Lingard, Paul (2009) Capacitance Based Virtual Instrument Mass Flow Measuring System. Masters by Research thesis (MSc), Manchester Metropolitan University.

CAPACITANCE BASED VIRTUAL INSTRUMENT MASS FLOW MEASURING SYSTEM

PAUL IAN LINGARD

MSc **2009**

CAPACITANCE BASED VIRTUAL INSTRUMENT MASS FLOW MEASURING SYSTEM

PAUL IAN LINGARD

A thesis submitted in fulfilment of the requirements of
The Manchester Metropolitan University for the degree of Master of Science

The Department of Engineering and Technology
The Manchester Metropolitan University

September 2009

Dedication

To the memory of my Father, Eric Lingard

Acknowledgments

I would like to thank first and foremost, Dr. Richard Deloughry for the opportunity, support and assistance in enabling me to undertake this MSc. I would like to also like to thank Dr. Idris Ibrahim for helping to make this whole experience more enjoyable, Dr. Prasad Ponnapalli for his helpful advice and Stephen Mason for his support.

Finally special thanks go to my long suffering wife Valerie for her understanding and patience during the long time I spent completing this project.

Declaration

No portion of the work referred to in this thesis has been submitted in support of an application for another degree or qualification of this, or any other institution of learning.

Signed…………………………………………….

Date……………………………………………….

Abstract

The research program conducted at the MMU into the design and development of a Virtual Instrument ECT Imaging System is a continuation from preceding investigations conducted by the MMU into tomographic imaging. The rationale behind the MMU tomographic imaging system is a response to the need for a robust and flexible proprietary tomographic imaging system appropriate for large industrial systems. The MMU Virtual Instrument ECT Imaging System consists of capacitance sensor(s), capacitance measuring hardware and the National Instruments (NI) PXI modular data acquisition system on which runs NI's LabVIEW graphical programming environment. The MMU tomographic imaging system is capable of high tomographic speed imaging from single and dual plane sensing arrays.

The purpose of this MSc project is, by utilising the MMU Virtual Instrument ECT Imaging System, to design and develop a virtual instrument measurement system for the purpose of measuring mass flow and flow velocity.

Evaluation of the virtual instrument measurement system is achieved by measuring the flow of polypropylene pellets through a vertical, hopper fed, gravity-conveyed flow system fitted with two axially spaced 8 electrode transducers. Pellet mass flow is determined from the averaged volumetric concentration of pellet materials present in the capacitance sensor placed in the upstream path of the pellet flow. Pellet velocity is determined by the cross correlation of the two random noise patterns generated by the pellets as it passes through the two capacitance sensors placed in the upstream and downstream path of the pellet flow.

Results are presented which show the relationship between the actual measured mass flow and the mean volumetric concentration taken from the upstream sensor compared to the number of independent normalised capacitance measurements taken from the upstream sensor. Also presented are results which relate the accuracy of the measured flow velocity to the number of independent normalised capacitance measurements taken from the upstream and downstream sensors.

The results presented show that as the number of independent normalised capacitance measurements taken from both the capacitance sensors are reduced, the electrostatic field distribution within the sensors becomes more inhomogeneous which has an adverse affect on the measurement accuracy of mass flow. Conversely, by increasing the number of independent normalised capacitance measurements taken from both the capacitance sensors has a detrimental affect on the accuracy of flow velocity measurement.

The results shown prove that the MMU Virtual Instrument ECT Imaging System is capable of individual accurate measurement of either mass flow or flow velocity. But, due to the limitations encountered with the current available hardware, simultaneous and accurate measurement of mass flow and flow velocity is impractical.

List of Tables

Chapter Two: Virtual Instrument Concepts

Table 2.1 Comparison between the PXI-6711, PXI-6733, and PXI-6143 20

Chapter Four: Electrical Capacitance Tomography (ECT)

Table 4.1 Normalised Voltage Correction Factors 44

Chapter Seven: Results

Table 7.1 The Total Number of Independent Averaged Normalised Capacitance Measurements (N_{CM}) Taken from the ECT Sensors and its Associated Sample Interval Time (δt) 109

Table 7.2 Comparison of Transit Time Measurements (τ_d), Pellet Velocity (v) and, Velocity Discrimination Factor (VDF) Obtained for Independent averaged normalised capacitance measurements (N_{CM}) of 7, 13, 18, 22 and, 28 122

List of Figures

Chapter One: Introduction

Figure 1.1 The MMU Flow Rig 3

Figure 1.2 Vertical Gravity-Conveyed Flow Measurement Section of the MMU Flow Rig 4

Figure 1.3 Schematic Overview of the System 5

Figure 1.4 The MMU VI ECT System Block Diagram 6

Figure 1.5 Determining Flow Rate from the Average Normalised Capacitance 7

Chapter Two: Virtual Instrument Concepts

Figure 2.1 Generic Block Diagram of a Traditional Instrument System 10

Figure 2.2 Instrument to Computer Interface 10

Figure 2.3 Generic Block Diagram of a Virtual Instrument System 11

Figure 2.4 PC Based Virtual Instrument System 12

Figure 2.5 PXI System Bus Architecture 14

Figure 2.6 A Typical Stand Alone PXI System 14

Figure 2.7 Component Parts of a LabVIEW Program 16

Figure 2.8 The Hierarchal Structure of a Virtual Instrument 17

Figure 2.9 VI Icon and Connector 18

Figure 2.10 The MMU Stand Alone PXI System 19

Figure 2.11 Tomographic Imaging System Overview 21

Chapter Three: Mass Flow Measurement Techniques

Figure 3.1 Steady State Capacitive Sensor 23

Figure 3.2 Sensitivity Distribution of a Capacitance Sensor with One Pair of Electrodes 23

Figure 3.3 Examples of Typical Solids Flow Patterns 24

Figure 3.4 Capacitance Sensor with a Rotating Field 24

Figure 3.5 The Capacitance Sensor with Compound Offset Electrodes 25

Figure 3.6 Non-intrusive Capacitive Flow Velocity Sensor 26

Figure 3.7 Transit Time between Upstream and Downstream Signals 26

Figure 3.8 The Cross Correlation Function 27

Figure 3.9 Theoretical Transfer Function of Sensor 28

Figure 3.10 Comparison between the Affect of Sensor Bandwidths on the Cross Correlation Function 29
Figure 3.11 Block Diagram of the Solids Mass Flowmeter Transducer 30
Figure 3.12 The Granucor Capacitance Flow Measurement System. Comprising of the DK 13 Velocity Sensor, DC 13 Concentration Sensor and MicroTech Correlator/Integrator 32
Figure 3.13 Typical Flow Measurement Setup 33
Figure 3.14 The Internal Structure of the DK 13 and DC 13 Sensors 34
Figure 3.15 DK 13 Internal Electrode Array 34
Figure 3.16 DK 13 Flow Velocity Sensor Signal Conditioning Electronics Block Diagram 35
Figure 3.17 DC 13 Concentration Sensor Signal Conditioning Electronics Block Diagram 36

Chapter Four: Electrical Capacitance Tomography (ECT)

Figure 4.1 The Core Components of an ECT Imaging System 38
Figure 4.2 Cross-sectional View of an ECT Sensor with External and Internal Electrode Configurations 38
Figure 4.3 Electrode-Pair Combinations for an 8 Electrode Sensor 39
Figure 4.4 A Typical ECT Sensor 40
Figure 4.5 Representations of the Electrical Field for Grounded and Driven Axial Guard Electrodes 41
Figure 4.6 Capacitance Cell Containing Vertically Stratified Material and Horizontally Stratified Material 43
Figure 4.7 A 1024 Pixel Grid (32 x 32 Pixels) Used to Image the Contents of a Circular Vessel Fitted with 8 Electrodes and an ECT Image of a Perspex Rod Placed Inside an Air Filled Sensor 45
Figure 4.8 The Four Primary Sensitivity Maps for an 8 Electrode Sensor 46
Figure 4.9 Intrinsically Stray-Immune Circuit Configuration 48
Figure 4.10 Differential Charge/Discharge Measurement Circuit 49
Figure 4.11 CMOS Switch Control Signals 50
Figure 4.12 AC Based Measuring Circuit 52
Figure 4.13 Equivalent Circuit of the Capacitive Sensor 53
Figure 4.14 The Phase Sensitive Detector (PSD) 54
Figure 4.15 Frequency Response of the Phase Sensitive Detector 55

Chapter Five: MMU Virtual Instrument ECT Imaging System

Figure 5.1 VI ECT System Hardware/Software Structure Overview 58

Figure 5.2 Diagram of the 8 Electrode Sensor Array 59

Figure 5.3 The 8 Electrode Sensor Array with Fitted Outer Shield 60

Figure 5.4 Measured Capacitance for an 8-Electrode ECT Sensor 61

Figure 5.5 Parallel Measurement Strategy Electrode Switching Sequence for an 8 Electrode ECT Sensor 62

Figure 5.6 Parallel Switching Electronics Functional Diagram 63

Figure 5.7 Circuit Configuration of DG419 CMOS SPDT Switches 63

Figure 5.8 Electrode Switch Arrangement 64

Figure 5.9 Block Diagram of the Capacitance Measurement Circuit 65

Figure 5.10 AC Bridge Circuit 66

Figure 5.11 The Burr Brown MPY634 Precision Wide-Bandwidth Multiplier as used in the Parallel System Standing Capacitance Compensation Circuit 67

Figure 5.12 Schematic Diagram of the Capacitance Measurement Stage 68

Figure 5.13 The Burr Brown MPY634 Precision Wide-Bandwidth Multiplier as used in the Signal Multiplier Stage of the Phase Sensitive Detector 70

Figure 5.14 PSD Low-Pass Filter Stage 71

Figure 5.15 The Final Version of the MMU ECT Capacitance Detection Hardware 73

Figure 5.16 The System Calibration VI's Front Panel and, the SubVIs called by the System Calibration VI 74

Figure 5.17 Typical DC Back-off Voltage Values for an 8 Electrode Sensor 75

Figure 5.18 Parallel Imaging System Front Panel 77

Figure 5.19 The Sequence of SubVI's Involved in the Generation of Permittivity Images 77

Figure 5.20 Collect Capacitance Data SubVI Flow Diagram 78

Figure 5.21 Simplified Version of the Image Reconstruction SubVI 79

Figure 5.22 Hierarchal Diagram of the ECT Method SubVI 79

Figure 5.23 The Dual-Plane 8-Electrode Imaging System Front Panel and, the Dual-Plane 8-Electrode Imaging VI Parallel Sequence Structure 80

Chapter Six: Development of a LabVIEW Virtual Instrument Cross Correlation Flowmeter

Figure 6.1 Cross Correlation of the Upstream and Downstream Sensor Signals 83

Figure 6.2 A Pictorial Representation of the Cross Correlation Process 84

Figure 6.3 The Discrete Cross Correlation Function 84

Figure 6.4 Comparison between the biased and unbiased values of $\hat{R}_{xy}(m)$ 85

Figure 6.5 Determination of System Bandwidth from $\rho_{xy}(\tau)$ 87

Figure 6.6 Point-by-Point Cross Correlation 89

Figure 6.7 Conceptual LabVIEW Diagram of Point-by-Point Cross Correlation 90

Figure 6.8 Evolutionary Cross Correlation Curves 91

Figure 6.9 The FFT Method for Calculating the CCF 91

Figure 6.10 The Dual-Plane 8-Electrode Imaging VI Parallel Sequence Structure with Modifications for Collecting Cross Correlation Data 93

Figure 6.11 Measurement Number Options Available in Cross Correlation Data Capture Mode 94

Figure 6.12 Typical Flow Profile of $\overline{V_{NC}}$ Values Taken from One of the ECT Sensors 95

Figure 6.13 Typical Averaged Normalised Capacitance Measurements ($\overline{V_{NC}}$) Taken from the Upstream and Downstream ECT Sensors 96

Figure 6.14 The Domination of CCF_β Obscures the Actual Required Peak Value 99

Figure 6.15 LabVIEW's Cross Correlation VI 99

Figure 6.16 Discrete Double Sided Cross Correlation 100

Figure 6.17 The MMU Virtual Instrument Measuring System CCF.VI and, the Hierarchal Diagram of the CCF.VI 101

Figure 6.18 An Example of the X and Y Signal Input Sequences and the Resulting Rxy Output Sequence as Applied to and Taken from, LabVIEW's CrossCorrelation VI 102

Figure 6.19 Obtaining the Delay Time from Rxy 103

Figure 6.20 Separation of the $x(n)$, $y(m)$, β_x and, β_y Information from the X and Y Signal Input Sequences by the Use of LabVIEW's "Mean.vi" 104

Chapter Seven: Results

Figure 7.1 Vertical Gravity-Conveyed Flow Section of the MMU Flow Rig 107

Figure 7.2 Mass Flow vs. Volumetric Concentration for Trial 1 110

Figure 7.3 Mass Flow vs. Volumetric Concentration for Trial 2 111

Figure 7.4 Mass Flow vs. Volumetric Concentration for Trial 3 111

Figure 7.5 The ECT Sensor Divided Into Quadrants 112

Figure 7.6 Measured Volumetric Concentration for all Four Quadrants 113

Figure 7.7 The Predefined Permittivity Images Corresponding to the Four Quadrant Positions within the ECT Sensor 114

Figure 7.8 The Second Set of Predefined Permittivity Images Used for the Simulation 115

Figure 7.9 Simulated Volumetric Concentration for all Four Quadrants 116

Figure 7.10 The Relative Contributions of Cross-Sectional Mean Volumetric Concentration Values of Each Quadrant as a Percentage of the Sum Total 116

Figure 7.11 Simulation Result of Voidage vs. Volumetric Concentration for the Centre Position 118

Figure 7.12 Simulation Result of Voidage vs. Volumetric Concentration for Quadrant 1 118

Figure 7.13 Simulation Result of Voidage vs. Volumetric Concentration for Quadrant 2 119

Figure 7.14 Simulation Result of Voidage vs. Volumetric Concentration for Quadrant 3 119

Figure 7.15 Simulation Result of Voidage vs. Volumetric Concentration for Quadrant 4 120

Figure 7.16 Comparison of Typical Correlograms Obtained for Independent Averaged Normalised Capacitance Measurements (N_{CM}) of 7, 13, 18, 22 and, 28 121

Figure 7.17 Mass Flow vs. Volumetric Concentration for $N_{CM} = 28$ Measurements (Averaged Over the Three Trials) 123

Figure 7.18 Qualitative Depiction of the Changes in the Electrostatic Field Generated Inside the ECT Sensor as the Number of Average Normalised Capacitance Measurements Taken Increases 125

Figure 7.19 Tomographic Images Taken from the Upstream and Downstream ECT Sensors 126

Chapter Eight: Conclusions and Future Work

Figure 8.1 Examples of Possible Alternative Field Rotation Measurement Configurations 129

Figure 8.2 Proposed LabVIEW Flowmeter Virtual Instrument 130

Appendix A: PSPICE Simulation Results for the MMU ECT System's Low Pass Filter

Figure A.1 PSPICE Simulated AC Magnitude Response of the 4th Order LPF 134

Figure A.2 PSPICE Simulated Transient Response of the 4th Order LPF 134

Appendix B: Derivation of Equation 6.17 in Chapter 6, Section 6.5.2.2

Figure B.1 Typical Averaged Normalised Capacitance Measurements ($\overline{V_N}$) Taken from the Upstream and Downstream ECT Sensors 136

Nomenclature

$[C]$	Matrix comprising of the normalised electrode pair, capacitance measurement combinations.
$[G]$	Vector comprising of the normalised grey level image.
$[K]$	Matrix comprising of the normalised pixel permittivity distribution.
$[S]$	Matrix comprising of the tomographic sensor's sensitivity map.
$[V_{NC}]$	Vector comprising of the normalised and corrected voltages, which are proportional to the change in capacitance between electrodes inside the tomographic sensor.
a	Capacitance sensor electrode axial length.
A	Flow cross sectional area.
A_s	Cross sectional area occupied by moving solid materials.
B	Correlation bandwidth.
C_x	Unknown capacitance.
ΔC_x	Change in unknown capacitance.
CF	Permittivity distribution correction factor.
d	Pipe diameter.
dB	Gain in decibels.
f_c	Bandwidth cut-off frequency of a capacitance sensor.
fF	Femtofarad (10^{-15} farads)

G_x	Loss conductance.
l	Axial distance between the upstream and downstream tomographic sensors.
M	Total number of possible independent electrode pair measurement combinations that can be taken from a tomographic sensor.
m	Discrete sample delay.
m_d	m^{th} sample corresponding to peak value of the discrete cross correlation function.
$\dot{m}$	Solids mean mass flow rate.
N	Total number of independent electrodes in a tomographic sensor.
N_{CM}	Total number of independent averaged normalised capacitance measurements taken from a tomographic sensor.
P	Maximum number of pixels in a tomographic image display grid.
Q_p	Transimpedance amplifier quality factor.
$R_{xy}(m)$	Discrete cross correlation function.
$\hat{R}_{xy}(m)$	Peak value of the discrete cross correlation function.
$R_{xy}(\tau)$	Cross correlation function.
$\hat{R}_{xy}(\tau)$	Peak value of the cross correlation function.
SF	Scaling Factor.
T	Overall observation time.
v	Solids mean flow velocity.
Δv	Change in measured solids mean flow velocity.

$v_{\max}$	Maximum measured solids mean flow velocity.
$v_{\min}$	Minimum measured solids mean flow velocity.
VDF	Velocity Discrimination Factor.
V_H	High permittivity measured reference voltage value, proportional to inter-electrode capacitance between tomographic sensor plate pairings
V_L	Low permittivity measured reference voltage value, proportional to inter-electrode capacitance between tomographic sensor plate pairings
V_N	Normalised measured voltage value, proportional to the change in capacitance between tomographic sensor plate pairings.
V_{NC}	Normalised and corrected measured value, proportional to the change in capacitance between tomographic sensor plate pairings.
$\overline{V_{NC}}$	Total Normalised and corrected, measured value, proportional to the overall change in capacitance between tomographic image frames.
V_M	Measured voltage value, proportional to inter-electrode capacitance between tomographic sensor plate pairings.
V_o	DC voltage output from the capacitance detector, proportional to the measured capacitance.
$x(n)$	Sampled ergodic signal taken from the upstream tomographic sensor
$x(t)$	Ergodic signal taken from the upstream tomographic sensor.
$y(n)$	Sampled ergodic signal taken from the downstream tomographic sensor.
$y(t)$	Ergodic signal taken from the downstream tomographic sensor.
β	Cross-sectional mean volumetric concentration of solids material within the tomographic sensor.

β_x	Cross-sectional mean volumetric concentration of solids material within the upstream tomographic sensor.
β_y	Cross-sectional mean volumetric concentration of solids material within the downstream tomographic sensor.
δt	Sample interval.
$\varepsilon(X,Y)$	Permittivity distribution of dielectric materials inside a tomographic sensor.
ε_H	Higher permittivity material.
ε_L	Lower permittivity material.
γ	Region of higher permittivity.
ρ	True density of the solids material.
$\rho_{xy}(m)$	Discrete normalised cross correlation function.
$\rho_{xy}(\tau)$	Normalised cross correlation function.
τ	Time delay.
τ_d	Transit time of the solids material as it passes between the upstream and downstream tomographic sensors.

Contents

Chapter One: Introduction 1

1.1 Objectives 1

1.2 Background 2

1.2.1 The Manchester Metropolitan University (MMU) Flow Rig 2

1.2.2 Measurement System 5

Chapter Two: Virtual Instrument Concepts 9

2.1 Introduction 9

2.2 Definition of a Virtual Instrument 9

2.3 National Instruments Virtual Instrumentation System 13

2.3.1 Hardware: The PXI System 13

2.3.2 Software: LabVIEW Graphical Programming Environment 15

2.3.3 The MMU Stand Alone PXI System 19

Chapter Three: Mass Flow Measurement Techniques 22

3.1 Introduction 22

3.2 The Steady State Capacitive Flow Sensor 22

3.3 Flow Velocity Measurement 25

3.4 Mass Flow Measurement 29

3.4.1 Direct Mass Flow Measurement 30

3.4.2 Inferential Mass Flow Measurement 31

3.5 A Practical Capacitance Based Mass Flow Measurement System 32

3.5.1 The DK 13 Velocity Sensor 34

3.5.2 The DC 13 Concentration Sensor 35

Chapter Four: Electrical Capacitance Tomography (ECT) 37

4.1 Introduction 37

4.2 Electrical Capacitance Tomography Overview 38

4.2.1 The ECT Sensor 40

4.2.2 Image Reconstruction 42

4.2.2.1 Normalisation 42

4.2.2.2 Linear Back Projection (LPB) 44

4.2.3 Capacitance Measuring Circuits 48

4.2.3.1 Stray Immunity 48

4.2.3.2 Differential Charge/Discharge Measuring Circuit 49

4.2.3.3 AC Based Measuring Circuit 52

Chapter Five: MMU Virtual Instrument ECT Imaging System 57

5.1 Introduction 57

5.2 MMU Virtual Instrument Measuring System (VIMS) 58

5.2.1 Imaging Hardware 59

5.2.1.1 The 8 Electrode Sensor Array 59

5.2.1.2 Parallel System Signal Routing 62

5.2.1.3 Capacitance Measurement 64

5.2.1.3.1 Standing Capacitance Compensation 65

5.2.1.3.2 Capacitance Measurement Circuit 67

5.2.2 Imaging Software 74

5.2.2.1 The System Calibration Application 74

5.2.2.1.1 Back-off Voltage Finder 75

5.2.2.1.2 Normalisation Voltage Finder 76

5.2.2.2 Real Time Data Capture and Image Reconstruction 76

5.2.2.2.1 Collect Capacitance Data from the ECT Hardware 78

5.2.2.2.2 Image Reconstruction 78

5.2.2.3 Dual-Plane 8-Electrode Imaging 80

5.3 Conclusion 81

Chapter Six: Development of a LabVIEW Virtual Instrument Cross Correlation Flowmeter 82

6.1 Introduction 82

6.2 Cross Correlation of Sampled Signals 82

6.2.1 The Discrete Cross Correlation Function 82

6.2.2 Edge effect 84

6.2.3 Pearson's ρ Coefficient 86

6.3 Measurement Accuracy 86

6.3.1 Statistical Errors in Time Delay Measurement 86

6.3.2 Velocity Discrimination Factor 88

6.4 Computational Methods of Calculating the Cross Correlation Function 89

6.4.1 Direct Methods 89

6.4.1.1 Point-by-Point Method 89

6.4.1.2 Evolutionary Method 90

6.4.2 Frequency Domain Method 91

6.4.2.1 Fast Fourier Transform (FFT) 91

6.5 The Measurement of Solids Mass Flow using LabVIEW 92
  6.5.1 VI Overview 92
  6.5.2 The Virtual Instrument Measuring System's Cross Correlation Function Virtual Instrument (CCF.VI) 99
    6.5.2.1 LabVIEW's Cross Correlation VI 99
    6.5.2.2 The CCF.VI 101
6.6 Conclusion 104

Chapter Seven: Results 106
7.1 Introduction 106
7.2 Results 106
  7.2.1 Vertical Mass Flow Measurement 106
  7.2.2 Pellet Velocity Measurement 121
  7.2.3 True Density of the Solids Material 122
7.3 Conclusions 125

Chapter Eight: Conclusions and Future Work 127
8.1 Conclusions 127
8.2 Future Work and Recommendations 128
  8.2.1 Mass Flow Measurement 128
    8.2.1.1 Modification to the MMU Flow Rig 128
    8.2.1.2 Modifications to the Imaging Hardware and LabVIEW Software 128
  8.2.2 Flow Velocity Measurement 130
    8.2.2.1 Development of an Improved Flowmeter Virtual Instrument 130
    8.2.2.2 Single Plane Velocity Measurement 131
8.3 Contributions to Knowledge and Learning 131
8.4 Fulfilment of Objectives 132

Appendix A: PSPICE Simulation Results for the MMU ECT System's Low Pass Filter 133

Appendix B: Derivation of Equation 6.17 in Chapter 6, Section 6.5.2.2 135

Appendix C: Related Published Papers 138
Application of an Industrial Embedded Virtual Instrument System to Electrical Capacitance Tomographic Imaging 139
PXI-Based Electrical Capacitance Tomographic Imaging System Applied to Flow Control and Mass Flow Measurement 146

References 156

Chapter One

1 Introduction

The pneumatic conveying of bulk solids has played an important role in industry for decades. The advantages of pneumatic conveying systems have long been known. The fact that pneumatic conveying systems have few moving parts, make it more reliable and relatively efficient when compared with mechanical conveying systems. Additionally, the closed nature of the pneumatic conveying system prevents loss of material and contamination during transport.

The measurement of mass flow in pneumatic conveying systems is particularly important, in the process industry [1, 2]. A number of materials e.g. plastic, corn, coal, powders have dielectric properties which enable the use of capacitance measurement to be employed to extrapolate the mass flow of the material. Established capacitance measuring techniques such as the AC bridge [3, 4] and the charge discharge circuit [5, 6] can be adapted for measuring mass flow. The virtual instrument concept [7, 8], which is a PC based system, has been developed commercially to facilitate the rapid development of instrument systems. The virtual instrument software has a number of processing functions that will enable the velocity of the material to be determined. Combining the capacitance measurement techniques with a virtual instrument system platform will enable a mass flow instrument to be developed.

1.1 Objectives

The exploratory research was guided by four main objectives:

1. To design and develop a flow rig to enable different materials mass flow regimes to be assessed and determined.
2. To analyse the use of capacitance measurement techniques to mass flow measurement.
3. To investigate the use of signal processing techniques that will allow the velocity of material passing through a pipe to be determined.

4. To develop Virtual Instrument based on National Instrument LabVIEW Graphical programming system.

By using outcomes of these initial investigations, the benefits of a Virtual Instrumentation System (VIS) applied to a mass flow measuring system could be evaluated.

1.2 Background

The initial work on the measurement of flow using capacitance sensing was undertaken by Pickup [3] and involved the development of an AC bridge detection circuit allied to a PC based Texas C40 parallel tomographic imaging system to measure and control the flow of pneumatically conveyed particles. The work was extended further by Young [4] who undertook research into the application of the modified tomographic imaging and mass flow measuring system to improve the loading of road tankers. The research work was industrial based work for Montell (part of the Shell group of industries) and successful but indicated the need for a robust proprietary measuring system when applied to large industrial systems. The work by Davenport [8] showed how National Instruments LabVIEW graphical programming techniques could be configured to form a virtual instrument system which could be applied to Tomographic imaging and mass flow measurement. Ibrahim [9] extend this work further by producing a new National Instruments PXI based tomographic imaging capable of high speed imaging from single and dual plane sensing arrays. The imaging system was also used to control the flow of material using a Neural Network controller.

1.2.1 The Manchester Metropolitan University (MMU) Flow Rig

The MMU flow rig initially designed to replicate industrial pneumatic conveying systems was modified to simulate a vertical, hopper fed, gravity-conveyed flow system. A schematic of the flow rig and the dimensions are shown in Figure 1.1.

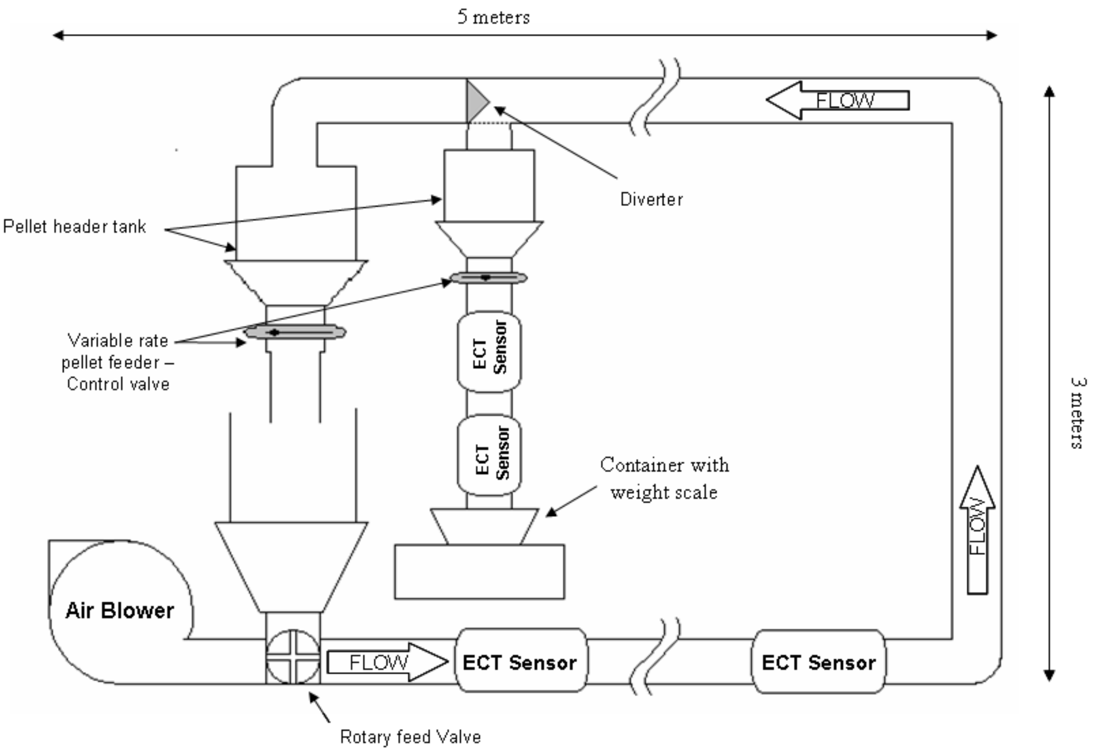

Figure 1.1 The MMU Flow Rig

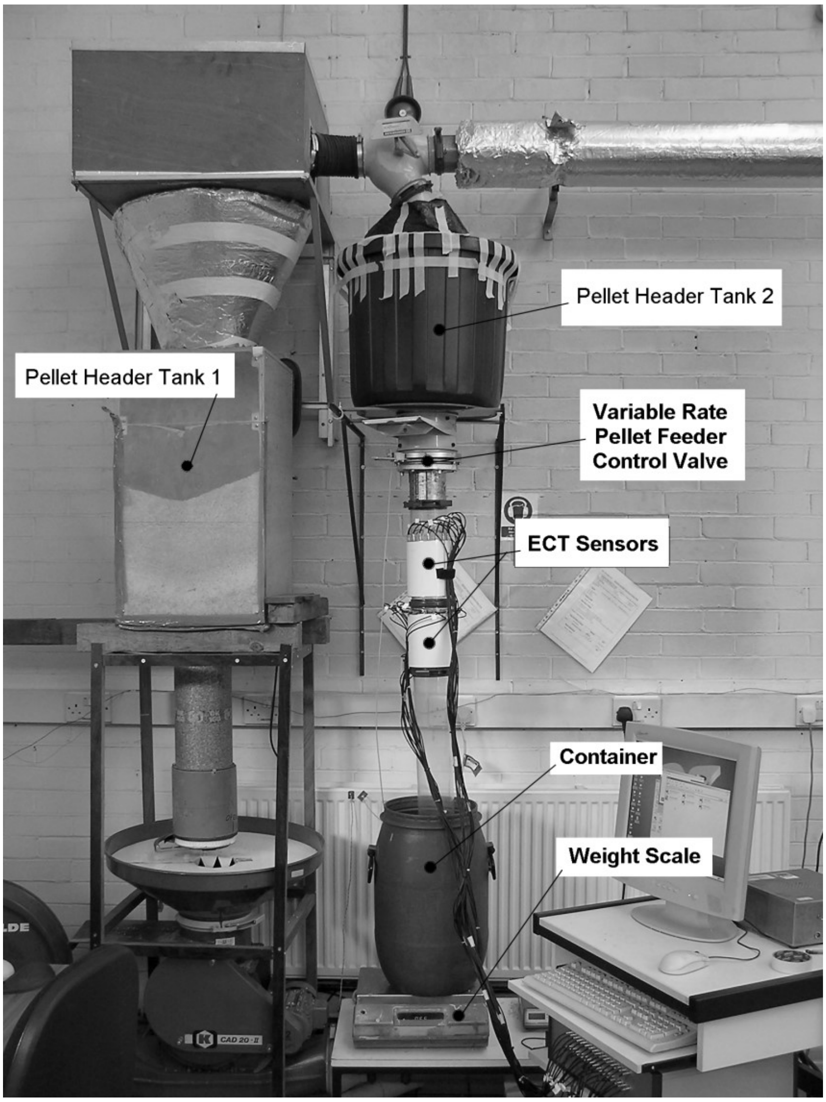

Figure 1.2 Vertical Gravity-Conveyed Flow Measurement Section of the MMU Flow Rig

Figure 1.2 shows the gravity-conveyed test section of the flow rig. Polypropylene pellets contained in header tank one, are pneumatically transferred through the system via the diverter into header tank two. Once this has been achieved, the gravitational flow rate of the pellets can be manually set by the variable rate pellet feeder valve located underneath the exit point of tank two. The output from pellet header tank 2 tank feeds directly through two axially spaced ECT sensing arrays into a container. The mass of the container is measured using a digital weigh scale, which has an auto zeroing function. The ECT sensing system is connected to the PXI Tomographic imaging and mass flow measuring system. A schematic overview of the system is shown in Figure 1.3.

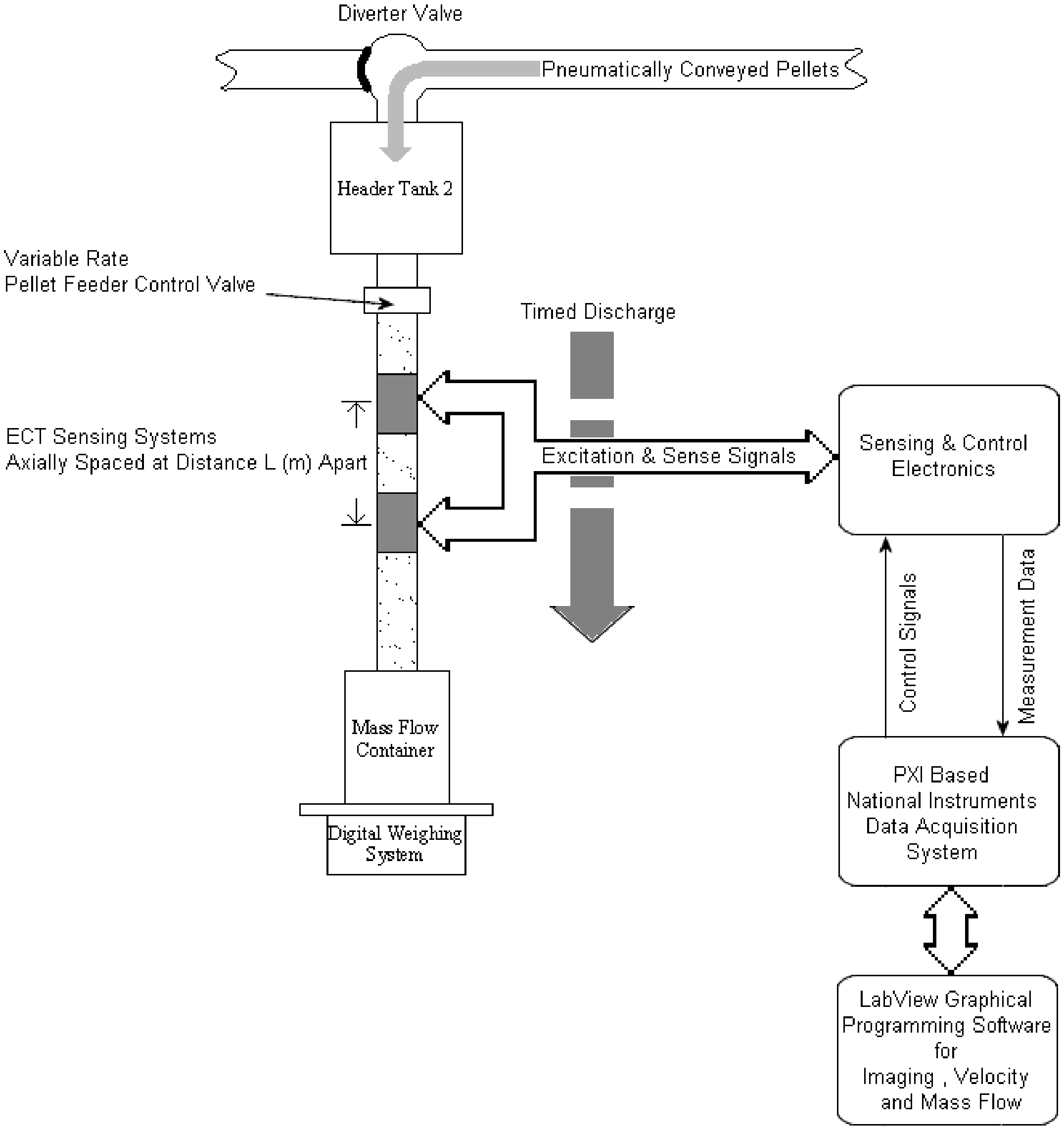

Figure 1.3 Schematic Overview of the System

1.2.2 Measurement System

The development of the mass flow rate measurement system will be an adaptation based on the dual-plane, Virtual Instrument (VI), Electrical Capacitance Tomography (ECT) system developed at the MMU [9].

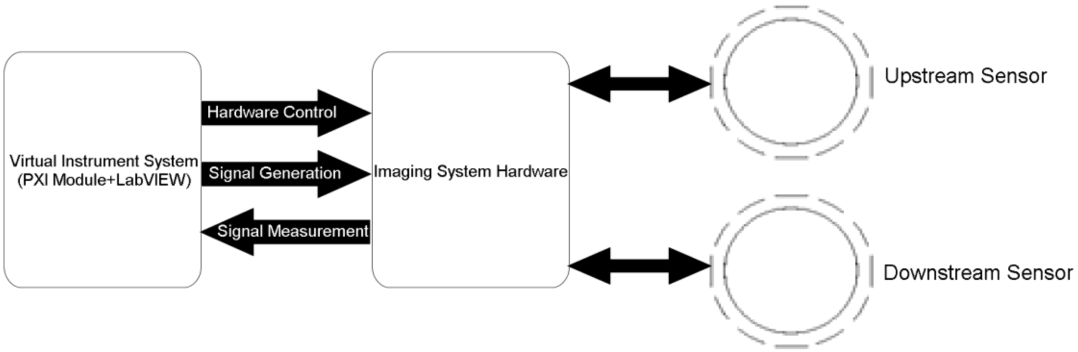

Figure 1.4 The MMU VI ECT System Block Diagram

A block diagram of the system is shown in Figure 1.4. Two separate ECT sensors are used to image upstream and downstream flows. The measurements acquired from the two sensors are controlled, as well as the stimulus and measurement signals being conditioned, by the imaging system hardware. The hardware selects the appropriate channel plate to be excited and then sequences the required remaining plates to acquire data both for the Tomographic image to be formed and for the velocity measurement to be determined. Overall control and data interpretation is executed by a stand alone virtual instrument system.

The signal information required for velocity and subsequently, mass flow measurement can be extracted as a subset of the tomographic imaging data gathered by the virtual instrument system. Where the overall averaged normalised[1] capacitance variations measured by the upstream and downstream Electrical Capacitance Tomography (ECT) sensors, as the flow of the material passes through them can be cross-correlated to determine the velocity (ms^{-1}) of the flow and the mass flow rate ($kg\ s^{-1}$) of the material is determined.

---

[1] Each sensor is calibrated to have a numerical value of zero when empty, and a value of one when full.

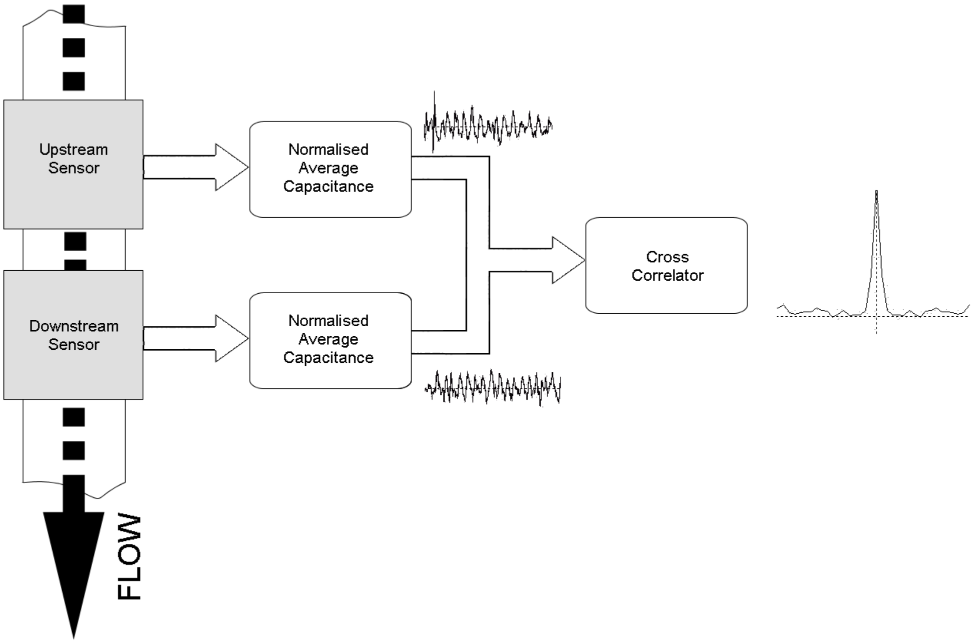

Figure 1.5 Determining Flow Rate from the Average Normalised Capacitance

From the flow rate the mass flow rate can be determined from Equation 1.1.

$$\dot{m} = \rho\, v\, A$$ **Equation 1.1**

Where:

$\dot{m}$ is the mass flow rate $\left(\frac{kg}{s}\right)$.

ρ is the true density of the material $\left(\frac{kg}{m^3}\right)$.

v is the velocity $\left(\frac{m}{s}\right)$.

A is the flow cross sectional area $\left(m^2\right)$.

The value for volumetric concentration can be determined from the averaged normalised capacitance given by the upstream ECT sensor. This is achieved by weighing the amount of solids conveyed in a suitable time interval, measured by a stop watch, over a range of different settings and establishing the relationship between volumetric concentration and average normalised capacitance. The results of these measurements will be presented in Chapter 7.

Chapter Two

2 Virtual Instrument Concepts

2.1 Introduction

This chapter introduces the concept of a virtual instrument and discusses how a virtual instrument differs from a more traditional instrument. The chapter then explains how software and hardware components are integrated together to build up a complete Virtual Instrument System (VIS). The chapter then expands on this theme by looking at an actual industrial virtual instrument system produced the National Instruments Corporation and its virtual instrument hardware (PXI system) and software (LabVIEW development system). The chapter finishes by detailing the configuration MMU PXI system and explaining how it is integrated into the MMU tomographic imaging system.

2.2 Definition of a Virtual Instrument

Modern traditional fixed-function digital test and measurement instruments such as oscilloscopes and signal generators are generally microprocessor based but are made up of predefined hardware, chiefly composed of analogue-to-digital (ADC), digital-to-analogue (DAC) converters and pre-programmed firmware components as shown in Figure 2.1. Although these test instruments are versatile and can perform many functions, the core functionality of the instrument is limited to their individual stimulus, measurement, or analysis functions.

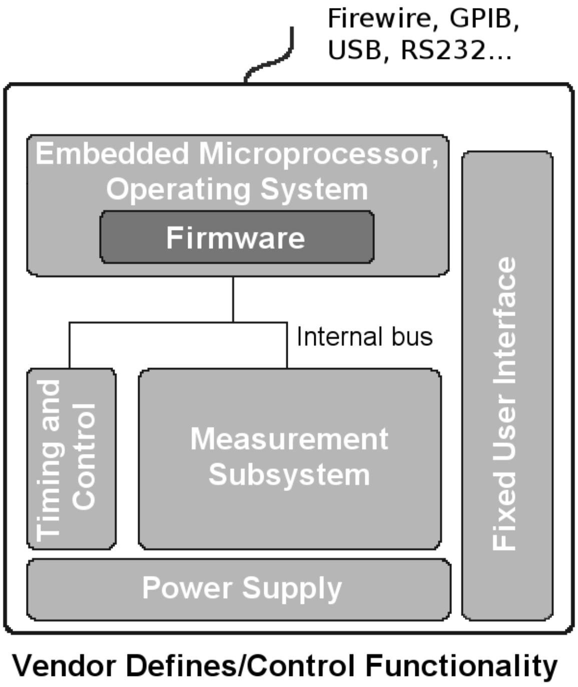

Figure 2.1 Generic Block Diagram of a Traditional Instrument System

Most modern instruments are equipped with some form of instrument to computer interface [10, 11] (Firewire, GPIB, USB, RS232 etc.) which provides remote communication from the host computer to the instrument (Figure 2.2) by the use of instrument control software, capable performing pre or post data analysis and, data storage. Data can be extracted from the acquired input signal, analysed, and then presented to the user by the use of a Graphical User Interface (GUI). This can essentially increase, to a limited degree, the instruments flexibility but can prove to be an expensive and bulky solution when multi-instrument systems are required.

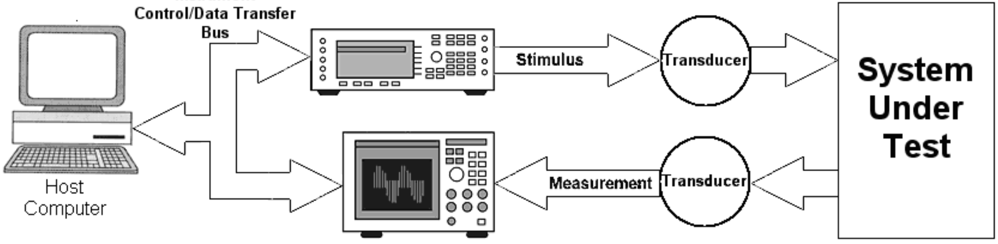

Figure 2.2 Instrument to Computer Interface

This methodology does however represent a shift from traditional totally hardware-centred measurement systems to flexible software controlled automated measurement systems.

The overall functionality of a measurement system can be vastly improved by combining the user defined software approach with user defined modular hardware systems. This approach is the core difference between a conventional instrument and a Virtual Instrument (VI). Even though traditional instruments largely share the same architectural components when compared to a virtual instrument, it is the modular approach to the hardware/software amalgamation used by the system which separates a virtual instrument from a traditional instrument (Figure 2.3) [12].

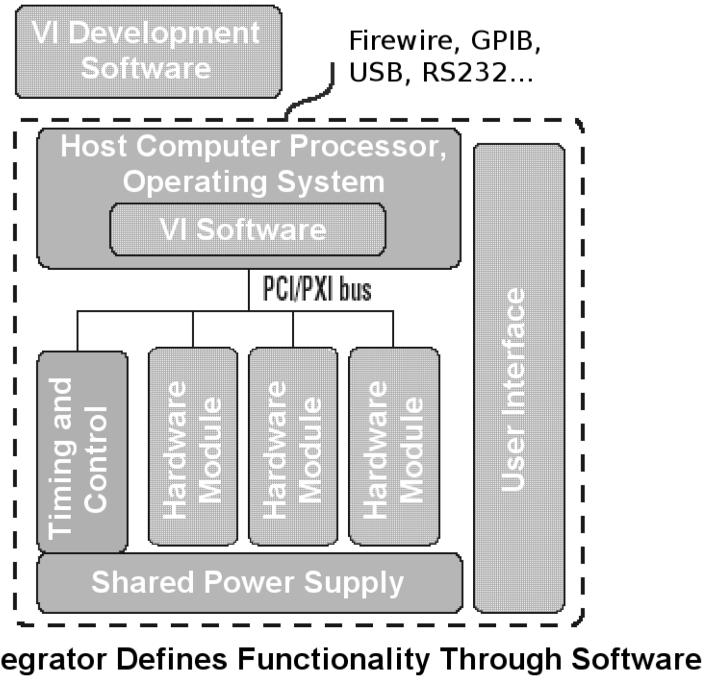

Figure 2.3 Generic Block Diagram of a Virtual Instrument System

Figure 2.4 shows the components of a rudimentary PC based virtual instrument system. The core of this system is usually a vendor proprietary internal, PCI form factor, plug in multifunction data acquisition board. Typical hardware subsystems contained on these boards are:

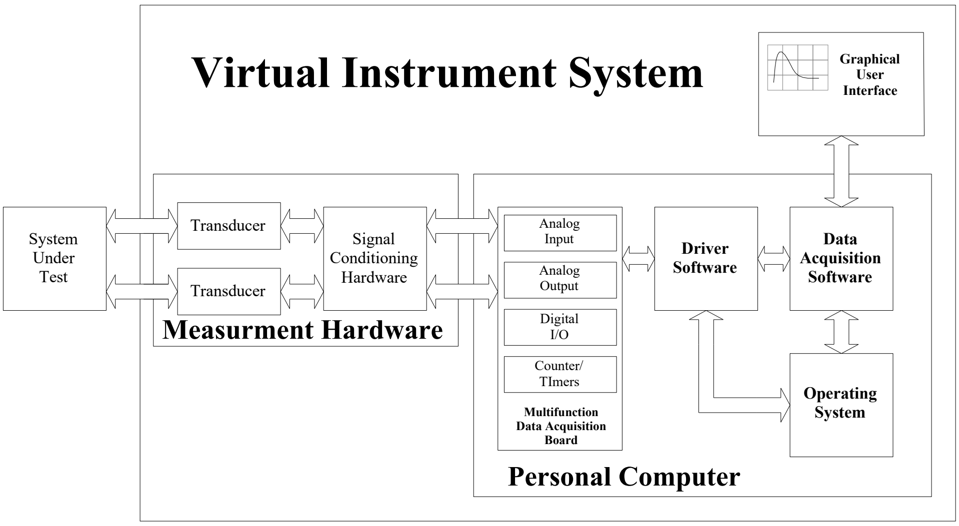

Figure 2.4 PC Based Virtual Instrument System

- **Analog Inputs:** By means of an analog-to-digital converter, analog input subsystems convert analog input voltage signals into its corresponding numerical representation. These subsystems can have up to 64 analog input channels at 12 or 16 bits resolution.
- **Analog Outputs:** Analog output subsystems convert numerical values generated by the data acquisition software into output voltages. Like analog input subsystems, they are typically multichannel devices offering 12 or 16 bits of resolution.
- **Digital I/O:** Digital input/output subsystems input and output digital values (typically 0 – 5 volts) either as single bits or as 8, 16, or 32 bit ports depending on the actual hardware configuration.
- **Counter/Timers:** Counter/timer subsystems are used for event counting, frequency and period measurement, and pulse train generation.

Multifunction data acquisition boards are usually provided with software drivers which act as in interface between the data acquisition board, the operating system (e.g. Windows or Linux), and the data acquisition software such as National Instrument's LabVIEW or MathWork’s MATLAB.

Software platform such as LabVIEW and MATLAB, are high-level technical computing languages and interactive environments which perform data analysis such as signal processing and acts as the user interface for inputting and displaying data.

The benefits of software-defined virtual instruments include:

- Increased system flexibility through reconfiguring software.
- Increased system longevity by adapting to future needs.
- Lower system size by creating multiple software personalities on shared measurement hardware.
- Lower system cost through hardware reuse.
- The ability to solve unique system requirements not addressed by existing traditional instruments.
- Reduce costs by reusing hardware for many applications.

2.3 National Instruments Virtual Instrumentation System

2.3.1 Hardware: The PXI System

Integrating several hardware modules into a single virtual instrumentation system requires sophisticated timing and synchronization between individual modules which cannot be easily implemented using standard ISA, PCI, or CompactPCI bus systems.

Originally introduced in 1997 by National Instruments, the PXI bus is an extended version of the standard PCI bus with added timing and synchronization capabilities hence its acronym, **P**CI e**X**tensions for **I**nstrumentation (PXI). This extra hardware functionality is achieved by the following additional buses (Figure 2.5);

- **System Reference Clock**
  A 10MHz built-in common reference clock provides synchronization between multiple modules.
- **Trigger Bus**
  Eight trigger bus lines provide shared trigger, clock and handshaking signals.
- **Star Trigger Bus**
  Provides an high speed trigger with low levels of delay and skew. To achieve this, an independent line is routed the star trigger controller to each of the other slots in a star configuration.
- **Local Bus**
  In addition to the standard PCI bus a third bus is known as the local bus allows both

digital and analogue signals to be passed over it. In this way signals that may be required to be transferred within the chassis can be accommodated.

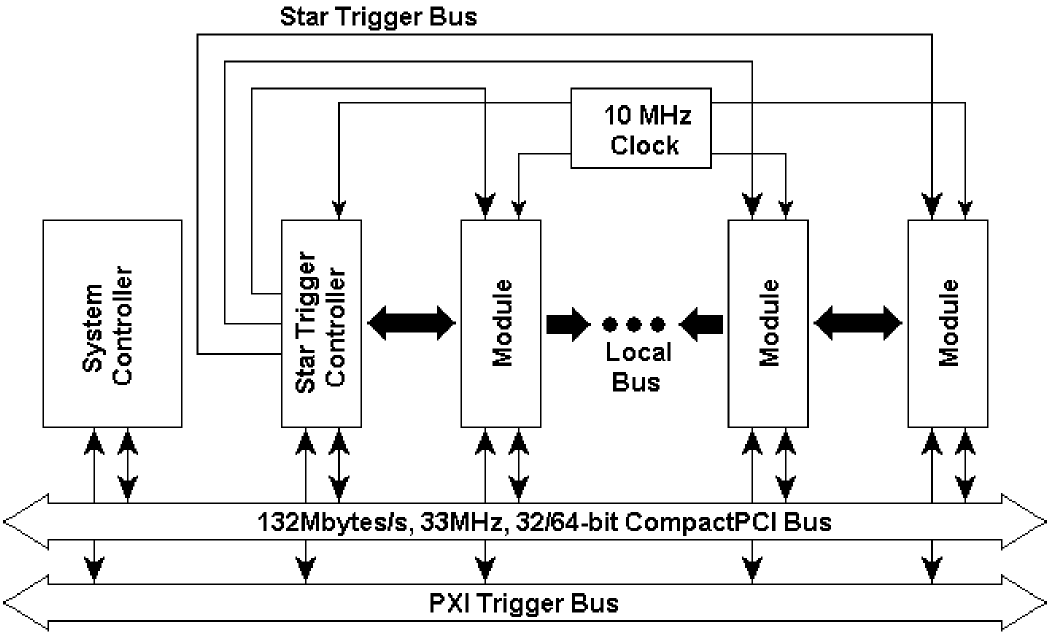

Figure 2.5 PXI System Bus Architecture

In addition, whereas most desktop PCI systems offer only three peripheral slots per bus segment, PXI systems can have up to seven peripheral slots per bus segment.

To ensure that PXI based systems operate reliably in harsh industrial environments. It is a requirement of the PXI specification that all PXI systems should use high-performance IEC connectors and rugged Eurocard enclosures with specific cooling and environmental requirements.

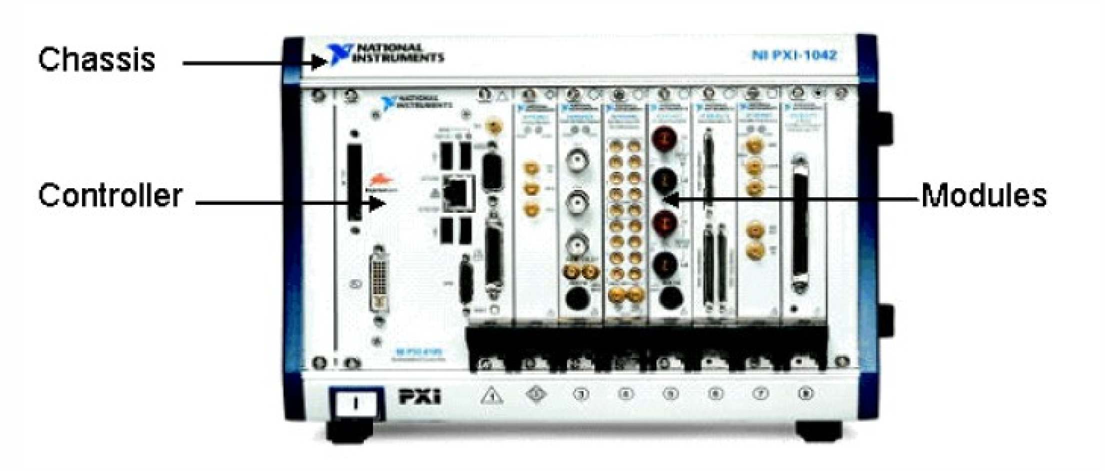

Figure 2.6 A Typical Stand Alone PXI System

Stand alone PXI systems comprises of three fundamental system components (Figure 2.6):

- **Chassis**
  As well as providing the PXI backplane for the instrumentation system. The chassis also provides DC power supplies and cooling for the system controller and modules.
- **Controller**
  In the case of stand alone systems, the PXI system will have an embedded controller which is a standard desktop PC produced as a small, PXI module.
- **Modules**
  Comprises of various user selectable peripheral data acquisition modules or instruments that slot into the chassis.

2.3.2 Software: LabVIEW Graphical Programming Environment

Developed by National Instruments, LabVIEW (**Lab**oratory **V**irtual **I**nstrumentation **E**ngineering **W**orkbench) is a graphical programming environment used primarily in data acquisition and instrumentation control.

In contrast to other high level programming languages in which lines of text based code define the sequential actions of the program, programs written using LabVIEW relies on interconnected graphical symbols which define and control dataflow, to characterise a programs behaviour [8, 13].

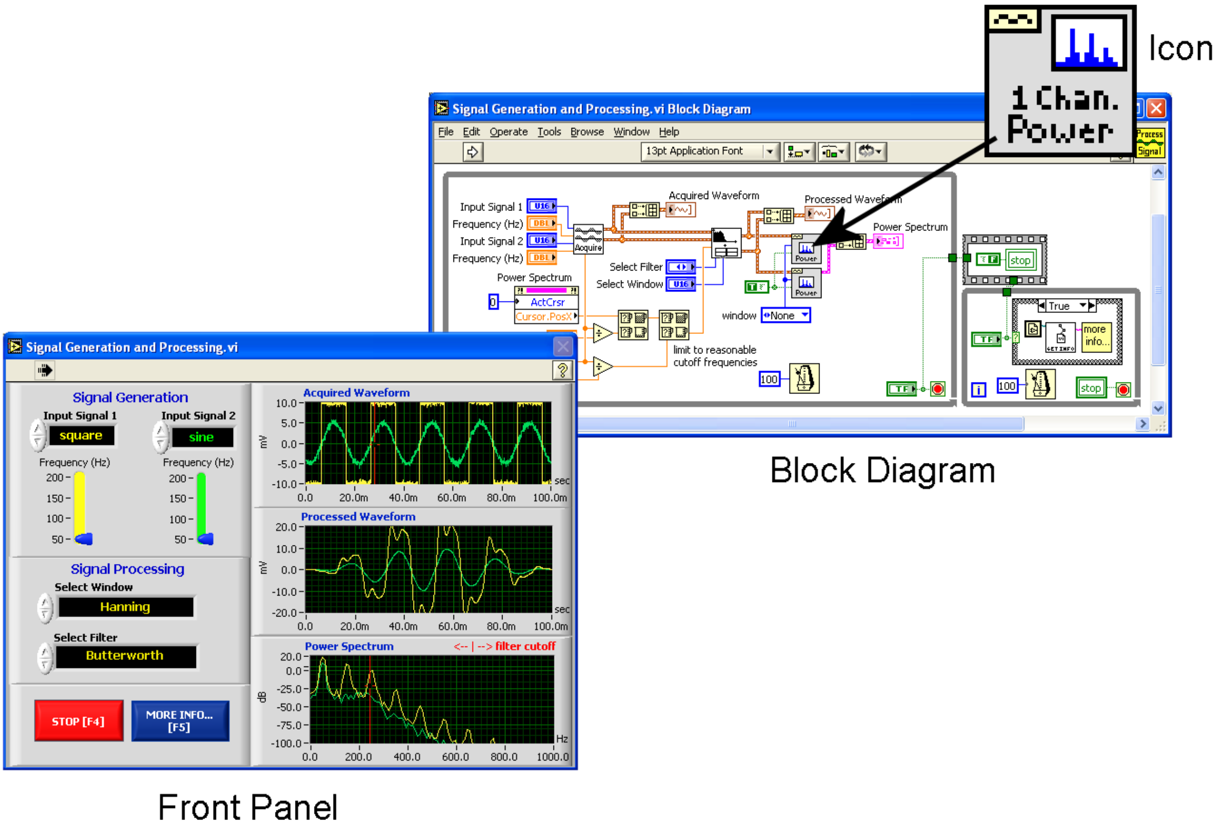

Figure 2.7 Component Parts of a LabVIEW Program

A LabVIEW program is built up of three main components (Figure 2.7):

- **Front Panel.**
  The front panel is the user interface of the program. It is made up of controls (inputs) and indicators (outputs) which simulate the front panel of an instrument. It is mainly for this reason that a LabVIEW program is usually referred to as a Virtual Instrument (VI) irrespective of whether or not its function and appearance resembles an actual physical instrument.
- **Block Diagram.**
  The block diagram is graphical representation of VI's source code which defines the operation of the VI. The block diagram consists of terminals (an interface to the front panel objects), subVIs, functions, constants and, structures, which are "wired together" to transfer data to other block diagram objects.

- **Icons.**

  Like other high level programming languages, LabVIEW is designed to be modular and hierarchal (Figure 2.8). In a similar way other languages use subprograms, VIs can contain within it, lower level VIs (subVI) represented as a pictorial icon in the block diagram. To be able to use a single VI as a subVI, the VI must have an icon and a connector (in order to pass data to and from the VI) defined for it during the programming phase (Figure 2.9). LabVIEW comes with an extensive library of prewritten subVI modules among which include functions for data acquisition, mathematics and signal processing.

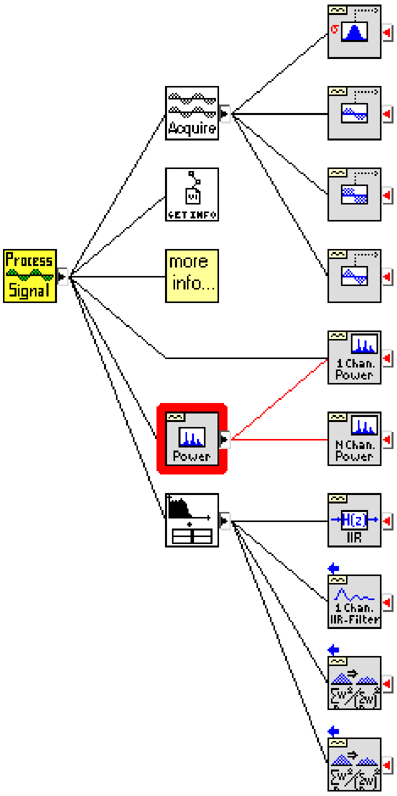

Figure 2.8 The Hierarchal Structure of a Virtual Instrument

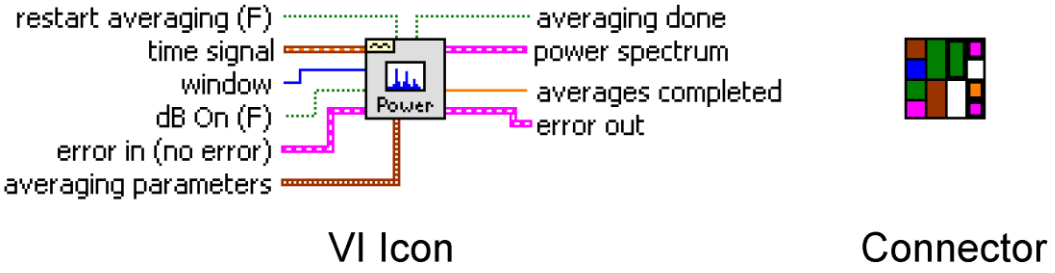

Figure 2.9 VI Icon and Connector

The main advantage LabVIEW has as a program development platform for the scientist and engineer over other high level text-based programming languages such as C++ or BASIC is the more intuitive graphical programming environment which makes LabVIEW relatively easy to learn and use effectively [14]. LabVIEW also has an extensive library of readily available plug-in program modules, built-in user interface controls and indicators, and integrated I/O capabilities, which decreases software development time and complexity.

The main criticism levelled at LabVIEW is in the fact that when compared to other development suites; LabVIEW is an expensive option (current price 2009 between £1049 for the base suite and £3599 for the full developer suite). Also, it is not particularly easy to integrate with the more conventional text based computer languages and its lack of object oriented features. This has since somewhat been resolved to some extent with the introduction of LabVIEW 2009. The portability and distribution of LabVIEW applications is hampered by the fact that LabVIEW requires a separately-installed run-time engine.

2.3.3 The MMU Stand Alone PXI System

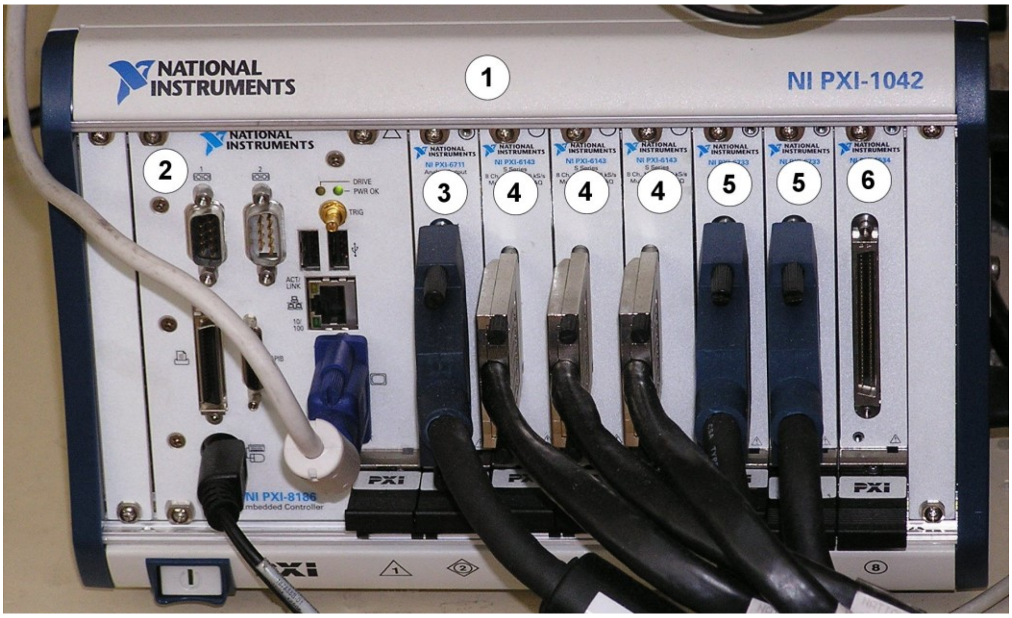

Figure 2.10 The MMU Stand Alone PXI System

Figure 2.10 shows the NI stand alone PXI system as used by the MMU. Based on the PXI-1042 [15] general purpose 3U backplane 8 slot chassis (Figure 2.10, Label 1), the PXI system uses the following modules:

- PXI-8186 (Figure 2.10, Label 2): 2.2GHz Pentium 4 based embedded computer/controller. Produced as a small and rugged, PXI module it has many similarities to a standard desktop PC, but has additional, on board PXI specific, triggering and timing hardware [16].
- PXI-6711 (Figure 2.10, Label 3): The PXI-6711 is a high speed, 12 bit, four channel, voltage output device incorporating an eight channel digital I/O (**I**nput/**O**utput) port [17]. This module is used to generate excitation and reference signals for the tomographic imaging hardware Figure 2.11.
- PXI-6143 (Figure 2.10, Label 4): The PXI-6143 is a multifunction eight channel analog data acquisition module [18] and similar to the PXI-6711 and PXI-6733 has digital I/O capabilities. Two of these modules are used to read capacitance data from the tomographic imaging hardware Figure 2.11.
- PXI-6733 (Figure 2.10, Label 5): The PXI-6733 has the same functional specification as the PXI-6711. Differing only in the number of output channels (eight) and resolution (16 bit) [17]. Two of these modules are used to generate the

D.C. back off values for capacitance measurement and to control signal routing within the tomographic imaging hardware Figure 2.11. The functionality and specifications of the PXI-6711, PXI-6143 and, PXI-6733 are summarized in (Table 2.1) below.

- PXI-6534 (Figure 2.10, Label 6): The PXI-6534 is a high-speed, 32-bit, parallel Digital Input/Output (DIO) interface. Which can either generate or read 5V TTL or CMOS digital patterns at a rate of up to 80 MB/s [19]. This module will not be used for this application.

	Module		
Specification	**PXI-6711**	**PXI-6733**	**PXI-6143**
Analog Inputs	N/A	N/A	8
Analog Outputs	4	8	N/A
Resolution	12 bits	16 bits	16 bits
Sampling rate	N/A	N/A	250 kS/s per channel
Maximum Update Rate	1 MS/s	1 MS/s	N/A
Output Range	±10 V	±10V	N/A
Input Range	N/A	N/A	±5V
Digital I/O	8	8	8
Counter/Timers	2,24-bit	2,24bit	2,24bit
Triggers	Digital	Digital	Digital

Table 2.1 Comparison between the PXI-6711, PXI-6733, and PXI-6143

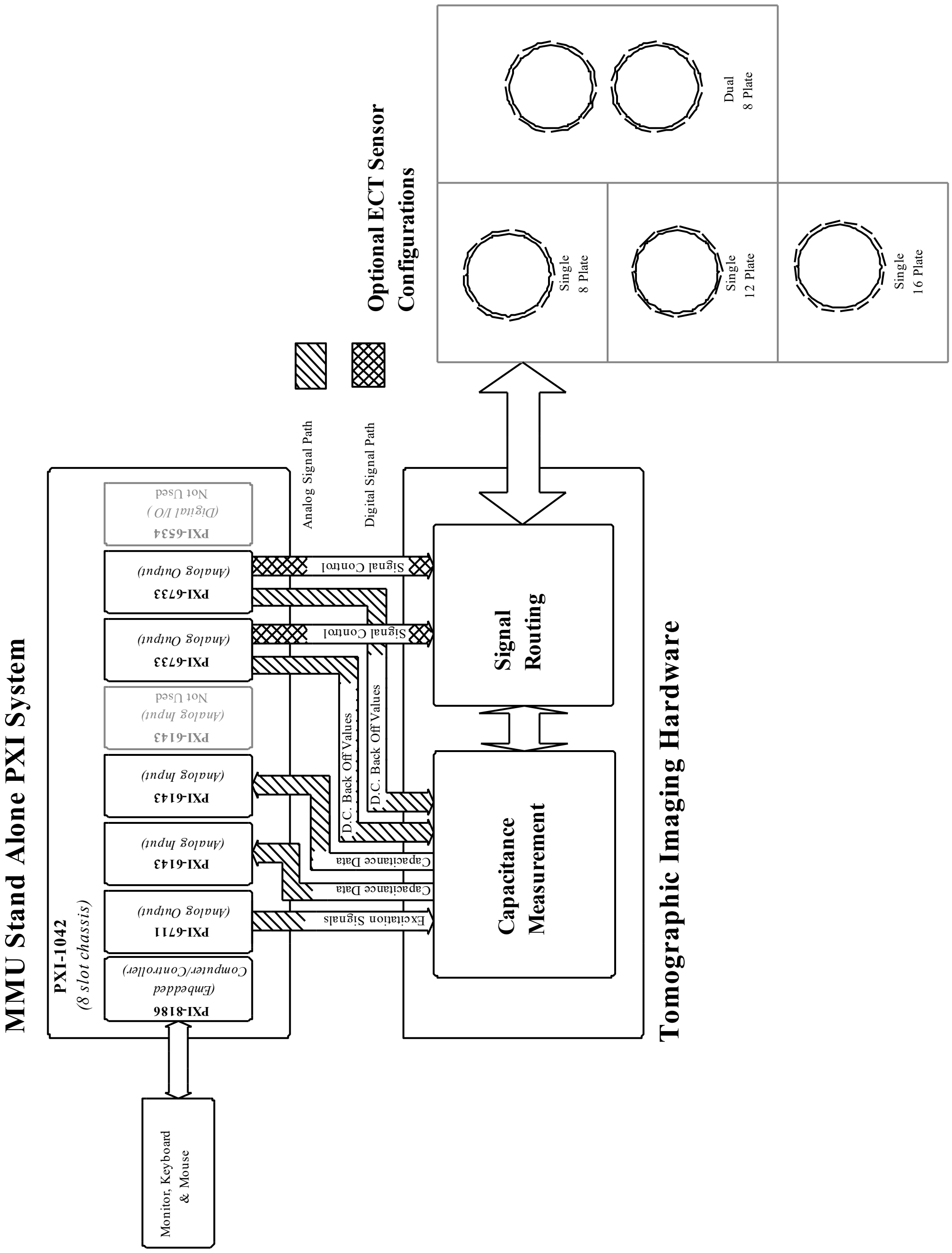

Figure 2.11 Tomographic Imaging System Overview

Chapter Three

3 Mass Flow Measurement Techniques

3.1 Introduction

Sensors used as a basis for measuring the mass flow of bulk conveyed particulate solids in closed pneumatic systems, fall into two major categories, intrusive or non-intrusive. Intrusive sensors inside the conveyer's pipeline have been successively used in solids flow measurement, but the main problem with intrusive sensors lies in the fact that the movement of high velocity abrasive particles causes wear and can quickly damage the sensor arrangement. It is primarily for this reason combined with its low cost to manufacture that the steady state capacitive sensor is the most commonly used method for the measurement non-conductive solids flow.

This chapter examines the structure of a steady state capacitive flow sensor and outlines some of the inherent underlying problems associated with this type of sensor and suggests some methods by which they can be alleviated. The chapter then goes on to introduce the method of cross correlation for measuring flow velocity and the concept of "spatial filtering" and its affect on sensor design. The chapter then examines the techniques used to measure mass flow and outlines the difference between "direct" and "inferential" mass flow measurement methods. The chapter then ends by briefly examining the Granucor flow measurement system produced by the Thermo Electron Corporation.

3.2 The Steady State Capacitive Flow Sensor

The steady state capacitive sensor for non-conductive solid flow measurement consists of two conducting electrodes placed either side of a non-conductive flow vessel which effectively form a capacitor (Figure 3.1). Non-conducting material flowing through the vessel creates a change in the relative permittivity of the dielectric which in turn creates a change in the capacitance of the sensor, which is then converted into an electronic signal by the capacitance measuring circuit.

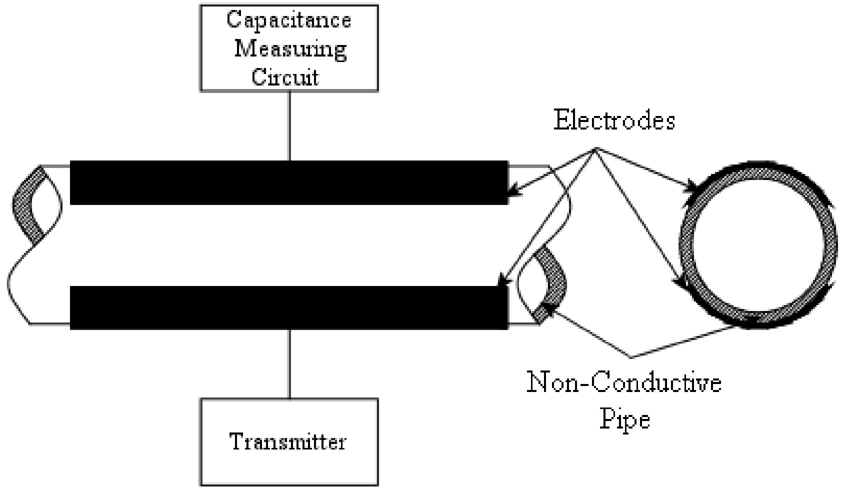

Figure 3.1 Steady State Capacitive Sensor

The electronic signal resulting from the change in capacitance can be related to flow rate by the cross correlation of two signals from upstream and downstream sensors, or to solids concentration (or mass flow) from the measurement of the magnitude of the signal.

Figure 3.2 shows the sensitivity distribution of a concave plate capacitance sensor. The inhomogeneous distribution of the field sensitivity within the sensor results in flow regime dependence (Figure 3.3) when attempting to measure volumetric concentration.

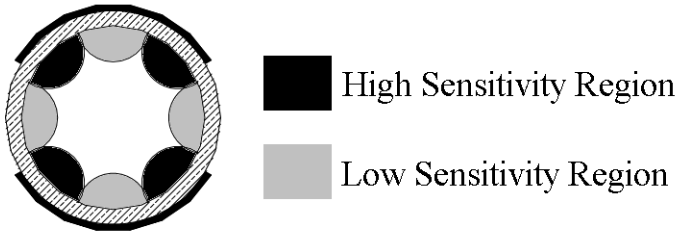

Figure 3.2 Sensitivity Distribution of a Capacitance Sensor with One Pair of Electrodes

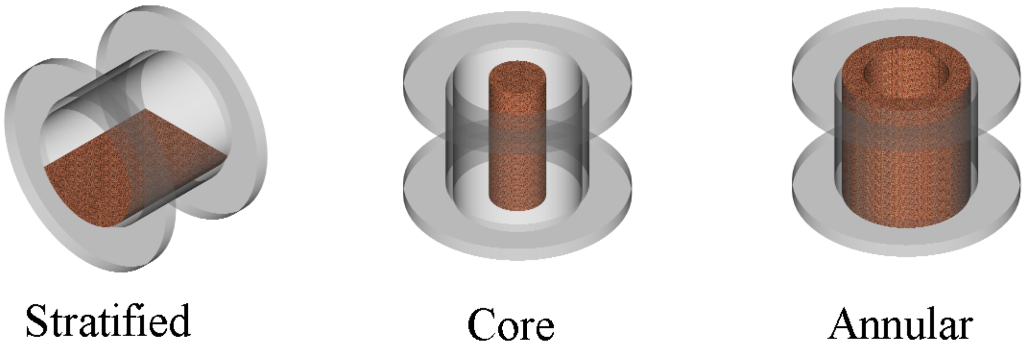

Figure 3.3 Examples of Typical Solids Flow Patterns

Flow regime dependence upon can be reduced by using multiple sensing electrodes whose output can be switched electronically to produce a rotating field across the pipe section (Figure 3.4) [20].

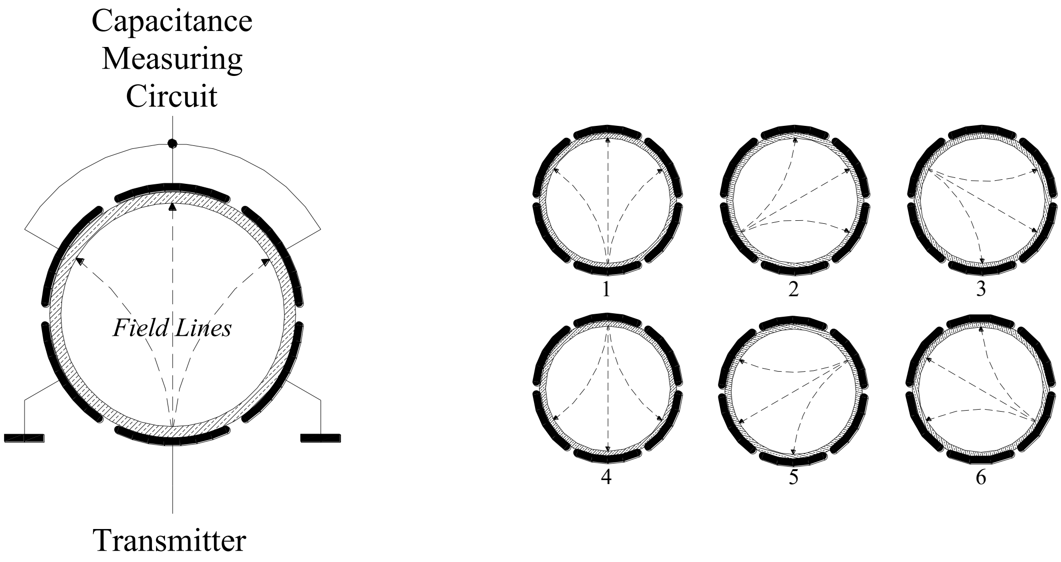

Figure 3.4 Capacitance Sensor with a Rotating Field

Using the rotating field method reduces the sensor's overall response time. A much better sensing performance can be achieved by using an additional pair of electrodes which are offset and placed axially near to the first pair of sensors (Figure 3.5) [21].

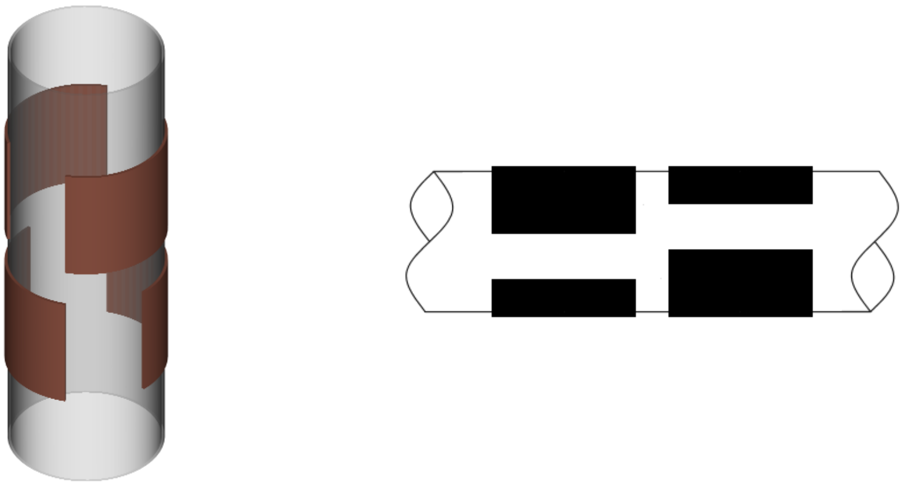

Figure 3.5 The Capacitance Sensor with Compound Offset Electrodes

The two fields created by each sensor compensate for each other and by taking an averaged value from the two sensors results in an improved immunity to flow regime susceptibility.

3.3 Flow Velocity Measurement

The pneumatic conveying of solid material, such as polypropylene pellets, is essentially a solids-gas (polypropylene pellets and air) two-phase mixture. But since it is the flow of the solids and not the air that is of primary interest, solids flow can be effectively treated in this case, as a single-phase solids flow.

As outlined in Chapter 1, Section 1.2.2, the cross correlation of signals taken from upstream and downstream flow sensors determines the solids velocity. A non-intrusive capacitive flow velocity sensor is shown in Figure 3.6.

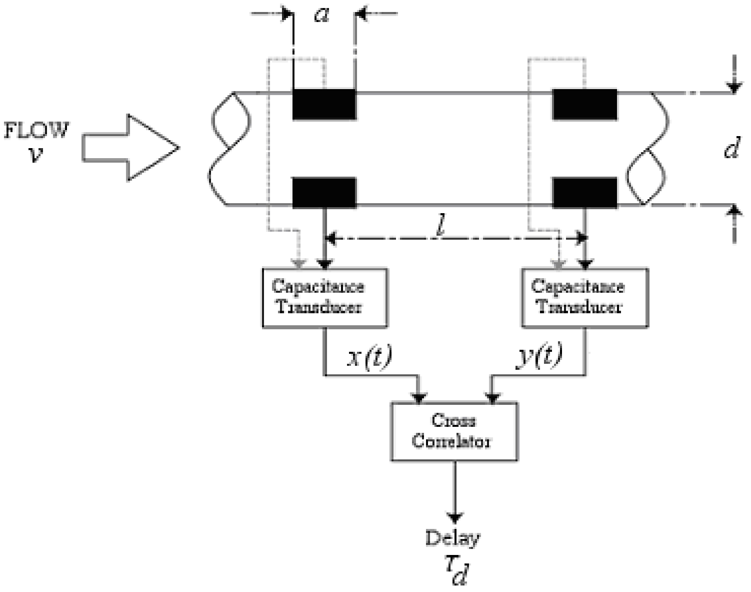

Figure 3.6 Non-intrusive Capacitive Flow Velocity Sensor

The sensor consists of two sets of electrodes of length a (m) mounted on a tube of diameter d (m) and axially spaced l (m) apart. The dielectric noise caused by the flow of non-conductive material passing through the sensor is converted into electrical signals $x(t)$ and $y(t)$. The principal of flow velocity measurement by cross correlation is to use the cross correlation function to determine the transit time (delay), τ_d (s), between the upstream and downstream signals (Figure 3.7).

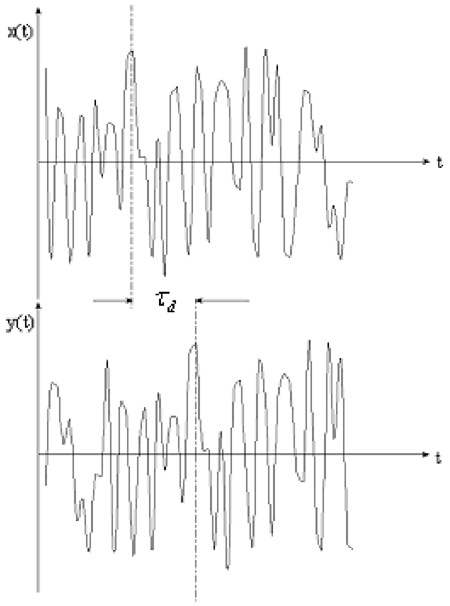

Figure 3.7 Transit Time between Upstream and Downstream Signals

The possible statistical dependence or correlation between two different random signals $x(t)$ and $y(t)$ is expressed by the cross-correlation function:

$$R_{xy}(\tau) = \lim_{T\to\infty} \frac{1}{T}\int_0^T x(t)y(t+\tau)dt$$ **Equation 3.1**

The maximum value of $R_{xy}(\tau)$ will occur at $\tau = \tau_d$ (Figure 3.8).

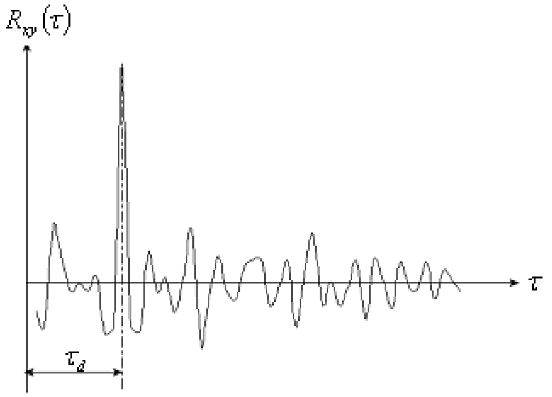

Figure 3.8 The Cross Correlation Function

Thus the flow velocity v ($m s^{-1}$) is given by Equation 3.2.

$$v = \frac{l}{\tau_d}$$ **Equation 3.2**

Where:

v is the flow velocity $\left(\frac{m}{s}\right)$.

l is the distance between sensors (m).

τ_d is the transit time between the upstream and downstream sensors (s).

Conceptually, the cross correlation function can be described as the average of the product of the signal $x(t)$ and the time delayed signal $y(t)$.

The bandwidth of the sensor is related to the axial length of the sensor a (m) and the flow velocity v (m s^{-1}) and is given by the transfer function [22]:

$$|H(j\omega)| = \left| \frac{\sin\left(\frac{\omega a}{v}\right)}{\frac{\omega a}{v}} \right| \qquad \textbf{Equation 3.3}$$

The transfer function is shown graphically in Figure 3.9, where the first zero of the transfer function is the effective cut-off frequency which can be determined from Equation 3.4.

$$f_c = \frac{v}{a} \qquad \textbf{Equation 3.4}$$

Where:

f_c is the cut-off frequency of the sensor (Hz).

v is the flow velocity $\left(\frac{m}{s}\right)$.

a is the sensor length (m).

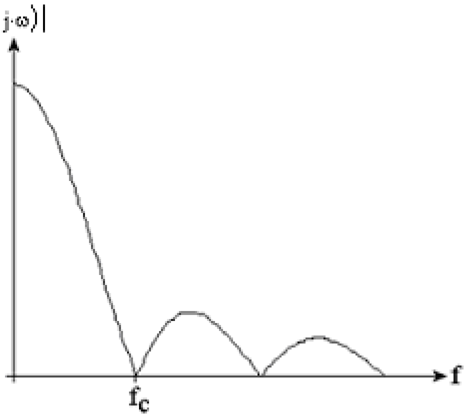

Figure 3.9 Theoretical Transfer Function of Sensor

As it can be seen from Equation 3.4, the shorter the length of the sensor the greater the sensor's bandwidth which leads to a sharper correlation peak making it more accurate and easier to detect (Figure 3.10) [23]. So the length of the sensor and intended measured flow velocity are the main parameters to consider in the design of cross correlation flow sensors.

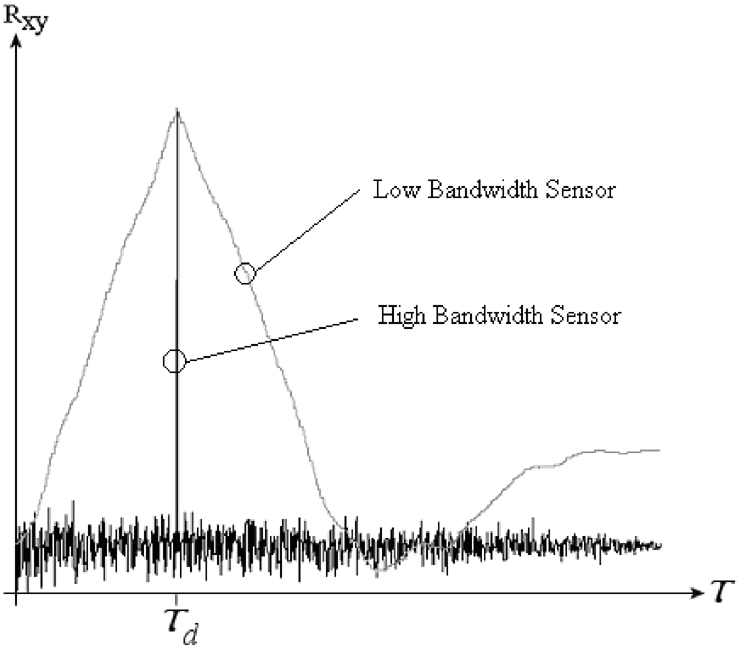

Figure 3.10 Comparison between the Affect of Sensor Bandwidths on the Cross Correlation Function

The least critical parameter in cross correlation flow measurement is the axial spacing between the upstream and downstream sensors. If large axial sensor spacing's are used, in addition to increased correlation times, there is a possibility of decreased accuracy in the cross correlation attributable to reduced signal similarity due to the break up of the turbulence pattern as it proceeds along the pipe. Beck and Plaskowski state the accuracy is optimum at a axial sensor spacing of between three and four pipe diameters [24].

3.4 Mass Flow Measurement

Non-intrusive mass flow instruments can be divided into two types, direct (or true) and inferential. Direct mass flow techniques employ a sensing element that responds directly to the mass flow of solids passing through the sensor. These instruments achieve this usually by either measuring the Coriolis force or the heat transfer of the flow passing through the sensor. Mass flowmeters of this type have only been successful commercially when the flow medium is either a liquid or, a dense phase solid such as pulverised fuel transported through relatively small pipes [20, 25].

3.4.1 Direct Mass Flow Measurement

A possible non-intrusive method of directly measuring the mass flow of non-conductive solids material was proposed by Green et al [26]. This method is based on the proposition that due to intrinsic turbulence, solids flow can be regarded as a mixture of flow noise and the overall average flow. It has been found experimentally that a direct correlation between flow noise and mass flow exists which can be measured to give the mass flow of the conveyed material. A block diagram of the mass flowmeter is shown in Figure 3.11. A capacitive sensor located on the walls of the conveyer is connected in parallel with an inductor to form a tuned circuit controlling the frequency of an oscillator. The change in permittivity within the capacitive sensor, created by the flow of non-conducting solid material passing between the sensor plates, changes the frequency of the oscillator to produce a frequency modulated (FM) signal the frequency which changes in relation to both the average flow and the superimposed noise flow.

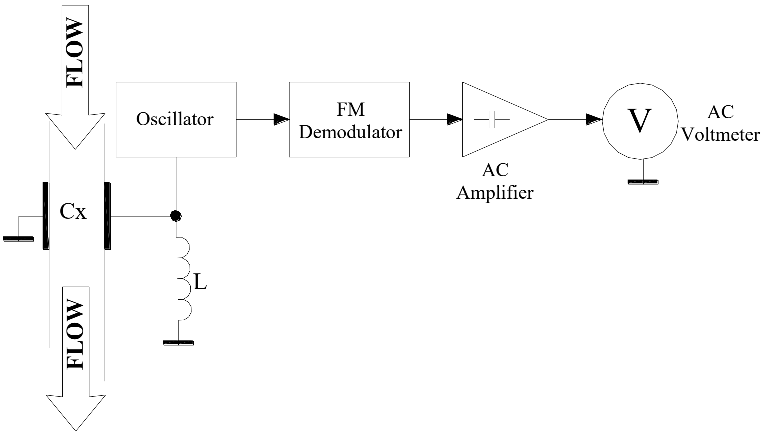

Figure 3.11 Block Diagram of the Solids Mass Flowmeter Transducer

The frequency modulated signal is converted into corresponding voltage changes by a FM demodulator circuit. The average flow signal changes relatively slowly compared to the flow noise signal. The use of an AC amplifier will remove the average flow signal leaving only the signal of interest, the flow noise signal at the output of the AC amplifier. This is passed to an AC voltmeter which is calibrated to display mass flow.

3.4.2 Inferential Mass Flow Measurement

Inferential mass flow methods involve the measurement of flow rate $\left(m\,s^{-1}\right)$ and volumetric concentration separately, from which the mass flow rate can be deduced [27]. Based on Equation 1.1, the inferred mass flow rate $\left(kg\,s^{-1}\right)$ is given by Equation 3.5.

$$\dot{m} \qquad\qquad \beta$$ **Equation 3.5**

Where:

$\dot{m}$ is the mass flow rate $\left(\frac{kg}{s}\right)$.

ρ is the true density of the solids material $\left(\frac{kg}{m^3}\right)$.

A is the cross sectional area of the pipe $\left(m^2\right)$.

v is the solids velocity $\left(\frac{m}{s}\right)$.

β represents volumetric concentration and is defined as the cross sectional area of the moving solids normalised with respect to the pipe's cross sectional area.

Where:

$$\beta = \frac{A_s}{A}$$ **Equation 3.6**

A_s is the cross sectional area occupied by a moving solid $\left(m^2\right)$.

β is dimensionless and has a value of $0 \le \beta \le 1$.

Besides mass flow, the inferential also provides knowledge of both the solids velocity and volumetric concentration and can provide invaluable information leading to the reduction of pipeline wear and breakage of material, as well as overall energy savings, during the transportation process.

3.5 A Practical Capacitance Based Mass Flow Measurement System

The Granucor flow measurement system produced by the Thermo Electron Corporation is an inferential mass flow measurement system (Figure 3.12). It can be used with dense phase pneumatically conveyed bulk solids or gravity conveyed materials to provide real-time flow measurement of flow velocity, solids concentration, mass flow rate and the total flow over a fixed period of time. The Granucor system is composed of two non-invasive independent sensors DK 13 velocity sensor and the DC 13 concentration sensor both of which are based on steady state capacitive sensing techniques.

Figure 3.12 The Granucor Capacitance Flow Measurement System. Comprising of the DK 13 Velocity Sensor, DC 13 Concentration Sensor and MicroTech Correlator/Integrator

The main function of the MicroTech correlator/integrator is to processes the signals taken from the two sensors to determine flow rate by cross correlation and combined with the concentration value calculate the mass flow rate. A typical flow setup arrangement is shown in Figure 3.13 [28].

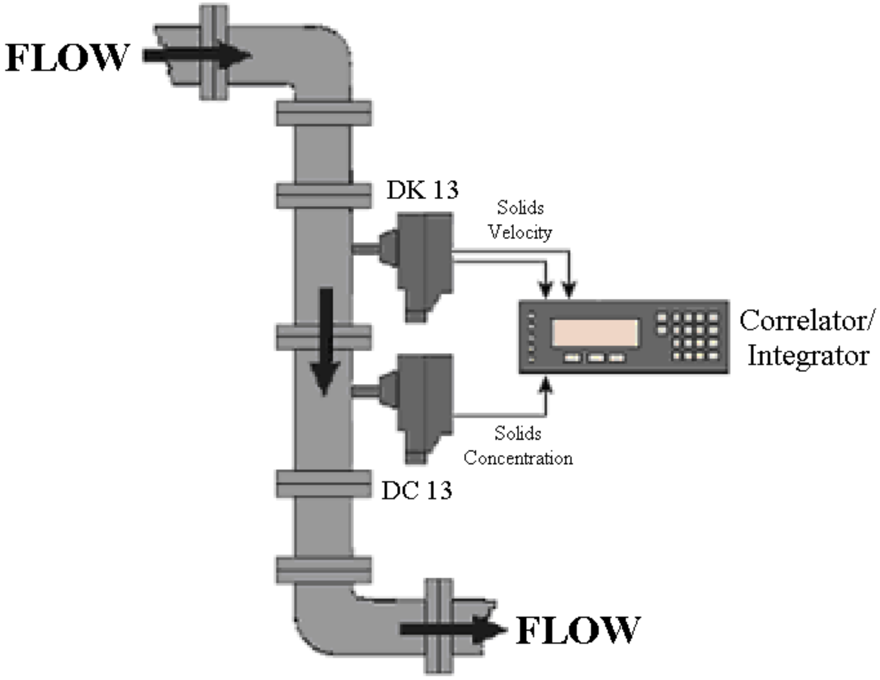

Figure 3.13 Typical Flow Measurement Setup

The internal structure of the DK 13 velocity sensor and DC 13 concentration sensor is shown in Figure 3.14. The 150mm inner tube consists of sensor electrodes mounted on epoxy resin which is protected by a lacquered steel outer tube, which also act as a screen for the capacitor and the space between the inner and outer tube is filled with polyurethane foam to give the sensor mechanical stability. Each end of the tube is fitted with a standard DIN 150lb mounting flange with the sensors signal conditioning electronics contained within a steel box mounted to the outer tube (Figure 3.12).

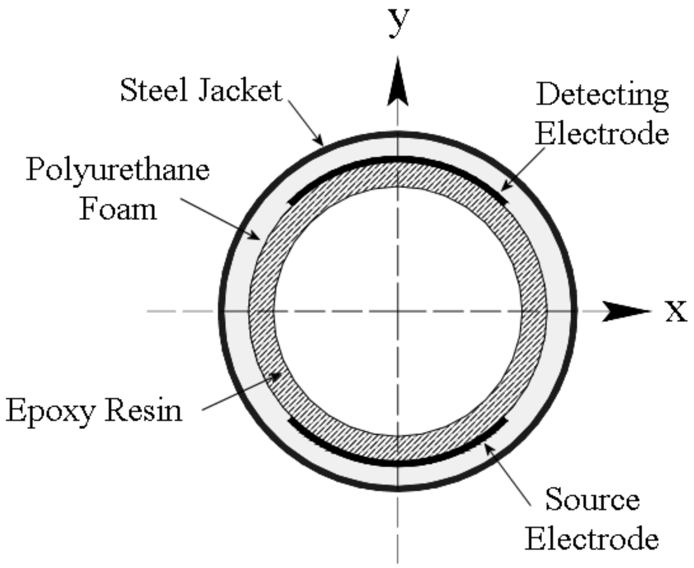

Figure 3.14 The Internal Structure of the DK 13 and DC 13 Sensors

3.5.1 The DK 13 Velocity Sensor

The DK 13 velocity sensor consists of a measuring tube and signal conditioning electronics, the internal electrode arrangement consists of a long electrode running nearly the full length of the inner tube on one side of the tube and a series of six electrodes spaced at various distances on the opposite side of the inner tube (Figure 3.15).

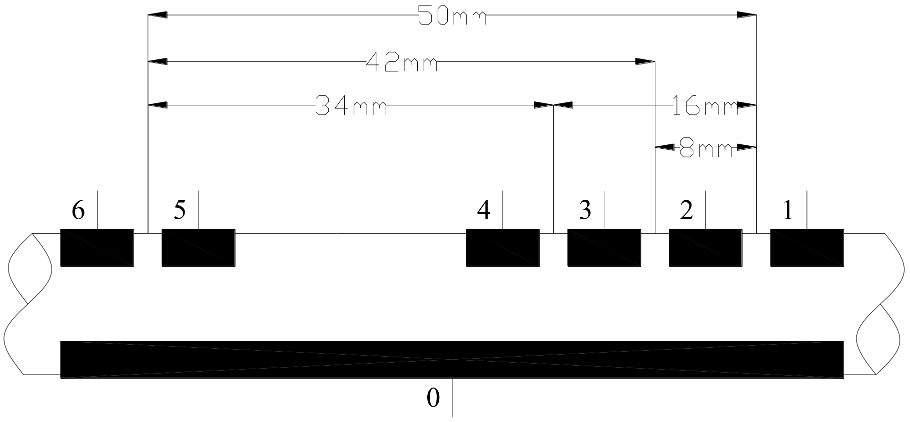

Figure 3.15 DK 13 Internal Electrode Array

By using various permutations when connecting the sensor to the signal conditioning electronics, makes it possible to adjust the axial spacing between the sensors in the range of 8mm to 50mm.

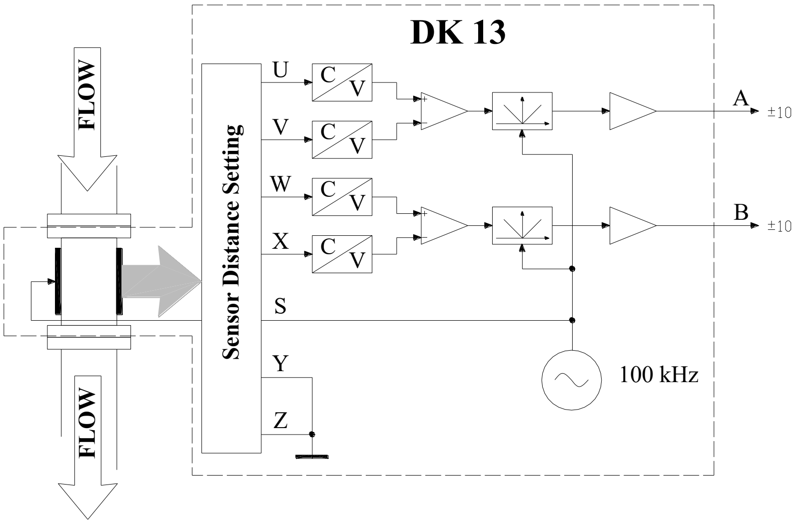

Figure 3.16 DK 13 Flow Velocity Sensor Signal Conditioning Electronics Block Diagram

Figure 3.16 shows a block diagram of the DK 13 flow velocity sensor's electronics, random flow noise created by changes in sensor capacitance caused by the presence of solids material passing through the two sensors. This change in capacitance, amplitude modulates the two 100 kHz detecting electrode signals which are then demodulated by the phase sensitive detectors. The two signals are then amplified to produce two ±10V noise signals ready for cross correlation.

3.5.2 The DC 13 Concentration Sensor

Figure 3.17 shows a block diagram of the DC 13 concentration sensor's electronics. Changes in sensor capacitance caused by the presence of solids material inside the sensor vessel are directly proportional to the volumetric concentration of the solids. This change in capacitance alters the amplitude of the 100 kHz detecting electrode signal which is then phase sensitively rectified to convert it into a DC value. This is used to determine the frequency of a pulse stream, the frequency of which is proportional the volumetric concentration of the solids.

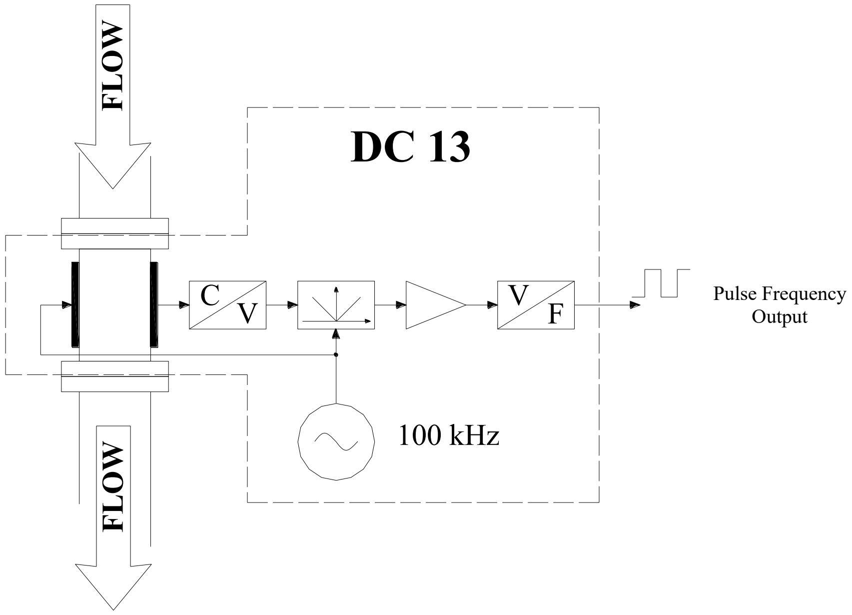

Figure 3.17 DC 13 Concentration Sensor Signal Conditioning Electronics Block Diagram

The sensor is pre-calibrated before use by filling the sensing vessel with a known grade of solids.

Yan and Reed performed an experimental evaluation on the concentration sensor with various materials [29] and found that beside flow dependency, the overall accuracy of the sensor is significantly affected by materials temperature and moisture content.

Chapter Four

4 Electrical Capacitance Tomography (ECT)

4.1 Introduction

Tomography can be described as the technique of generating a two dimensional cross sectional image, or tomogram, of a three dimensional object from a series of non-invasive measurements. Initially developed for medical applications, tomographic measurement techniques have been adapted in recent years by the chemical and process engineering industries. Non-invasive visualisation of cross sectional flow concentration and velocity profiles of solids, liquids or gases in pipelines or vessels used as part of an industrial process, leading to improved product quality and process efficiency. In order to distinguish this area of tomography from its medical counterpart, industrial tomography is specifically referred to as Industrial Process Tomography or simply, Process Tomography (PT).

Process tomography systems have to be relatively cheap, simple to use, portable and be robust enough to function in an industrial environment; it also must be able to operate fast enough to non-intrusively produce cross sectional images of non-static moving objects. Lower resolution Electrical Impedance Tomography (EIT) imaging techniques based on the measurement of the electrical properties of materials (resistive, capacitive or, inductive) has been proven to be predominantly successful in meeting the required criteria for industrial tomographic imaging systems [2].

Electrical Capacitance Tomography (ECT) is a branch of EIT which involves the use of a capacitive sensor to obtain information about the spatial distribution of non-conducting dielectric materials inside closed pipes or vessels in order to visualise the cross-sectional distribution of permittivity.

This chapter introduces the underlying principles of Electrical Capacitance Tomography by looking at the core components of an electrical capacitance tomography imaging system. The chapter then discusses the principals of ECT measurement strategies, sensor design and image reconstruction. The chapter finishes by examining two of the major types of capacitance measuring circuit strategies used for ECT, explaining the operation and the advantages and disadvantages of each circuit in turn.

4.2 Electrical Capacitance Tomography Overview

The core components of an electrical capacitance tomography imaging system are shown in Figure 4.1.

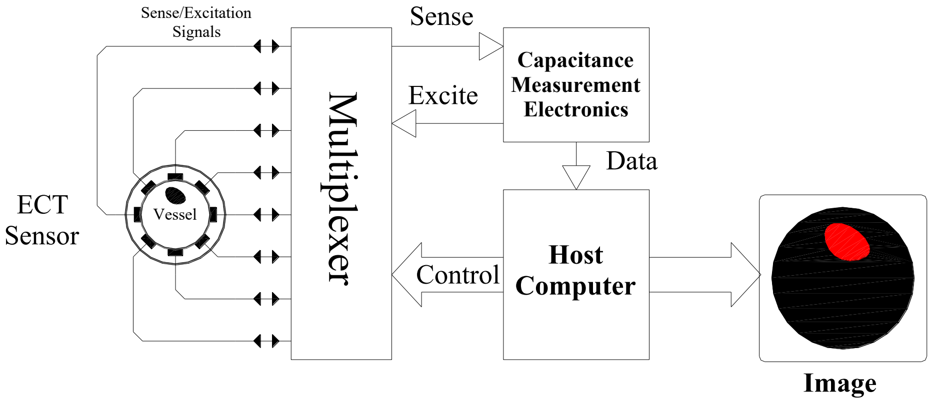

Figure 4.1 The Core Components of an ECT Imaging System

The sensor used to measure the permittivity distribution of non-conducting dielectric materials inside a the vessel ($\varepsilon(X,Y)$), is comprised of a set of electrodes (typically 8 or 12) symmetrically placed either on the inside or outside of an insulated vessel (Figure 4.2) [30, 31].

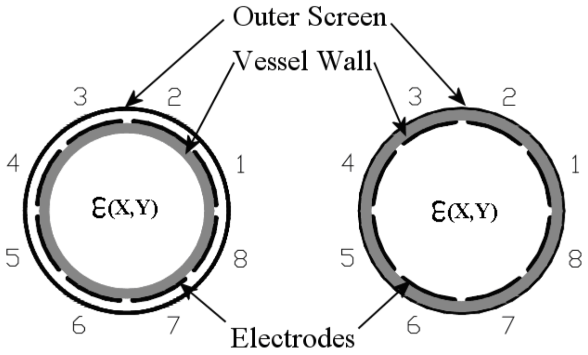

Figure 4.2 Cross-sectional View of an ECT Sensor with External and Internal Electrode Configurations

In a serial measurement strategy, each electrode is energised as a source electrode turn by turn and the electrical changes on the remaining electrodes are then measured. For an N electrode system, firstly electrode 1 would be energised and the resulting currents from electrode 2 through to electrode N would be measured in turn. Next electrode 2 would be energised and the resulting currents from electrode 3 through to electrode N would then be measured. This process is repeated until all possible electrode pair combinations have been covered which finally concludes when electrode $N-1$ is the energised electrode and electrode N is the measured electrode. All possible measurement pair combinations for an 8 electrode system are shown in Figure 4.3, which shows in total, 28 possible electrode pair combinations.

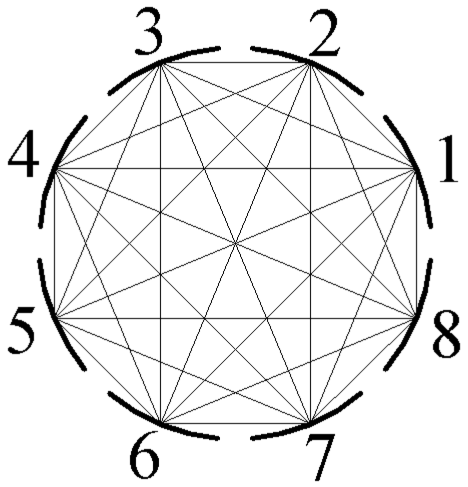

Figure 4.3 Electrode-Pair Combinations for an 8 Electrode Sensor

The total number of possible independent electrode pair combinations *M*, for an *N* electrode system is given by Equation 4.1.

$$M = \frac{N(N-1)}{2}$$ **Equation 4.1**

The path of the signals applied to or taken from the sensor is selected by a multiplexer controlled by the host computer (Figure 4.1).

Measurement electronics convert capacitance changes detected within the vessel into analogous voltage changes ready to be processed and ultimately converted into a cross-sectional image by the host computer.

The role of the host computer is to perform three functions; firstly, it is used to control the associated hardware of the imaging system, secondly, it is used as a data acquisition system to collect and store measurements executed by the associated hardware. Finally, it is used to process the collected data to reconstruct and display the tomographic image.

4.2.1 The ECT Sensor

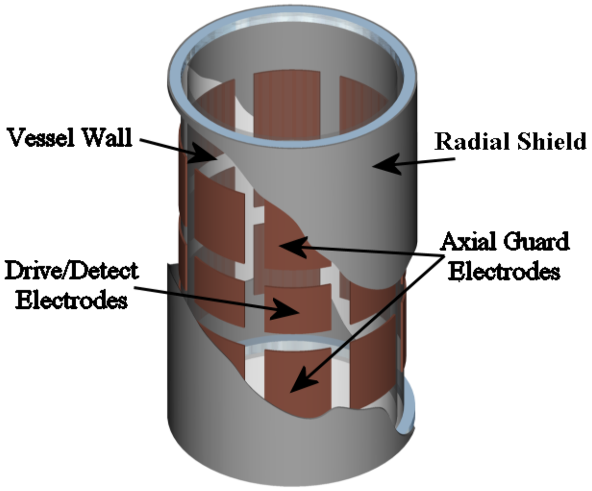

Figure 4.4 A Typical ECT Sensor

Figure 4.4 shows a cutaway 3D representation of a typical ECT sensor. As stated previously, the capacitance transducer segment of the sensor is comprised of a set of drive/detect electrodes symmetrically placed either on the inside or outside of an insulating vessel. The decision whether to mount the sensing electrodes on the inside or outside of the vessel wall is dependant upon on the following factors; accuracy, contact with materials and ease of construction. Electrodes mounted on the outside walls of the insulating vessel are simpler to construct and are truly non-invasive but, the presence of the sensor wall introduces an extra series coupling capacitance in addition to the inter-electrode capacitances, causing a non linear response with respect to the changes in permittivity inside the vessel. Electrodes mounted on the inside walls of the insulating vessel are more difficult to construct and have some contact with the materials within the vessel, but have the highest accuracy due to the fact that they do not suffer the nonlinearity problem associated with externally mounted electrodes [31, 32].

The actual number and dimensions of electrodes used is a trade off between axial and radial resolution, sensitivity and image capture rate. A high electrode number with smaller dimensions will give a high resolution at the expense of measurement sensitivity and because more measurements will need to be taken (Equation 4.1) a reduced image capture rate. Fewer electrodes with larger dimensions improve measurement sensitivity and image capture rate whilst reducing image resolution [31].

Axial guard electrodes placed at either end of the measurement electrodes (Figure 4.4), reduce electrical noise and improve the axial resolution and the sensitivity of the sensor by preventing the fringing of electric field lines from each end of the set of measurement electrodes [33].

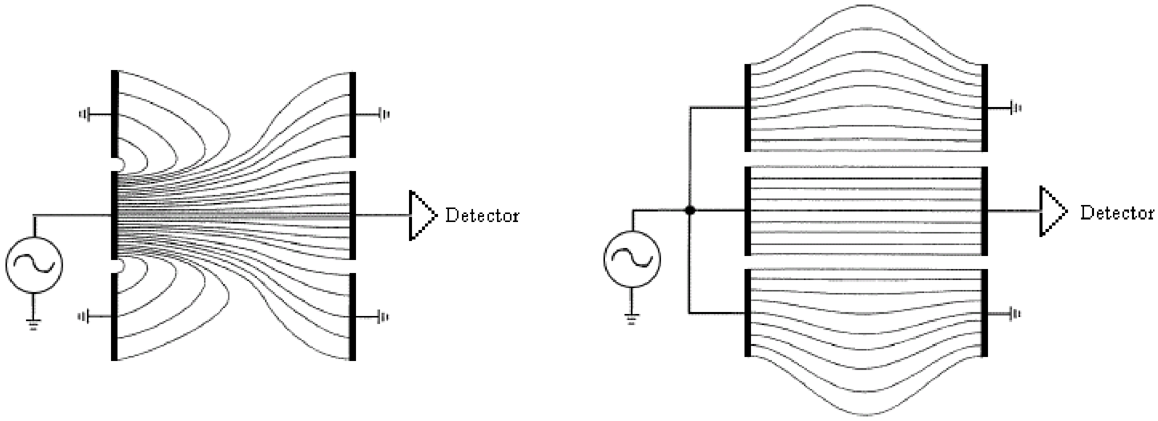

(a) (b)

Figure 4.5 Representations of the Electrical Field for (a) Grounded and (b) Driven Axial Guard Electrodes

Figure 4.5 compares the affect on the electrical field inside the sensing area when (a), the axial shield is grounded and (b), one side of the axial guard electrodes are grounded whilst the other side is driven from the same voltage source as the measurement electrode thus producing a more homogeneous electric field improving the axial resolution and sensitivity of the sensor [33, 34]. A grounded radial shield placed around the whole sensor protects the sensor from corruption by any external field interference and variations in stray capacitance between the sensor and earth.

4.2.2 Image Reconstruction

4.2.2.1 Normalisation

As stated previously, the tomographic imaging system shown in Figure 4.1 converts then collects capacitance changes detected within the vessel into a series of analogue voltage changes. Each measured voltage of the collected voltage series and (subsequently derived) permittivities are then normalised [35, 36] prior to image reconstruction. The main advantages of normalisation are [35];

- It eliminates the need to know the dielectric constants of the individual materials inside the vessel.
- The widely different ranges of capacitance measurements, permittivity values and image values are standardised to a single measurement range from 0 to 1.
- Errors introduced by the image capture hardware such as offset and drift are reduced.
- Straightforward sensor calibration can be accomplished.

Sensor calibration is performed by filling the vessel with two reference materials in turn and by measuring the resulting voltage values at these two extreme values of relative permittivity.

The normalised value V_N of the measured voltage is given by Equation 4.2.

$$V_N = \frac{V_M - V_L}{V_H - V_L} \qquad \textbf{Equation 4.2}$$

Where:

V_M is the measured voltage value corresponding to the inter-electrode capacitance (V).

V_L is the measured value corresponding to the inter-electrode capacitance when the vessel is completely filled with the lower permittivity reference material (V).

V_H is the measured value corresponding to the inter-electrode capacitance when the vessel is completely filled with the higher permittivity reference material (V).

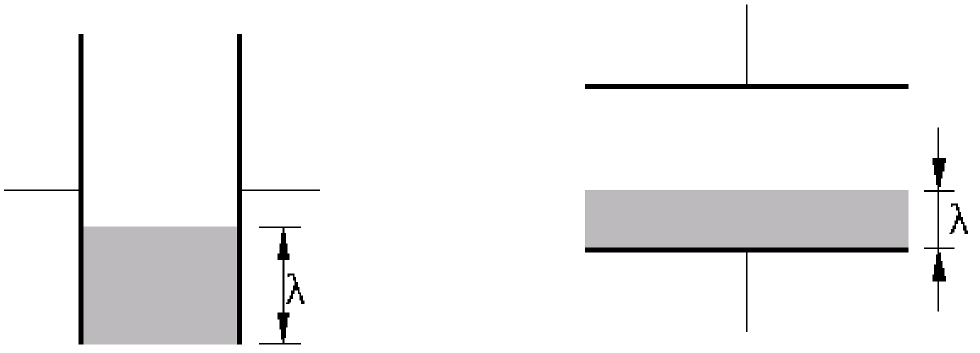

(a) (b)

Figure 4.6 Capacitance Cell Containing (a) Vertically Stratified Material and (b). Horizontally Stratified Material

If the distribution of the higher permittivity material is vertically stratified within the sensing vessel (Figure 4.6a), the volume of the vessel taken up by the higher permittivity material λ, is linearly proportional to the normalised value of the measured voltage given by Equation 4.2. Conversely, if the distribution of the higher permittivity material is horizontally stratified within the sensing vessel (Figure 4.6b) or a mixture of both horizontal and vertical distributions (homogeneous), the volume of the vessel taken up by the higher permittivity material λ, is not linearly proportional to the normalised value of the measured voltage V_N [35]. This non-linearity can be corrected by multiplying the normalised value of the measured voltage given by Equation 4.2 (V_N) by some correction factor (CF) whose value is dependant upon the expected distribution of material inside the measuring vessel (Equation 4.3).

$$V_{NC} = V_N CF \qquad \textbf{Equation 4.3}$$

Where:

V_{NC} is the normalised and corrected measured voltage.

V_N is the normalised measured voltage given by Equation 4.2.

CF is a suitable correction factor whose value is dependant upon the expected distribution of material inside the measuring vessel (see Table 4.1).

Distribution	**Distribution Model [35]**	**Correction Factor (CF)**
Vertical	Parallel	1
Horizontal	Series	$\frac{V_R}{1+V_N(V_R+1)}$
Homogeneous	Maxwell	$\frac{2+V_R}{3+V_N(V_R-1)}$

Table 4.1 Normalised Voltage Correction Factors

Where:

V_N is the normalised measured voltage given by Equation 4.2.

V_R is the ratio of V_H to V_L, obtained from sensor calibration.

4.2.2.2 Linear Back Projection (LPB)

The permittivity image of two different materials inside the sensor with diverse permittivities is often displayed as pixels located on a square pixel grid; an appropriate graduated colour scale is used to indicate the magnitude of the normalised pixel permittivity.

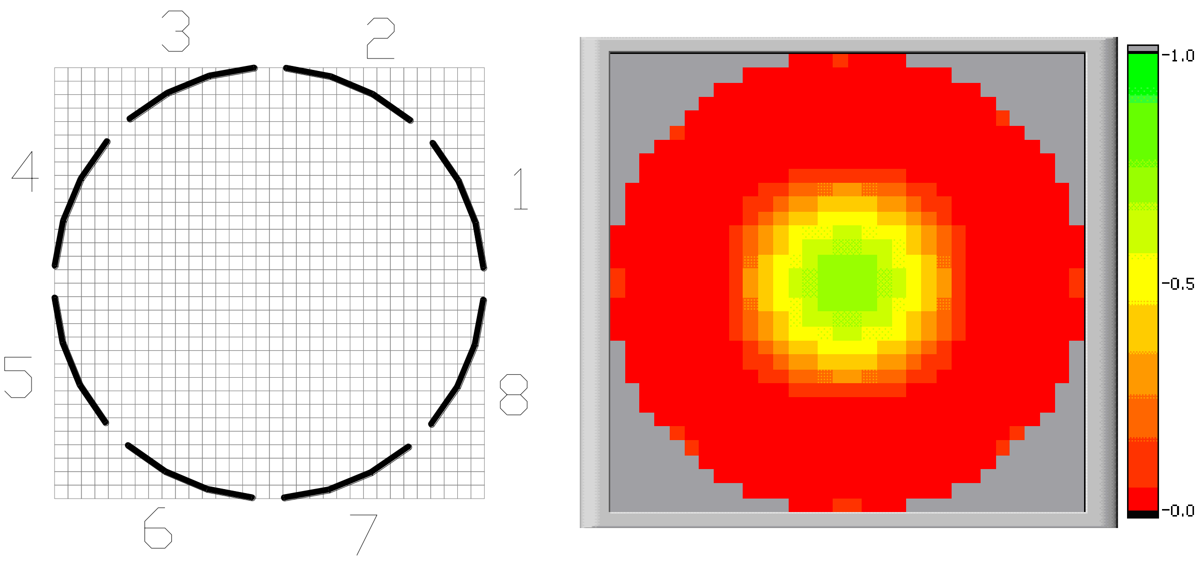

(a) (b)

Figure 4.7 (a) A 1024 Pixel Grid (32 x 32 Pixels) Used to Image the Contents of a Circular Vessel Fitted with 8 Electrodes and (b) ECT Image of a Perspex Rod Placed Inside an Air Filled Sensor

Figure 4.7(a), shows a 32 by 32 square pixel grid used to display the permittivity distribution image of a circular 8 electrode sensor. The image relates only to the pixels contained inside the boundary of the sensor, so only 812 pixels (P) are required to recreate the normalised permittivity image, all pixels outside the sensor's periphery are discarded. Figure 4.7(b) shows an example of a reconstructed permittivity image of a perspex rod placed inside an air filled sensor. The normalised permittivity value is indicated by a graduated red/yellow/green colour scale, a value of zero (the red area) indicates the presence of the lower permittivity material used during sensor calibration (air). A value of one, the green area, indicates the presence of the higher permittivity material used during sensor calibration (perspex).

Linear back projection is based on the forward problem which assumes that a linear relationship exists between permittivity distribution and measured capacitance. The forward problem (Equation 4.4) determines the inter-electrode capacitances for any arbitrary distribution of permittivity values inside the sensor [37].

$$[C]=[S][K]$$ **Equation 4.4**

Where:

$[C]$ is a M by 1 matrix of normalised independent electrode pair capacitance combinations. M is given by Equation 4.1 (28 for an 8 electrode sensor).

$[S]$ is a M by P matrix containing a set of sensitivity values for every electrode pair commonly referred to as the sensor's sensitivity map. P is the number of pixels representing the sensor's cross section on the image grid (Figure 4.7a).

$[K]$ is a P by 1 matrix containing the normalised pixel permittivity distribution (0 to 1).

The key to the solution of Equation 4.4 is the determination of the relationship between the set of capacitance values obtained, relative to the pixel position of higher permittivity material within the measurement grid. This relationship is established by the sensors sensitivity matrix or map [37].

Plates 1-2 Plates 1-3

Plates 1-4 Plates 1-5

Figure 4.8 The Four Primary Sensitivity Maps for an 8 Electrode Sensor

In the case of a circular sensor an accurate map can be obtained analytically but for more complex sensor geometries, numerical methods such as finite element modelling have to be employed [30, 38]. For symmetrical sensor configurations it is only necessary to calculate a few primary sensitivity maps for the unique electrode pairings as the rest can be derived by either reflection or rotation (Figure 4.8).

Ideally Equation 4.4 can be solved to give the permittivity distribution from the measured capacitances (backward problem) to give Equation 4.5.

$$[K]=[S]^{-1}[C]$$ **Equation 4.5**

But the fact that the sensitivity matrix obtained from the forward problem is non-square (dimensions M by P), implies that there in no analytical solution to Equation 4.5, thus making it unusable as a basis for image reconstruction. But it can be argued that a useable approximation of the permittivity distribution can be obtained by means of the transform of the sensitivity matrix (Equation 4.6) [30].

$$[K]=[S]^{T}[C]$$ **Equation 4.6**

Equation 4.6 can be restated to give a set of normalised permittivity image values G, in terms of the normalised measured voltage value V_{NC} (Equation 4.7).

$$[G]=[S]^{T}[V_{NC}]$$ **Equation 4.7**

Where:

$[G]$ is the normalised grey level image vector.

$[V_{NC}]$ is the normalised and corrected measured voltage vector (see Section 4.2.2.1).

The popularity of the linear back projection method is due to the fact that it is fast and relatively simple to implement which makes in suitable for online process monitoring. But the reproduced image suffers low spatial resolution, due to image blurring, thus giving only qualitative images of sensor permittivity distributions. This blurring affect can be attributed to the following factors [30, 38, 39];

- ECT is intrinsically a soft field method means that the electric field is distorted by the material distribution inside the sensor. This makes the relationship between permittivity distribution and measured capacitance non-linear (LBP assumes a linear relationship).

- The number of capacitance measurements taken is less than the number of pixels defined by the grid which makes it impossible to obtain a unique solution for each image pixel.
- A non-linear electric field inside the sensor. The magnitude of the electric field generated within the ECT is strongest near the wall area and weakest at its centre.

Various other image reconstruction algorithms exist which greatly improve image quality such as the iterative method [40] which is based on the use Equation 4.4 and Equation 4.6 alternately, to progressively correct the displayed pixel values. This method is a trade off between image quality and speed of execution, because of the time taken to carry out the repetitive calculations needed in order to produce the required image quality. Faster single step methods such as the Landweber or Tikhonov transform [9, 30, 41] improves image quality without the overhead of execution time. These methods involve the use of advanced mathematical concepts to find the inverse transform of the sensitivity matrix $[S]^{-1}$ in Equation 4.5.

4.2.3 Capacitance Measuring Circuits

As introduced in at the start of this chapter (see Figure 4.1) a capacitance measuring circuit converts the capacitance changes detected within the vessel into analogue voltage changes. A suitable capacitance measurement circuit strategy for ECT should be highly stable with a good signal to noise ratio, fast dynamic response, low baseline drift and be stray capacitance immune.

4.2.3.1 Stray Immunity

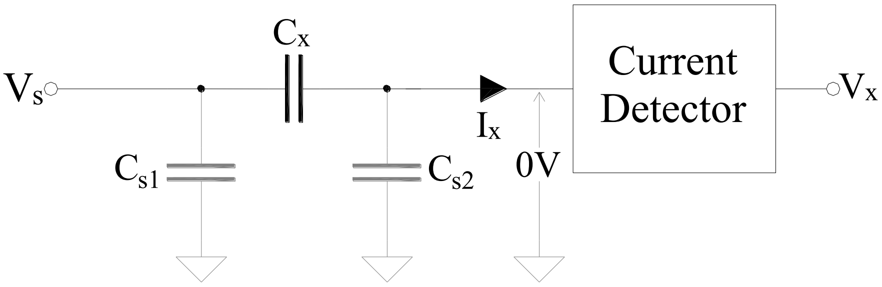

Figure 4.9 Intrinsically Stray-Immune Circuit Configuration

Because of their stray immunity, two types of circuit are considered as most suitable for use in ECT systems, the charge/discharge and the AC-based circuit [42, 43]. Both the charge/discharge and AC-based circuit operate in an essentially similar manner (Figure 4.9). One end of the unknown capacitance C_x is connected to a voltage source V_s and the other end to the low impedance input of a current detector. The stray capacitances, mainly caused by the capacitance between the earthed screen (see Section 4.2.1) and the connection between the capacitance transducer and its measuring circuit, is represented in Figure 4.10 by C_{s1} and C_{s2}. As C_{s1} is connected directly between the voltage source and ground, the current passing through C_{s1} has no contribution to the overall measurement. C_{s2} is connected between the input of the current detector and ground. Due to the low impedance input of the current detector, the potential difference across C_{s2} is negligible and has only a slight effect on the overall capacitance measurement.

4.2.3.2 Differential Charge/Discharge Measuring Circuit

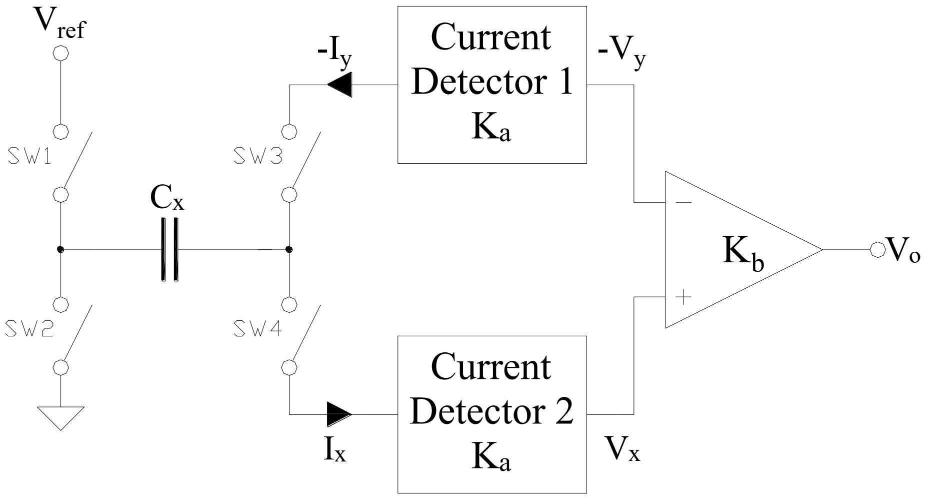

Figure 4.10 Differential Charge/Discharge Measurement Circuit

The circuit shown in Figure 4.10 [42], consists of two (low impedance input) current detectors of transimpedance K_a, a differential amplifier of gain K_b, and four switches SW1 to SW4 operated as two pairs (SW1,SW4 and SW2,SW3). Each pair is turned on and off with a 180° phase shift which alternately charges and discharges the unknown capacitance (C_x) over the period T (Figure 4.11).

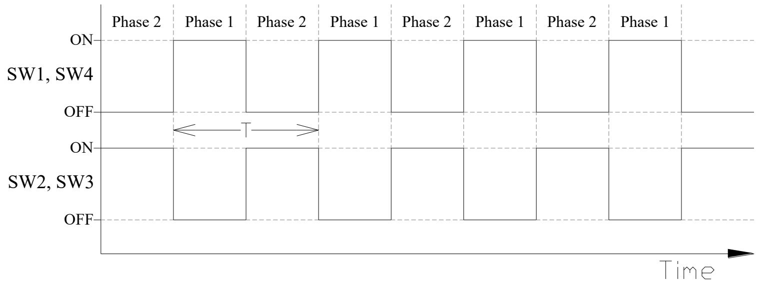

Figure 4.11 CMOS Switch Control Signals

During phase one of the charge/discharge cycle, CMOS switches SW1, SW4 are switched on and SW2, SW3 are switched off. This allows the unknown capacitance C_x to charge to potential V_{ref}. A charging current, proportional to the unknown capacitance, flows into current detector 2 which in turn is averaged out by the detector to produce a DC voltage V_x. The DC voltage output from detector two is given by Equation 4.8.

$$V_x = K_a V_{ref} C_x f + V_{off} \qquad \textbf{Equation 4.8}$$

Where:

V_x is the DC output voltage from current detector two (V).

K_a is the transimpedence of the current detector (Ω).

V_{ref} is the reference voltage (V).

C_x is the unknown capacitance (F).

f is the frequency of the charge/discharge cycle (Hz).

V_{off} is a DC voltage offset due to baseline drift caused by variations in V_{ref}, f, K_a and, (V).

During phase two of the charge/discharge cycle, CMOS switches SW2, SW3 are switched on and SW1, SW4 are switched off. This discharges the unknown capacitance C_x (previously charged to potential V_{ref}) drawing current, again proportional to the unknown capacitance, from detector one which in turn is averaged out by the detector to produce a DC voltage V_y. The DC voltage output from detector one is given by Equation 4.9.

$$V_y = -K_a V_{ref} C_x f + V_{off}$$ **Equation 4.9**

Where:

V_y is the DC output voltage from current detector two (V).

The final DC measurement voltage output V_o from the differential amplifier is given by;

$$V_o = K_b (V_x - V_y)$$ **Equation 4.10**

Substituting for V_x and V_y into Equation 4.10 gives;

$$V_o = 2K_a K_b V_{ref} C_x f + K_b (V_{off} - V_{off})$$ **Equation 4.11**

As it can be seen from Equation 4.11, the baseline drift voltage (V_{off}) is cancelled out by the differential amplifier.

The main advantage of this type of capacitance measuring circuit is its simplicity of operation and low cost when compared to other types of circuits. Reduced measurement accuracy caused by the injection of additional charge into the current detectors due to the use of CMOS switches is a major problem for this type of circuit, which requires the need for frequent system recalibration [43, 44].

4.2.3.3 AC Based Measuring Circuit

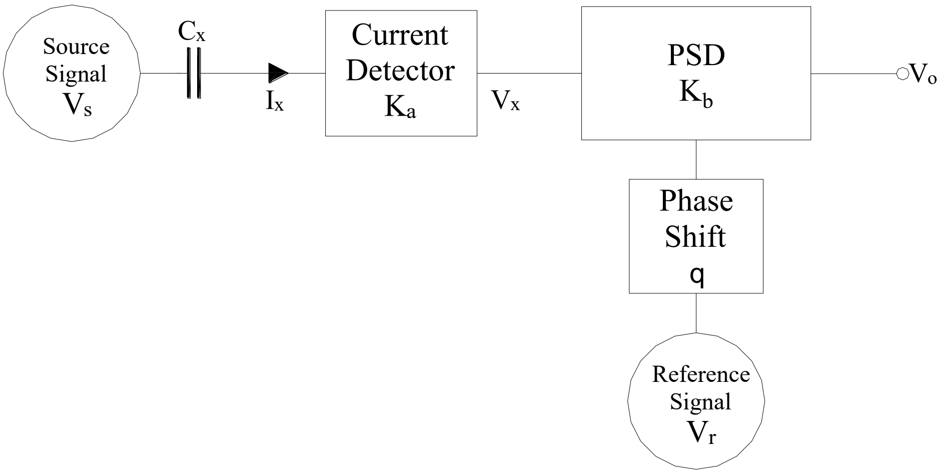

Figure 4.12 AC Based Measuring Circuit

The AC Based Capacitance measuring circuit is shown in Figure 4.12. A sine wave signal source (V_s) is applied to the unknown capacitance (C_x) to produce an AC input current (I_x). The input current is converted into an AC voltage (V_x) via a low impedance input current detector of transimpedance K_a. The AC based measuring circuit has a low baseline voltage drift due to the use of AC amplifiers.

As stated previously electrical capacitance tomography is based on the measurement of permittivity fluctuations caused by the movement of material inside a capacitive sensor. Due to dielectric hysteresis and leakage all dielectrics (except vacuum) have an associated loss conductance which can be modelled by a capacitor (C_x) in parallel with a conductance (G_x) (Figure 4.13a). This implies that the peak voltage output of the current detector (V_x) is the complex sum of voltages V_{Cx} and V_{Gx} which is directly related to the currents passing through C_x and G_x (Figure 4.13b) [45].

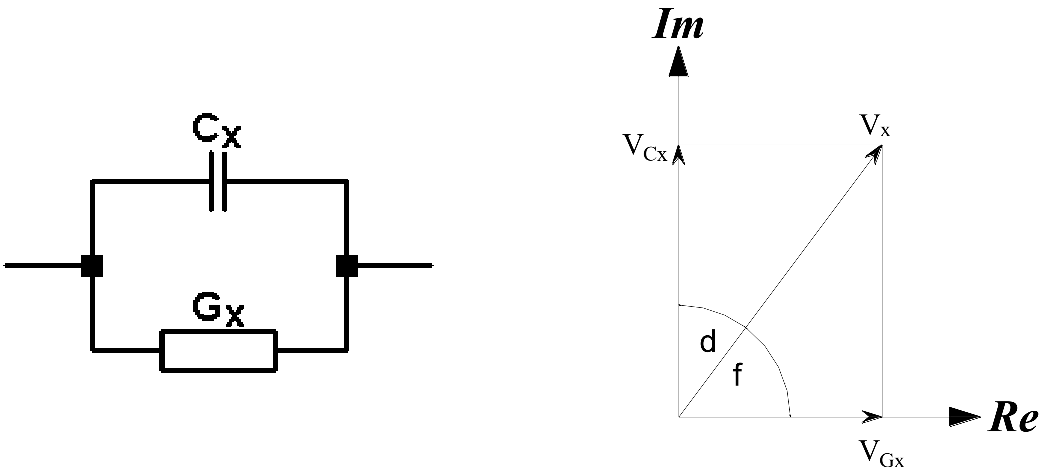

a) Capacitance C_x in parallel with a loss conductance G_x.

b) Complex representation of the current detector output voltage V_x with phase shift ϕ and loss angle δ.

Figure 4.13 Equivalent Circuit of the Capacitive Sensor

Hence:

$$V_x = K_a V_s \left(G_x + j\omega_s C_x \right) \qquad \textbf{Equation 4.12}$$

Where:

V_x is the peak output voltage amplitude from the current detector (V).

V_s is the peak voltage amplitude of the signal source (V).

ω_s is the angular frequency of the signal source $\left(\frac{rad}{s} \right)$.

K_a is the transimpedence of the current detector (Ω).

C_x is the unknown capacitance (F).

G_x is the associated loss conductance (S).

The AC signal V_x is demodulated using a Phase Sensitive Detector (PSD) to produce a DC voltage proportional to the unknown capacitance C_x. The PSD consists of a voltage multiplier followed by a low pass filter (Figure 4.14). The output voltage from the current detector is multiplied by a reference signal which can be either a sine or square wave of the same frequency of the excitation signal. The low pass filter is used to extract only the DC component of the signal product.

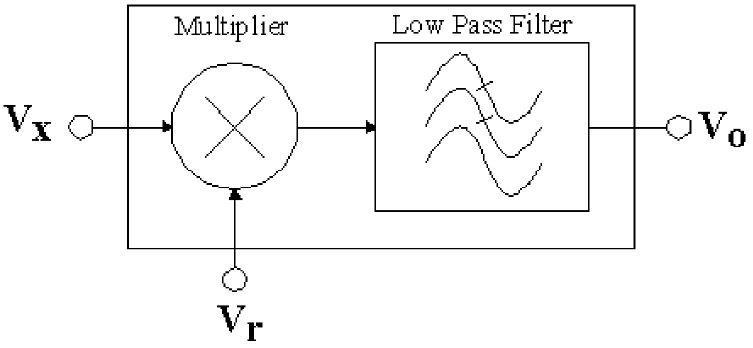

Figure 4.14 The Phase Sensitive Detector (PSD)

The final DC measurement output of the PSD is given by Equation 4.13 [46-48].

$$V_{dc}(\theta) = K_b V_x V_r \cos(\theta - \phi) \qquad \textbf{Equation 4.13}$$

Where:

K_b is the gain factor of the PSD which is dependant upon the scale factor of the voltage multiplier, the type of reference signal used (sine or square), and the band pass gain of the low pass filter.

V_r is the peak voltage amplitude of the reference signal (V)

ϕ is the phase difference between the signal source and current detector output signals.

θ is the phase difference between the current detector output and reference signals.

By trigonometrically expanding Equation 4.13 and substituting $\cos(\phi) = \frac{V_{Gx}}{V_x}$ and $\sin(\phi) = \frac{V_{Cx}}{V_x}$ (from Figure 4.13b) into the result gives;

$$V_{dc}(\theta) = K_b V_r \left[V_{Gx} \cos(\theta) + V_{Cx} \sin(\theta) \right]$$ **Equation 4.14**

As it can be seen from Equation 4.14, by changing the reference signal to be either, in phase with respect to the current detector signal $(\theta = 0°)$ or in quadrature phase with respect to the current detector signal $(\theta = 90°)$, values proportional to G_x or C_x can be extracted separately. This ability to separate the measured capacitance from the loss conductance, gives the AC based circuit a major advantage over the charge/discharge circuit which is affected by loss conductance [43].

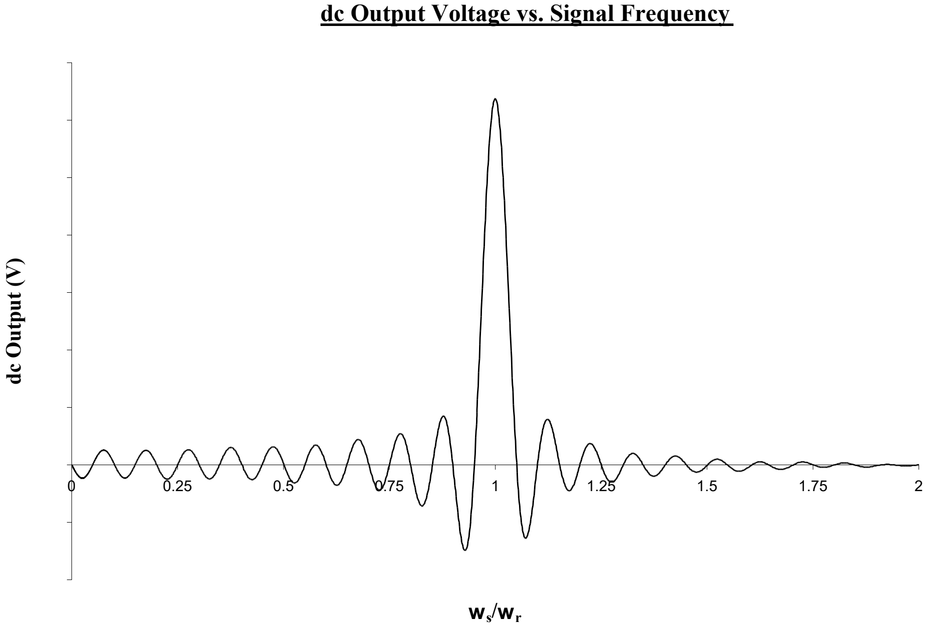

Figure 4.15 Frequency Response of the Phase Sensitive Detector

Figure 4.15 shows the frequency response of the phase sensitive detector, as it can be seen from the figure, the PSD also acts as a high Q band pass filter around the reference frequency ω_r thus giving the AC based circuit a high signal to noise ratio [47].

Compared with the charge/discharge measurement circuit, the AC based circuit will provide an overall superior performance in terms of drift, signal to noise ratio and the capability of measuring either capacitance or conductance. But this configuration is more complicated and costly to implement especially for high frequency operation.

The AC based circuit's overall superior performance over other capacitance measurement circuits plus, the fact that this circuit has been successfully used on previous MMU tomographic imaging system research projects [3, 4], are the primary two reasons why the decision was taken to select this type capacitance measurement circuit for the MMU Virtual Instrument Measuring System's hardware.

Chapter Five

5 MMU Virtual Instrument ECT Imaging System

5.1 Introduction

The development of the MMU Virtual Instrument Electrical Capacitance Tomography system is a continuation of two previous ECT systems, referred to as the PT1, and PT2 systems, developed at the MMU [3, 4] and the investigation into the suitability of LabVIEW as a platform for performing real-time tomographic image reconstruction [8, 49].

The PT1 was an eight electrode; serial capacitance sensing system (applied to a 100mm diameter pipe conveying polypropylene pellets) used primarily for imaging static and real time tomographic images. In order to overcome some of the inherent limitations found with the PT1 system the PT2 system was developed. Besides improvements made to the systems hardware, the core premise of the PT2 system was the modification from serial to parallel capacitance data acquisition which improved the overall data acquisition time (see Chapter 5, Section 5.2.1.2).

The MMU Virtual Instrument Measuring System (VIMS) adopts some of the basic concepts developed for the PT2 system whilst overcoming the operational inflexibility of the PT2 system by replacing most of the strict hardware/software components of the PT2 system with reconfigurable modular software (LabVIEW). It uses a common hardware base (NI PXI embedded controller) which uses proprietary data acquisition hardware (NI PXI data acquisition modules) which can be run independently from the standard PC platform.

This chapter gives an overview of the hardware and software systems employed by the MMU Virtual Instrument Measuring System (VIMS). The chapter begins with an outline view of the construction of the ECT sensor, sensor electrode switching (parallel system signal routing) and the capacitance measurement circuit. The chapter then proceeds with an explanation of how the software system interacts with the hardware, collects the capacitance data and how this data is processed in order to produce an ECT image. The chapter finishes with an introduction to how the Virtual Instrument Measuring System performs dual-plane 8-electrode imaging which is the basis of mass flow measurement by cross-correlation techniques.

5.2 MMU Virtual Instrument Measuring System (VIMS)

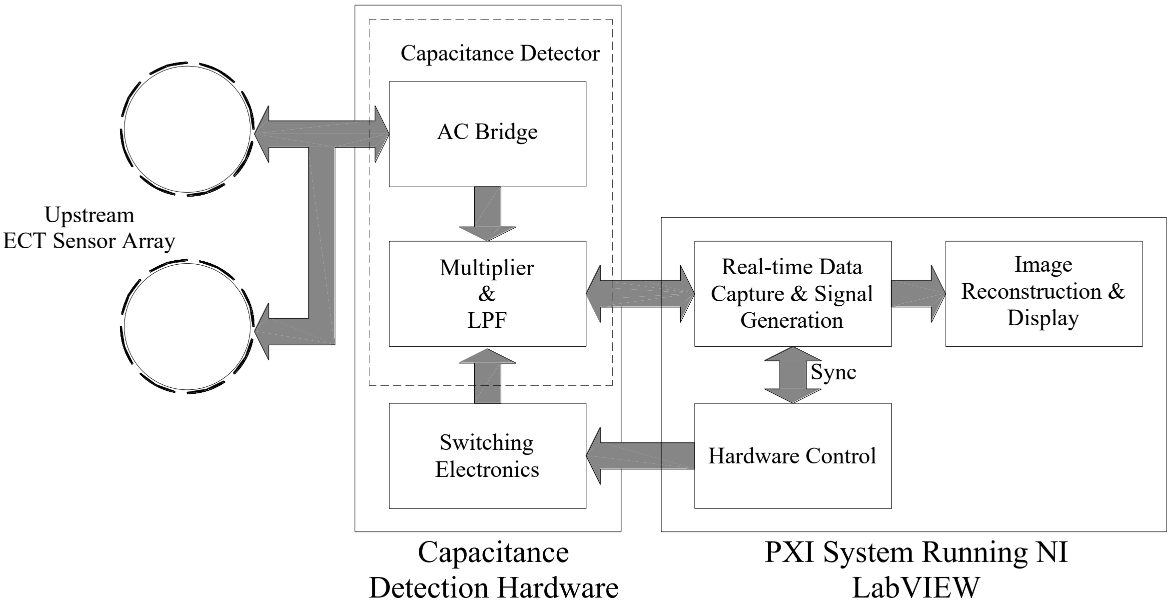

Figure 5.1 VI ECT System Hardware/Software Structure Overview

The key hardware and software components of the MMU Virtual Instrument Measuring System consist of the ECT sensor, capacitance detection hardware and the PXI system (Figure 5.1). The main function of the capacitance detection hardware is to translate the measured capacitance values generated inside the sensor into suitable voltage values that can be read by the PXI analog input hardware. The capacitance detection hardware consists of an AC-bridge detector circuit operating at a frequency of 100 kHz, signal routing hardware and a signal demodulation circuit consisting of a voltage multiplier and low pass filter. An embedded Pentium 4 computer system inside the PXI module implements the Virtual Instrument Software Architecture (VISA) via LabVIEW. The four main sections of the VI software perform, signal generation, data acquisition, hardware control and image reconstruction/display. A more detailed description of the VI ECT System Hardware/Software Structure is given in the following sections.

5.2.1 Imaging Hardware

5.2.1.1 The 8 Electrode Sensor Array

The following section describes the construction of an 8 electrode sensor array; a similar approach was taken for the construction of the 12 and 16 electrode sensor arrays.

Taking into consideration the basic sensor design principles outlined in Chapter 4, Section 4.2.1, the capacitive sensor is constructed from conductive copper tape mounted on a 100mm diameter acrylic pipe to form the external drive/detect and guard electrode arrays.

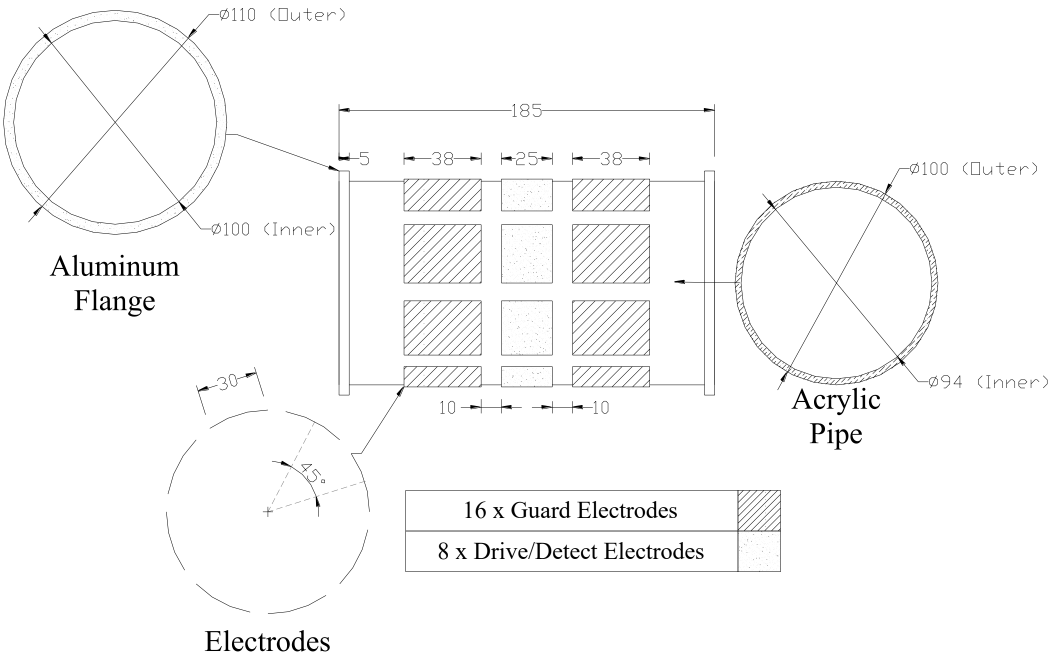

Figure 5.2 Diagram of the 8 Electrode Sensor Array (Dimensions in mm)

Aluminium flanges mounted on either end of the pipe (Figure 5.2) allow the sensor to be readily inserted into the test rig by the use of clamp rings. Electrical connection between the sensor's electrodes and the imaging hardware is achieved via snap-on SMB (**S**ub**M**initure type **B**) connectors which provide quick and easy changes between different sensor configurations.

Figure 5.3 The 8 Electrode Sensor Array with Fitted Outer Shield

Figure 5.3 is a photograph of a complete 8 electrode sensor with fitted outer shield showing the arrangement of the interconnecting SMB connectors and cables.

Figure 5.4 shows the resulting measured inter-electrode capacitances when the 8 electrode sensor was filled consecutively with two permittivity reference materials, in this case the reference materials are air (lower permittivity material ε_L) and polypropylene pellets (higher permittivity material ε_H) [9]. Figure 5.4a shows the resulting measured inter-electrode standing capacitances of the empty (air filled) sensor, whilst Figure 5.4b shows the resulting measured inter-electrode capacitance change (ΔC) of the sensor when filled with polypropylene pellets.

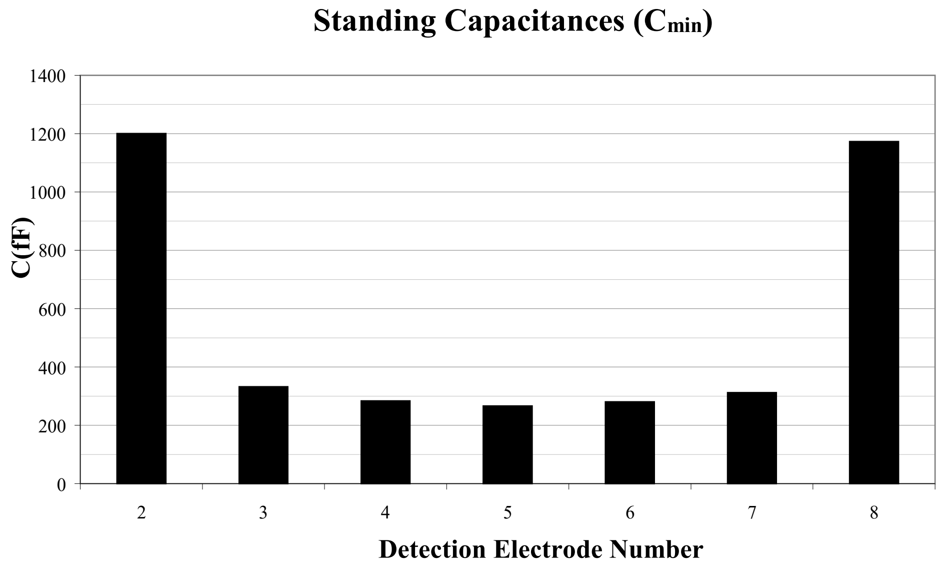

(a)

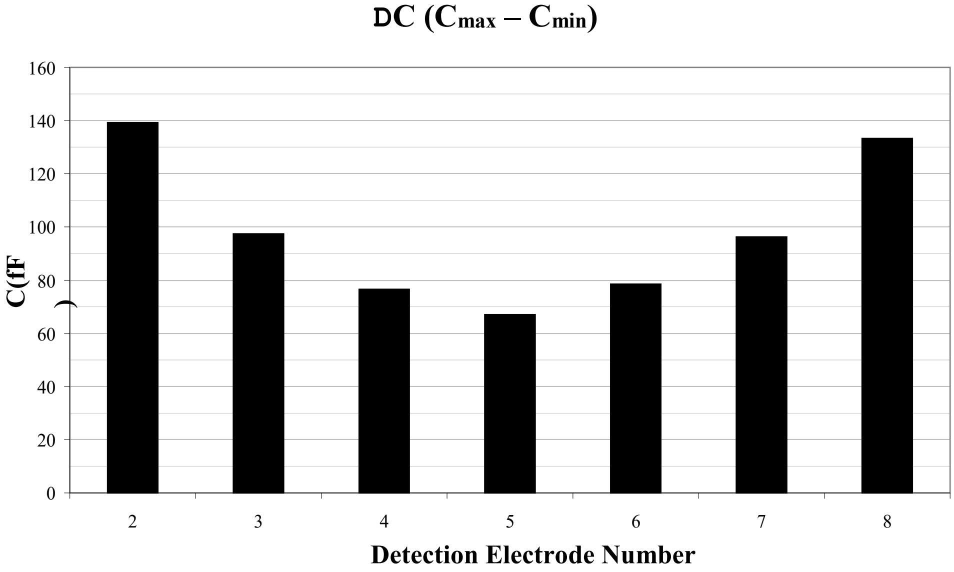

(b)

Figure 5.4 Measured Capacitance for an 8-Electrode ECT Sensor
(a) Standing Capacitances
(b) Changes in Capacitance

It can be clearly seen from Figure 5.4(a), and to a lesser extent Figure 5.4(b), the sensor electrodes (2 and 8) located closest to the excitation electrode (electrode 1) have the highest inter-electrode capacitance values whilst all other drive/detect electrode pairings (1 and 3 through 7) rapidly decrease in capacitance as the distance between the drive/detect sensor pairings increases. Also evident from Figure 5.4 is that the measured standing inter-electrode capacitances of the empty sensor (ranging from 266fF to 1201fF) is significantly larger than the resulting capacitance change (ΔC) when the sensor is filled with polypropylene pellets (ranging from 67fF to 139fF). This implies that any proposed capacitance transducer has to be capable of dealing with a wide range of probable capacitance values as well as detecting relatively small capacitance changes [43]. An appropriate method for counteracting the standing inter-electrode capacitances of the ECT sensor will be examined in Section 5.2.1.3.1.

5.2.1.2 Parallel System Signal Routing

As stated in Chapter 4, Section 4.2, the serial measurement procedure for collecting capacitance information from an 8 electrode ECT sensor requires a total of 28 steps to collect the required 28 electrode pair combinations. An alternative strategy to this would be to energise one electrode whilst simultaneously measuring the capacitance data from the remaining electrodes i.e. the data is collected in parallel.

Measurement Step	**Driven Electrode**	**Detected Electrodes**						
1	1	2	3	4	5	6	7	8
2	2	3	4	5	6	7	8	
3	3	4	5	6	7	8		
4	4	5	6	7	8			
5	5	6	7	8				
6	6	7	8					
7	7	8						

Figure 5.5 Parallel Measurement Strategy Electrode Switching Sequence for an 8 Electrode ECT Sensor

Figure 5.5 shows the succession of measurements made for an 8 electrode ECT sensor during the parallel measurement sequence. As it can be seen from the figure, all 28 electrode pair combinations can be collected in 7 steps as opposed to the 28 steps required for the serial measurement which gives an effective four-fold increase in the total data acquisition time. For an N electrode system, a parallel data collection strategy will result in a $\frac{N}{2}$ fold improvement in overall data acquisition time.

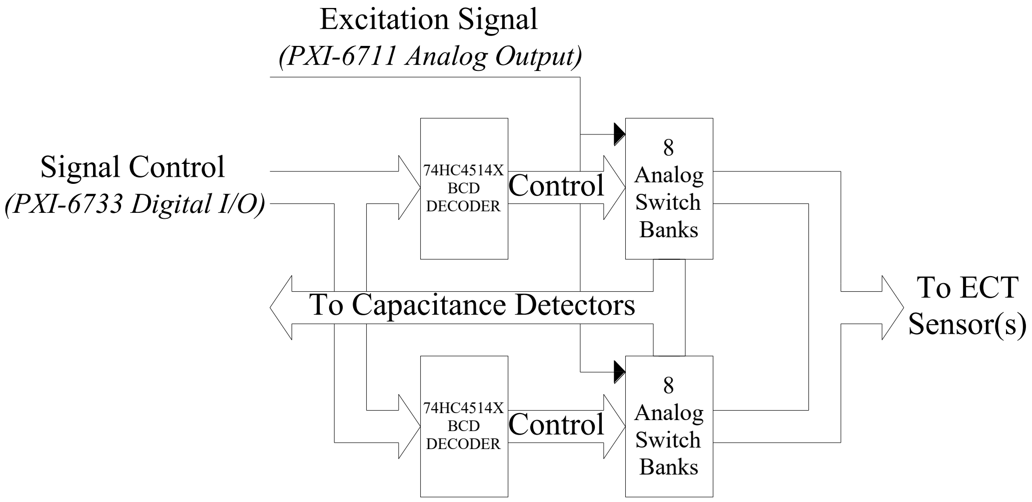

Figure 5.6 Parallel Switching Electronics Functional Diagram

Figure 5.6 shows the block diagram of the parallel switching circuit. Eight digital control lines from the PXI-6733 digital I/O module are used to control the individual state of sixteen analog switch banks via two 74HC4514 BCD decoders. Each switch bank controls which electrode inside the ECT sensor is driving or detecting whilst maintaining the field on the axial guard electrodes (see Chapter 4, Section 4.2.1).

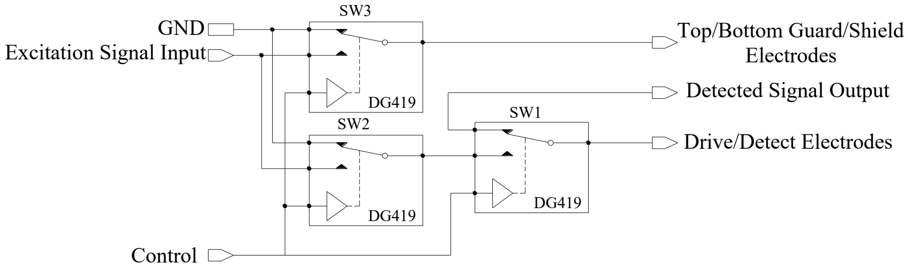

Figure 5.7 Circuit Configuration of DG419 CMOS SPDT Switches

A single switch bank consists of three DG419 single-pole/double-throw (SPDT) switches connected to single control line which operates each switch simultaneously (Figure 5.7).

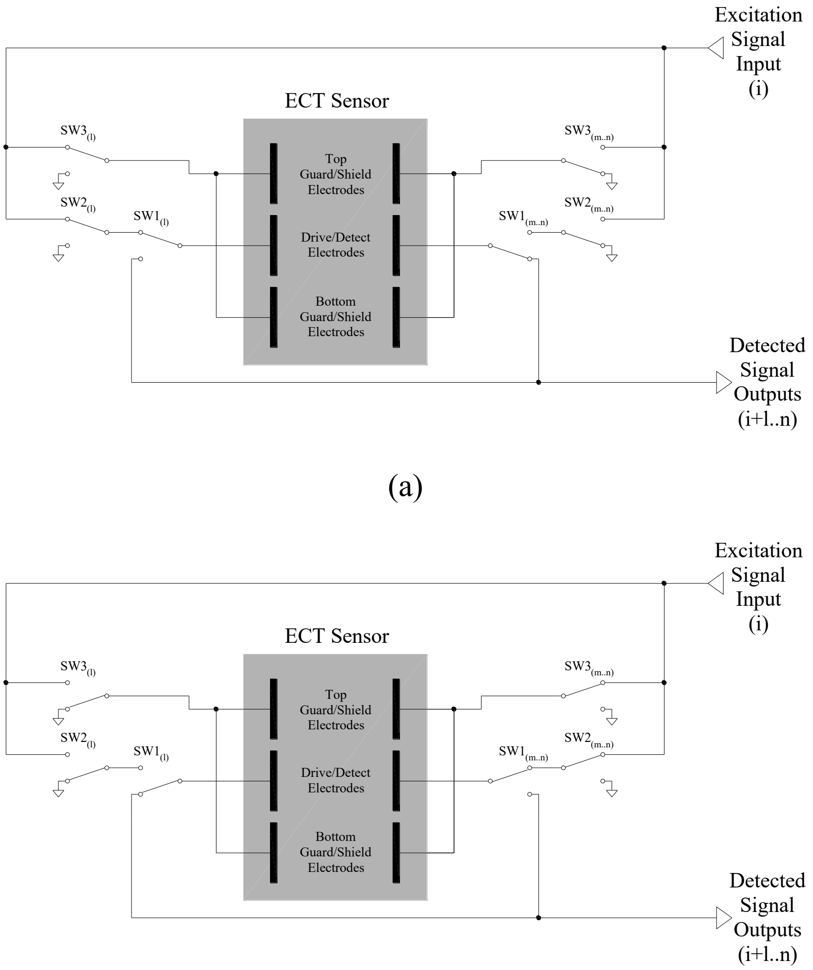

(a)

(b)

Figure 5.8 Electrode Switch Arrangement

Figure 5.8(a) and Figure 5.8(b) show the operation of the switch bank arrangement connected to each individual sensor. Figure 5.8(a) shows how the electrodes on the left hand side are switched to drive mode, whilst the right hand side of the diagram represents all the remaining electrodes within the ECT sensor which are switched to detect mode. Conversely Figure 5.8(b) shows how the electrodes on the left hand side of the diagram switched to detect mode, whilst the right hand side of the diagram shows how any of the remaining electrodes would be switched into drive mode.

5.2.1.3 Capacitance Measurement

For an ECT parallel measurement system with a 16 electrode sensor array capability, fifteen individual measurement circuits would be required for data acquisition. The capacitance sensor for the MMU VI ECT system is based around the measurement circuit developed for the PT2 system [4], which is the AC based capacitance measuring circuit as summarised in Chapter 4, Section 4.2.3.3.

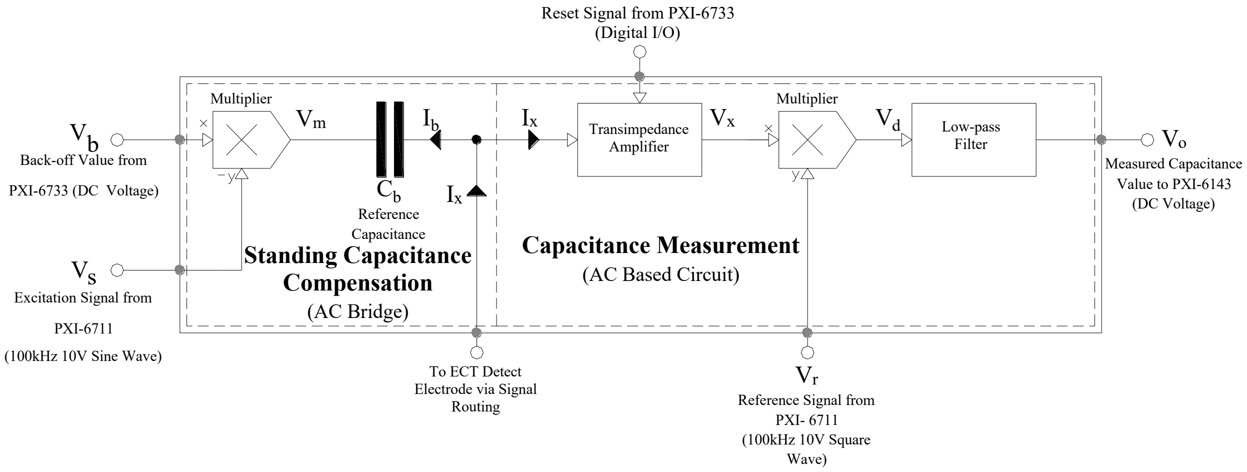

Figure 5.9 Block Diagram of the Capacitance Measurement Circuit

A block diagram of one of the fifteen capacitance measurement circuits is shown in Figure 5.9. The capacitance measurement circuit can be divided into two main sections, the standing capacitance compensation circuit, and the capacitance measurement circuit. The operation of each of these two sections is described below.

5.2.1.3.1 Standing Capacitance Compensation

The AC based capacitance measuring circuit, measures the absolute value of the unknown capacitance. However, as stated in Section 5.2.1.1, the introduction of higher permittivity materials into the sensing area results in small changes of capacitance in contrast to the relatively large standing capacitances of the empty sensor. Maximum sensitivity of the AC based capacitance measuring circuit to small capacitance changes is achieved by adding a preceding stage to the capacitance measurement circuit. This stage is will remove the signal contribution of the standing capacitances leaving only a signal which is proportional to the change in capacitance (ΔC_x). This is achieved by the use of an AC bridge circuit (Figure 5.10) which cancels out the standing capacitances of the sensor by applying a ‘back-off’ signal (V_m) in anti-phase to the excitation waveform (V_s) via a fixed capacitance (C_{b1} and C_{b2}).

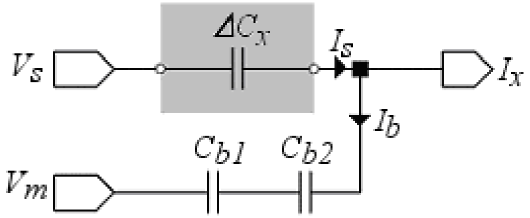

Figure 5.10 AC Bridge Circuit

During low permittivity calibration of the ECT sensor, the amplitude of the anti-phase signal V_m applied to AC bridge circuit is adjusted until the bridge is balanced ($I_s = I_b$) and a zero voltage reading will be detected at the capacitance measurement circuit's output (V_o in Figure 5.9). By compensating for the standing capacitance in this way, the AC based measuring circuit will only give a voltage reading proportional to the change in capacitance ΔC_x caused permittivity changes inside the sensor.

The necessary anti-phase signal V_m, is derived from the 100 kHz sine wave reference signal V_s (generated by the PXI-6711 analog output card) which is inverted then scaled by a fixed DC value V_b (generated by the PXI 6733), by means of a Burr Brown MPY634 precision wide-bandwidth multiplier.

It can be shown that the peak amplitude of the required back-off signal is proportional to the peak amplitude of the reference signal and the ratio of the measured capacitance to the fixed reference capacitance [43] this is given by Equation 5.1.

$$V_m = -V_s \frac{C_x}{C_b}$$ **Equation 5.1**

Where:

V_s is the peak amplitude of the excitation signal (V).

V_m is the peak amplitude of the compensation signal (V).

C_x is the unknown capacitance (F).

C_b is the reference capacitance, $C_{b1} + C_{b2}$ (F).

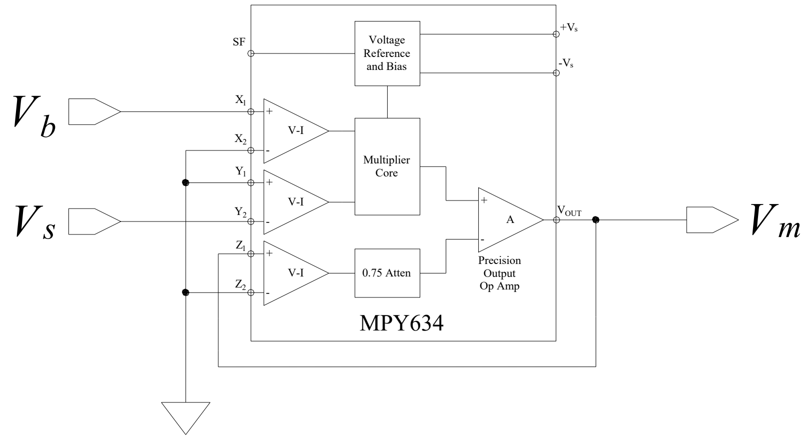

Note: *Connections* V_s *and* V_m *matches the same named connections as shown in Figure 5.10.*

Figure 5.11 The Burr Brown MPY634 Precision Wide-Bandwidth Multiplier as used in the Parallel System Standing Capacitance Compensation Circuit

Figure 5.11 shows the circuit configuration of the MPY634 multiplier as used in the standing capacitance compensation circuit which has a transfer function of;

$$V_m = -\frac{V_s\ V_b}{10} \qquad \textbf{Equation 5.2}$$

By combining Equations 5.1 and 5.2 a theoretical value for V_b can be established;

$$V_b = \frac{C_x}{C_b}10 \qquad \textbf{Equation 5.3}$$

The actual required value for V_b is determined in-situ by the imaging software during the system calibration phase (see Section 5.2.2.1.1 below).

5.2.1.3.2 Capacitance Measurement Circuit

The capacitance measurement circuit consists of a transimpedance amplifier followed by a phase sensitive demodulator as depicted in Figure 5.9.

The transimpedance amplifier shown in Figure 5.12 uses two wide bandwidth Burr Brown OPA627AP operational amplifiers. The first stage acts as a current to voltage converter (U1). For improved circuit sensitivity, the current to voltage converter stage is followed by a non-inverting buffer amplifier stage (U2) [9]. Lf is incorporated into the feedback path of the current to voltage converter in order to minimise the affects of mutual capacitance between adjacent electrodes of the ECT sensor array [50]. Also included in the feedback path is a DG481 analog CMOS switch S1 which is controlled by the PXI-6733 input/output module. S1 resets the capacitance detector amplifier prior to capacitance measurement in order to prevent amplifier stage saturation.

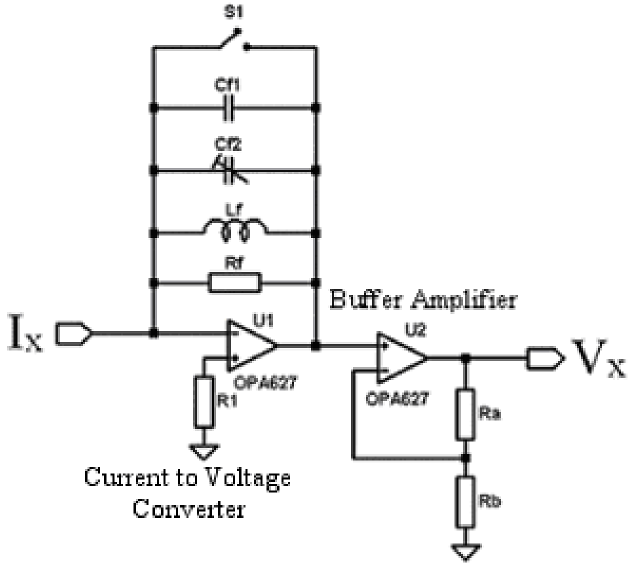

Figure 5.12 Schematic Diagram of the Capacitance Measurement Stage

The capacitance and inductance present in the feedback path of the current to voltage converter will cause the capacitance measurement circuit to act as a second order band pass filter with the transfer function $H(s)$ of the circuit as given by Equation 5.4 [51];

$$H(s) = \frac{v_x(s)}{i_x(s)} = H_0 \frac{s\frac{\omega_p}{Q_p}}{s^2 + s\frac{\omega_p}{Q_p} + \omega_p^2}$$ **Equation 5.4**

Where:

H_0 is the mid band transimpedance gain of the circuit which is given by $H_0 = -R_f\left(1 + \frac{R_a}{R_b}\right)$.

ω_p is the pass band frequency which is given by $\omega_p = \frac{1}{\sqrt{Lf\,Cf}}$.

Q_p is the quality factor of band pass filter which is given by $Q_p = \sqrt{\frac{Cf}{Lf}} Rf$.

Cf is the parallel combination of $Cf1$ and $Cf2$ where, $Cf2$ is adjusted to give maximum output at 100kHz.

The bandwidth of the circuit can be determined from Equation 5.5.

$$\omega_{BW} = \frac{\omega_p}{Q_p} = \frac{1}{R_f C_f}$$

Equation 5.5

The frequency response of the current to voltage converter circuit is at a maximum when the input frequency is at 100 kHz and the transimpedance R_t of the current to voltage converter is equal to the circuit's feedback resistance R_f, i.e. at 100 kHz the total gain of the capacitance measurement stage is equal to its mid band gain H_0.

In the MMU Virtual Instrument Electrical Capacitance Tomography system, the capacitance measurement stage is designed to have a mid band transimpedance in the region of 22 MΩ which gives this circuit a sensitivity of approximately 100 Volts/pF.

The phase sensitive detector extracts the imaginary (capacitance) DC voltage component from the voltage waveform at the output of the capacitance measurement circuit V_x (see Chapter 4, Section 4.2.3.3) and produces an output voltage V_o which is directly proportional to the measured capacitance.

The first stage of the phase sensitive detector uses a Burr Brown MPY634 (Figure 5.13) which multiplies V_x by a 100 kHz square wave V_r (generated by the PXI-6711 input/output module and phase locked to the excitation signal V_s).

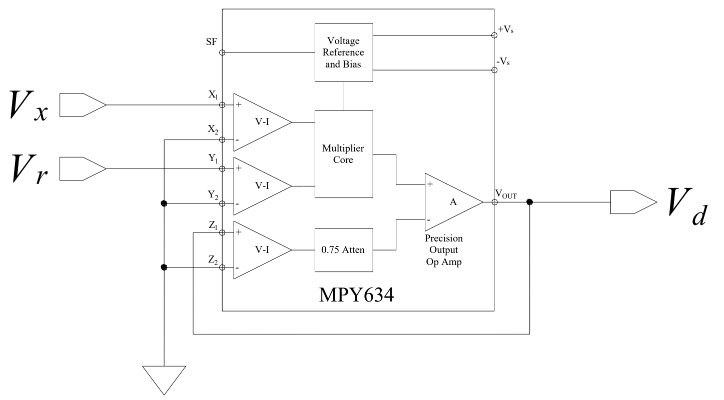

Figure 5.13 The Burr Brown MPY634 Precision Wide-Bandwidth Multiplier as used in the Signal Multiplier Stage of the Phase Sensitive Detector

When V_x and V_r are in phase, the resultant signal from the voltage multiplier (V_d) will contain both a sine-wave component and a DC component as shown in Equation 5.6.

$$V_d = V_x V_r \frac{K}{SF}\left(1+\cos\left(2\omega_r\right)\right) \qquad \textbf{Equation 5.6}$$

Where:

V_x is the peak amplitude of the signal acquired from the capacitance measurement stage.

V_r is the peak amplitude of the reference signal.

SF is the scaling factor of the multiplier (10 for a MPY634)

ω_r is the frequency of the excitation signal.

K is a constant dependant upon the waveform of the reference signal used (see Chapter 4, Section 4.2.3.3). Where $K = \frac{1}{2}$ or $K = \frac{\pi}{2}$ for a corresponding sine-wave or square-wave reference signal.

As the DC component contains the capacitance information required, the sine-wave component of the signal is removed by passing it through a low-pass filter (LPF) network. The MMU Virtual Instrument ECT Imaging System consists of two cascaded second order unity gain Sallen Key low pass filters as shown in Figure 5.14.

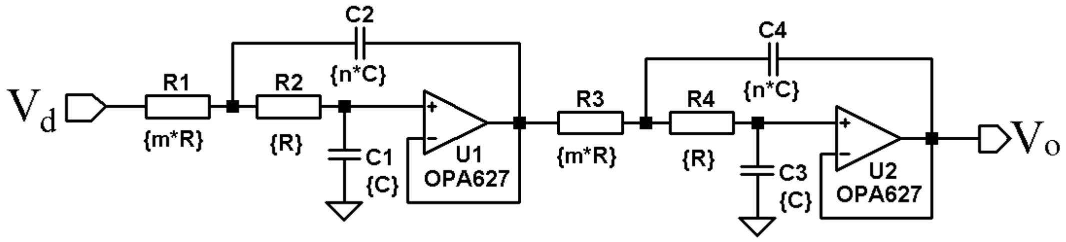

Figure 5.14 PSD Low-Pass Filter Stage

Design of the LPF is a trade-off between the cut-off frequency ω_c, and the filter's settling time τ_s. If the cut-off frequency is too high, some of the AC component of the signal from the transimpedance amplifier will be allowed to pass through which will adversely affect the capacitance measurement circuit's signal to noise performance. If the cut-off frequency is too low, the filter's settling time will increase thus slowing down the ECT system's overall capture rate.

Previous work in this area [45, 52], has produced a LPF design guideline which gives a method for calculating a suitable value for the filter's highest cut-off frequency (ω_c) by using Equation 5.7.

$$\omega_c \le \left[\frac{(2\omega_r)^{2n}}{\left(\frac{V_x V_r}{V_{LSB}} \frac{K}{SF} \right)^2 - 1} \right]^{\frac{1}{2n}}$$

Equation 5.7

Where:

V_x is the maximum peak amplitude of the signal acquired from the capacitance measurement stage.

V_r is the maximum peak amplitude of the reference signal.

V_{LSB} is the voltage magnitude of the ADC's LSB (see Equation 5.8).

n is the filter's order.

SF is the scaling factor of the multiplier.

ω_r is the frequency of the excitation signal.

K is a constant dependant upon the waveform of the reference signal used ($K = \frac{1}{2}$ sine-wave, $K = \frac{\pi}{2}$ square-wave).

The value of V_{LSB} is calculated from Equation 5.8.

$$V_{LSB} = \frac{V_{\max} - V_{\min}}{2^N}$$ **Equation 5.8**

Where:

$V_{\max}$ is the maximum input voltage to the ADC.

$V_{\min}$ is the minimum input voltage to the ADC.

N is the bit resolution of the ADC.

Equation 5.7 gives a maximum cut off frequency for the MMU ECT system's LPF of $\omega_c \leq 8.358kHz$. Once a suitable cut-off frequency is determined, the required R and C component values of the filter can be obtained. Referring to Figure 5.14, by letting $m = 1$ and $n = 2$ (in this case), the required R and C component values can be found by using Equation 5.9 [51].

$$\omega_c = \frac{1}{\sqrt{mn}RC}$$ **Equation 5.9**

The final design for the MMU ECT system's LPF was simulated in PSPICE (see Appendix A) and the results of the LPF's frequency and transient responses showed that the LPF had a cut-off frequency of $6kHz$, an attenuation gain of $-105dB$ and, a settling time of $300\mu s$.

Figure 5.15 shows internal and external photographs of the final version of the MMU ECT system's capacitance detection hardware. The internal view Figure 5.15(a) shows the position of the electrode sensor switching electronics, the PXI interface board and, the fifteen capacitance measurement circuits. The front view Figure 5.15(b) shows the thirty-two SMB ECT sensor connectors. The sixteen connectors on the top row connect to the drive/detect electrodes. The sixteen connectors on the bottom row connect to the ground/shield electrodes.

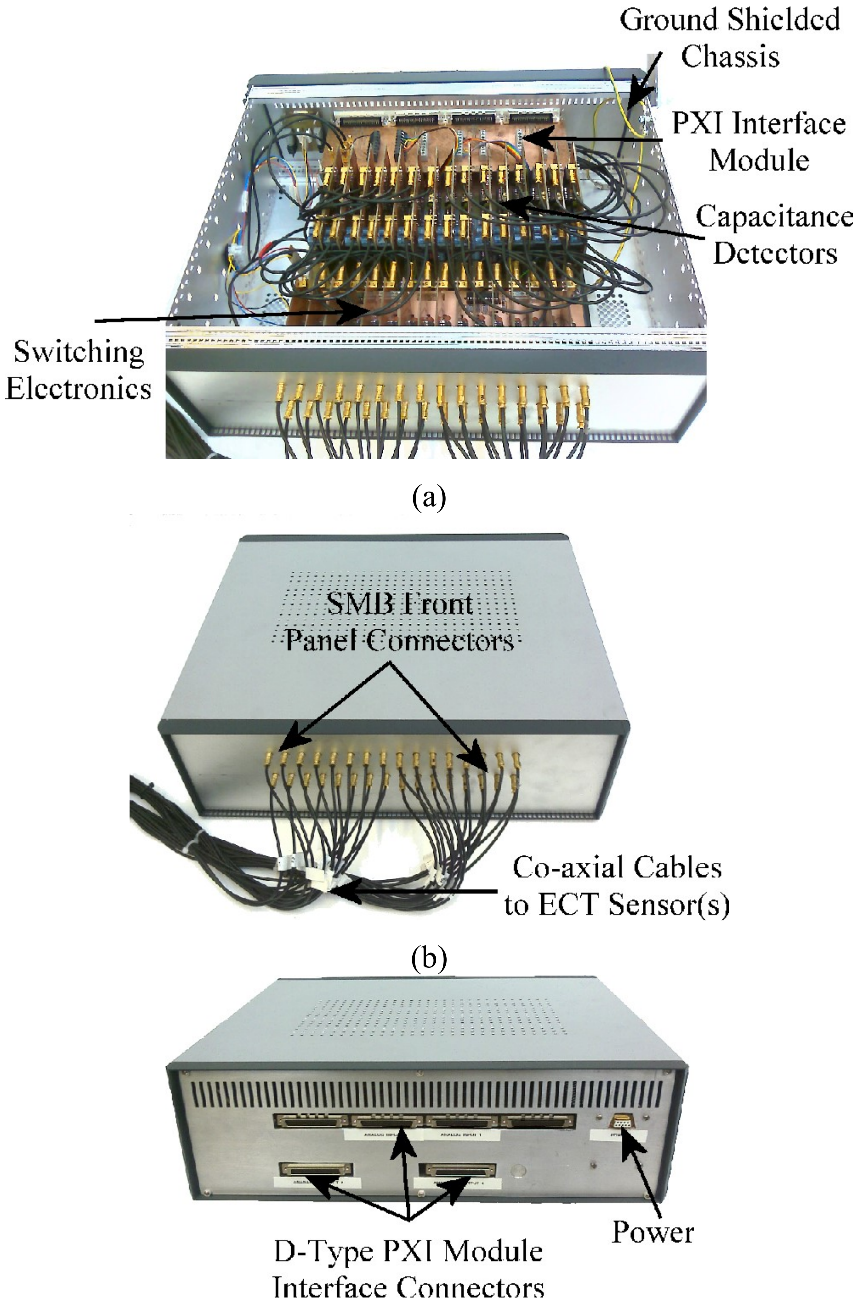

(a)

(b)

(c)

Figure 5.15 The Final Version of the MMU ECT Capacitance Detection Hardware

The rear view Figure 5.15(c) shows the power input connector and the interface connectors to National Instruments PXI data acquisition system.

5.2.2 Imaging Software

The overall image generation process can be broken down into two distinct and separate procedures:

1. System calibration.
2. Capacitance data acquisition and image reconstruction.

This division is reflected in the software design for the parallel ECT imaging system, where the software consists of two separate LabVIEW virtual instrument applications, one application for system calibration and a separate application for data acquisition and permittivity image generation. The advantage of this approach is the reduction of overall memory usage. Once the system is calibrated there is no need for the calibration software to remain in memory and can be removed from the memory pool before the image generation application is loaded and executed.

5.2.2.1 The System Calibration Application

(a) (b)

Figure 5.16 (a) The System Calibration VI's Front Panel and, (b) the SubVIs called by the System Calibration VI

The front panel for the system calibration VI is shown in Figure 5.16a. This VI is used during the system calibration phase, to generate standing capacitance compensation (back-off) voltage values and determine the required normalisation values associated with C_{max} and C_{min}. All values created by this VI are recorded as a text file for later use by the image reconstruction software VI. Depending upon its current mode of operation (i.e. which button is pressed), the System Calibration VI invokes either one of two subVIs (see

Figure 5.16b), "boff finder.vi" (back-off finder) or, "cmax cmin.vi" (determine normalisation values).

5.2.2.1.1 Back-off Voltage Finder

When the "find backoffs" button is pressed on system calibration VI's front panel (see Figure 5.16a), the main VI calls the back-off finder subVI "boff finder.vi". The back-off finder operates by applying the excitation signal to one electrode whilst simultaneously applying DC back-off multiplier voltages to the remaining capacitance measurement circuits. The value of the multiplier is increased until the resultant DC value (V_o) from all the capacitance measurement circuits is less than 1mV. The process is repeated until all the DC back-off values for all electrode pair combinations (M) have been found. The generated data is then written to a file for later use.

Figure 5.17 shows part of a sequence of DC back-off voltage values for an 8 electrode sensor generated by the back-off finder. Here, electrode 1 is the excitation electrode and back-off values have been determined for electrode 2 through to electrode 8.

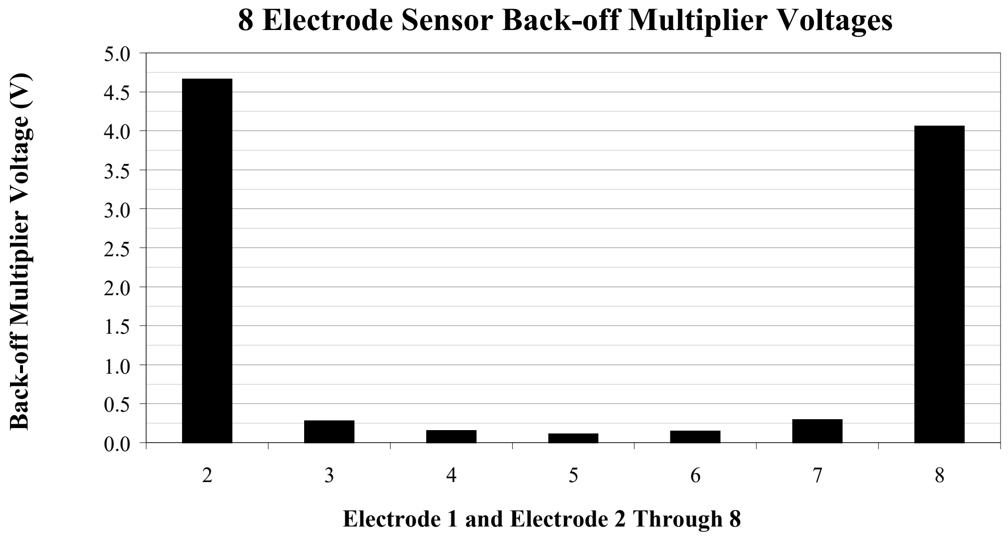

Figure 5.17 Typical DC Back-off Voltage Values for an 8 Electrode Sensor

As it can be seen from Figure 5.17, sensor electrodes (2 and 8) located closest to the excitation electrode (electrode 1) have the highest inter-electrode capacitance values (see Section 5.2.1.1) and therefore require the highest back-off multiplier values.

5.2.2.1.2 Normalisation Voltage Finder

The required normalisation values associated with $C_{\max}$ and $C_{\min}$ are determined by filling the ECT sensor with the lower permittivity material to be imaged and the "Write Cmin" button is pressed on system calibration VI's front panel (Figure 5.16a). This activates the "cmax cmin.vi" subVI which determines the electrode permutation values of $C_{\min}$, the subVI then saves these values to the calibration file. The above process is then repeated with the ECT sensor filled with the higher permittivity material to be imaged. The "Write Cmax" button is then pressed on system calibration VI's front panel, which calls the "cmax cmin.vi" subVI to find and save to the calibration file, the electrode permutation values of $C_{\max}$.

5.2.2.2 Real Time Data Capture and Image Reconstruction

Figure 5.1 shows how the virtual instrument software architecture of the parallel VI ECT imaging system is broken down into four discrete sub-systems;

1. Real-time data capture. Capacitance data is collected via the PXI-6143 multifunction data acquisition cards.
2. ECT hardware control. ECT sensor signal routing and electrode coupling is controlled via the PXI-6733 high-speed analog/digital output cards.
3. Signal Generation. Excitation, reference and, DC back-off signals are generated via the PXI-6711 and PXI-6733 high-speed analog/digital output cards.
4. Image reconstruction. The computer uses the collected capacitance data to generate permittivity image data prior to display.

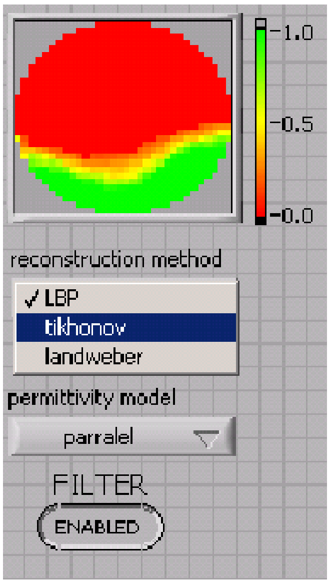

Figure 5.18 Parallel Imaging System Front Panel

The front panel of the parallel imaging system main VI is shown in Figure 5.18. This panel displays the reconstructed permittivity image and allows the user to control which reconstruction method and permittivity model is to be employed during the image reconstruction process.

Figure 5.19 shows the primary sequence of subVI's called by the parallel ECT system's main VI.

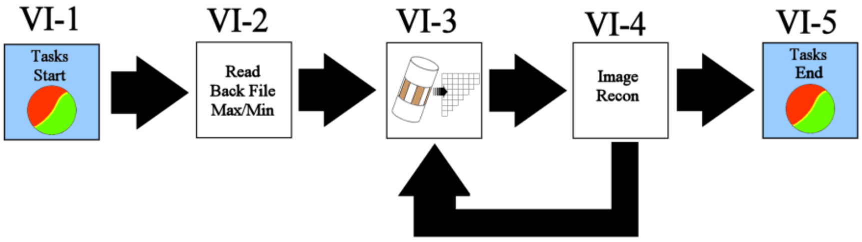

Figure 5.19 The Sequence of SubVI's Involved in the Generation of Permittivity Images

The primary sequence is executed in the following order;

VI-1. Set up the PXI modules (initiate data acquisition) and ECT hardware ready for use.

VI-2. Read-in previously created calibration data (see Section 5.2.2.1).

VI-3. Collect capacitance data from the ECT hardware.

VI-4. Using the calibration and capacitance information, reconstruct and then display a permittivity image. If an exit condition exists, go to VI-5. If not, go to VI-3 and repeat process.

VI-5. End data acquisition, save data, then exit.

5.2.2.2.1 Collect Capacitance Data from the ECT Hardware

The collect capacitance data subVI (VI-3 in Figure 5.19), outputs generated excitation, reference and digital control signals to the ECT hardware and then acquires the measured capacitance data. The output from this VI is a vector - whose number of elements is dependant upon the number of electrodes within the ECT sensor itself (28 values for an 8 electrode sensor) - containing a series of voltage values corresponding to the normalised capacitance C_N measured inside the sensor for all possible electrode pair combinations (see Chapter 4, Section 4.2.2.1).

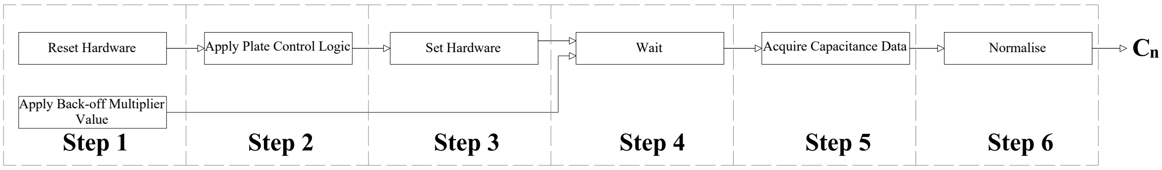

Figure 5.20 Collect Capacitance Data SubVI Flow Diagram

A flow diagram illustrating the main functions of the collect capacitance data subVI is shown in Figure 5.20. Besides the collection of capacitance data, the key function of this VI is to ensure that correct synchronisation exists between the various signals sent to the ECT measurement system and the timing of the data read from the ECT system.

5.2.2.2.2 Image Reconstruction

The image reconstruction subVI (VI-4 in Figure 5.19), uses the normalised capacitance data acquired by the collect capacitance data subVI and with the use of a suitable sensitivity map produces a N by N pixel image grid.

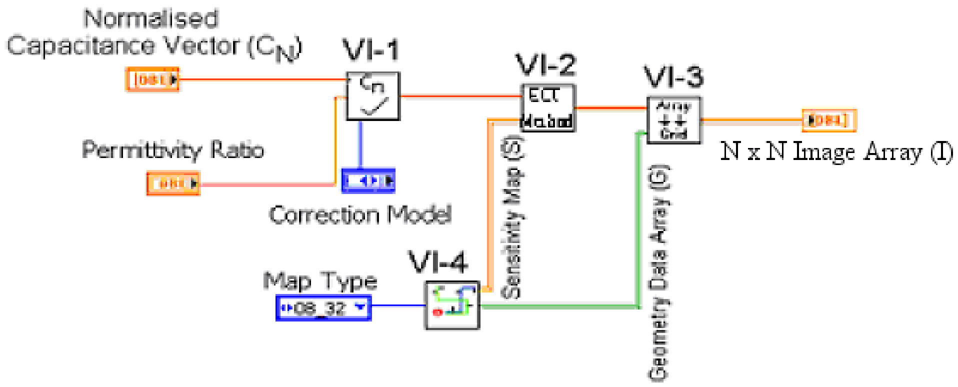

Figure 5.21 Simplified Version of the Image Reconstruction SubVI

A Simplified Version of the Image Reconstruction subVI is shown in Figure 5.21. A correction subVI (labelled VI-1 in Figure 5.21) allows the user to optionally select which permittivity model is used (parallel, series, or Maxwell) to correct the normalised capacitance data (C_N) before actual image reconstruction commences (see Chapter 4, Section 4.2.2.1). The ECT method subVI (labelled VI-2 in) uses a sensitivity map (produced by VI-4 in Figure 5.21) to convert the normalised capacitance data into a vector containing the grey level values of the ECT image. The ECT Method subVI (Figure 5.22) achieves this by one of three user selectable image reconstruction methods, Linear Back Projection (see Chapter 4, Section 4.2.2.2), the Tikhonov transform or, the Landweber transform [9].

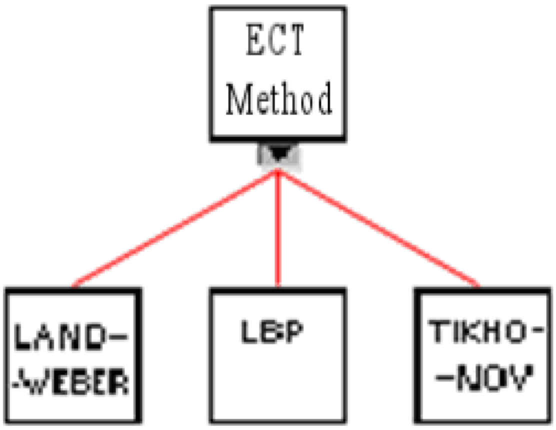

Figure 5.22 Hierarchal Diagram of the ECT Method SubVI

Finally, the ECT image vector is passed to the array to grid subVI (labelled VI-3 in Figure 5.21). This subVI uses a Boolean valued, vessel geometry data map (produced by VI-4 in Figure 5.21); the vessel geometry data map contains information about valid pixel locations within the vessel's boundary. This information is used in order to map the grey level values onto an N x N pixel image thus converting the grey level image vector into a format that can easily be displayed as an ECT image.

5.2.2.3 Dual-Plane 8-Electrode Imaging

The MMU Virtual Instrument ECT Imaging System's hardware has incorporated dual-plane tomographic imaging capability where two separate 8 electrode sensors spaced axially apart further increases the potential use of the system for process modelling and flow control. The LabVIEW virtual instrument software achieves this by running two corresponding synchronised versions of the real time data capture and image reconstruction VI (described in Section 5.2.2.2) as a single VI as shown in Figure 5.23b.

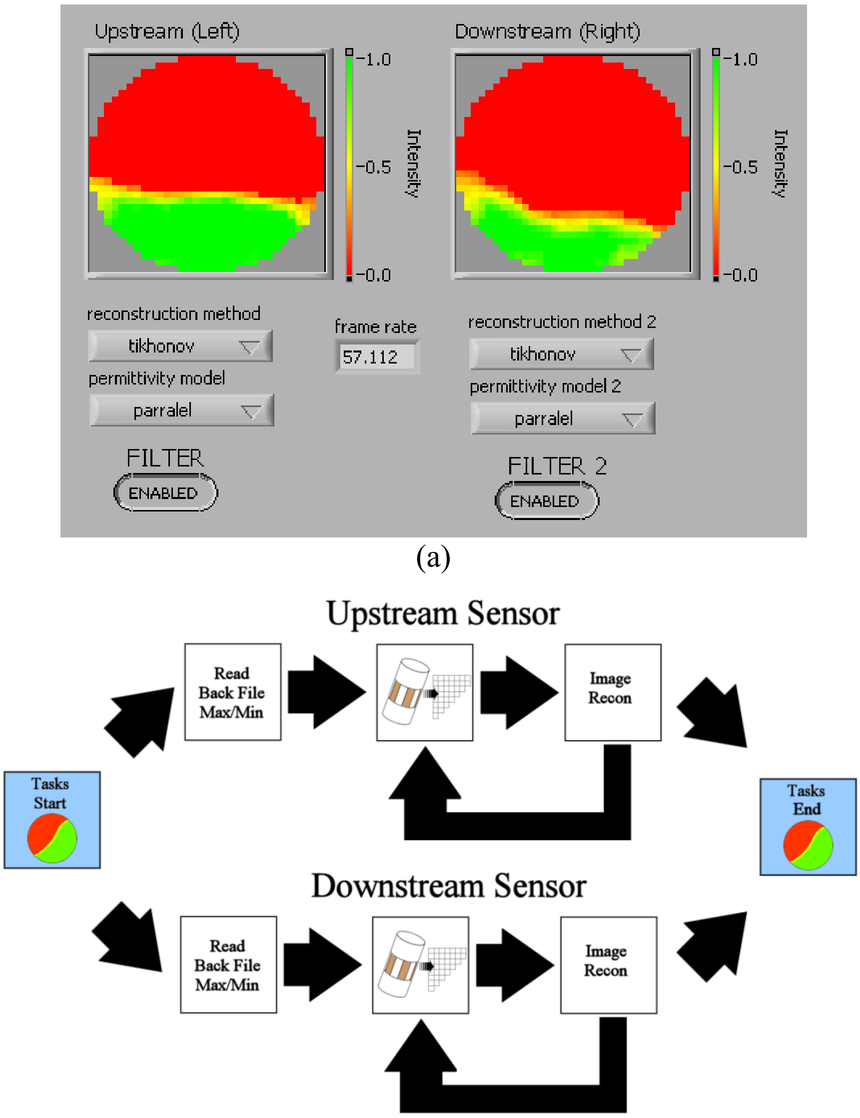

reconstruction method: tikhonov

permittivity model: parralel

frame rate: 57.112

reconstruction method 2: tikhonov

permittivity model 2: parralel

FILTER: ENABLED

FILTER 2: ENABLED

(a)

(b)

Figure 5.23 (a) The Dual-Plane 8-Electrode Imaging System Front Panel and, (b) the Dual-Plane 8-Electrode Imaging VI Parallel Sequence Structure

5.3 Conclusion

A virtual instrument ECT measuring system has been developed which is capable of taking real time cross-sectional tomographic images of the flow of polypropylene pellets as they pass through a 94mm diameter ECT sensor array. The virtual instrument ECT measuring system consists of three main key hardware and software components;

- The ECT sensor array.
- The Capacitance detection hardware.
- The PXI system running NI LabVIEW.

Together the above components form the foundation for a highly flexible ECT system with the following advantages over previous MMU ECT measurement systems;

- Parallel capacitance data acquisition: All combinations of inter-electrode capacitances can be measured simultaneously giving a four fold increase in data capture rate. Leading to real time data capture and image reconstruction.
- Optional ECT sensor configurations: ECT images can be produced from single 8, 12 or 16 electrode ECT sensors or from dual 8 electrode ECT sensors.
- Improved image accuracy: Through the use of the iterative LBP algorithms and Tikhonov and Landweber transforms for image reconstruction.
- System flexibility: The highly modular nature of the LabVIEW programming environment allows the system to be tailored to meet specific system requirements.

Chapter Six

6 Development of a LabVIEW Virtual Instrument Cross Correlation Flowmeter

6.1 Introduction

This chapter explains how the MMU Virtual Instrument Measuring System (VIMS) was extended to provide flow velocity information via cross correlation and solids mass flow from ECT images.

The chapter starts by looking at the discrete cross correlation function and how the accuracy of this function is affected by sampling over finite time periods. The chapter then proceeds by looking at how the accuracy of flow measurement is affect by statistical errors and velocity discrimination. The chapter then introduces some of the computational methods used for obtaining discrete forms of the cross correlation function. The chapter then finishes with how LabVIEW was utilised in the measurement of solids mass flow.

6.2 Cross Correlation of Sampled Signals

6.2.1 The Discrete Cross Correlation Function

As introduced in Chapter 3, Section 3.3, the measure of similarity between two random stationary (ergodic), processes or signals $x(t)$ and $y(t)$ as a function of a time-lag (τ), can be expressed by the Cross Correlation Function (CCF) $R_{xy}(\tau)$ (Equation 6.1).

$$R_{xy}(\tau) = \lim_{T \to \infty} \frac{1}{T} \int_0^T x(t) y(t + \tau) dt$$ **Equation 6.1**

If a strong correlation exists between the reference (upstream) signal $x(t)$ and the tracer (downstream) signal $y(t)$, a well-defined peak will manifest itself $\hat{R}_{xy}(\tau)$, corresponding to the transit time delay (τ_d) between the two signals (Figure 6.1).

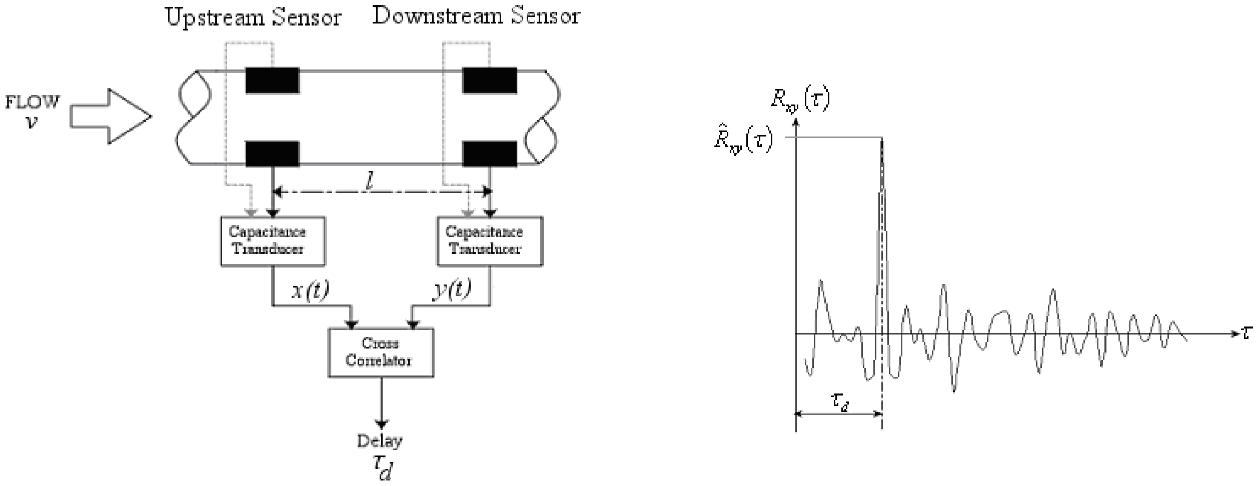

Figure 6.1 Cross Correlation of the Upstream and Downstream Sensor Signals

Equation 6.1 assumes that the correlation process is calculated over an infinite time period ($T \to \infty$), whereas in practical situations, calculations are made over a finite time period this means that the measured CCF is only an approximation to the true CCF i.e.

$$R_{xy}(\tau) \approx \frac{1}{T}\int_0^T x(t)y(t+\tau)dt \qquad \textbf{Equation 6.2}$$

Due to statistical uncertainties, this approximation will introduce a scattering on the measured transit time. For time sampled data sets, the discrete form of Equation 6.2 becomes;

$$R_{xy}(m) = \frac{1}{N}\sum_{n=0}^{N-1} x(n)y(n+m) \qquad \textbf{Equation 6.3}$$

Where $x(n)$and $y(n)$ are the upstream and downstream signal vectors of length $N-1$, m is the number of samples by which the tracer signal $y(n)$ is delayed by and has a value between $0 \le m \le M-1$, M is the maximum size in samples of the correlation window (see Figure 6.2). $R_{xy}(m)$ is a vector of size M containing a set of correlation coefficients taken over the set of delay intervals m.

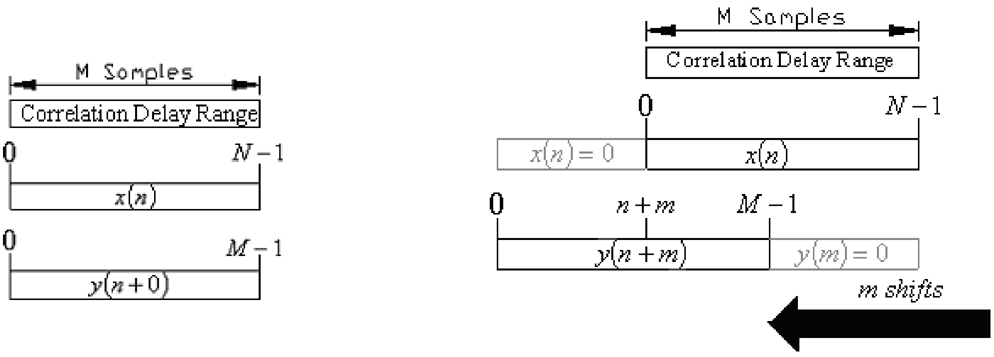

(a) Start of correlation (b) Correlation at m shifts

Figure 6.2 A Pictorial Representation of the Cross Correlation Process

The maximum peak of the discrete cross correlation function ($\hat{R}_{xy}(m)$ in Figure 6.3) occurs at $m = m_d$ and the transit time delay (τ_d) between $x(n)$and $y(n)$ can be obtained from Equation 6.4 where δt is the sample interval time.

$$\tau_d = m_d \delta t \qquad \textbf{Equation 6.4}$$

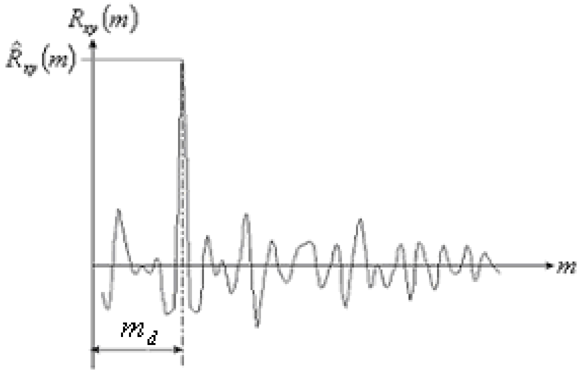

Figure 6.3 The Discrete Cross Correlation Function

6.2.2 Edge effect

A problem with the cross correlation of finite lengths of data is that as $y(n)$ is shifted to the left during the correlation process (see Figure 6.2), the waveform pairs no longer overlap and the data at the end of the of sequence no longer form pair products i.e.

$$\lim_{m \to (M-1)} R_{xy}(m) \to 0$$

This results in a linear decrease in the correlation's peak as the time delay between $x(n)$ and the $y(n)$ signals increases leading to doubtful values of $R_{xy}(m)$. This decrease in peak amplitude as m approaches ($M-1$) is known as the "end effect" and the value of $R_{xy}(m)$ is said to be "biased". This uncertainty can be compensated for by using a modified form of Equation 6.3 which gives the "unbiased" value of $R_{xy}(m)$.

$$R_{xy(unbiased)}(m) = \frac{1}{N-|m|}\sum_{n=0}^{N-1} x(n)y(n+m) \qquad \textbf{Equation 6.5}$$

Figure 6.4 shows a comparison between the biased and unbiased peak values of $R_{xy}(m)$. As can be seen from Figure 6.4 the unbiased peak value for $R_{xy}(m)$ at $m = m_d$ remains constant at approximately $R_{xy}(0)$ as the delay between the signals increases. It only deviates significantly from this value as m approaches ($M-1$), due to the increase in the statistical variance of $R_{xy}(m)$ [53].

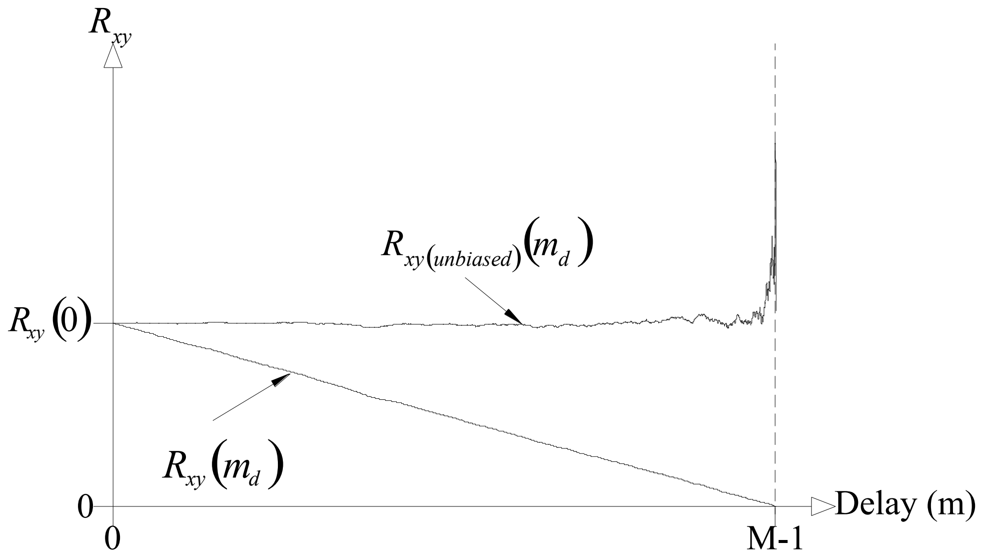

Figure 6.4 Comparison between the biased and unbiased values of $\hat{R}_{xy}(m)$

6.2.3 Pearson's ρ Coefficient

Because $R_{xy}(m)$ is calculated from the product pairs of $x(n)$ and $y(n)$, the relative amplitudes of $x(n)$ and $y(n)$ will also have an affect on the magnitude of $R_{xy}(m)$. Providing the mean values of $x(n)$ and $y(n)$ are both equal to zero the affect of the amplitudes of $x(n)$ and $y(n)$ on $R_{xy}(m)$ can be compensated for by normalising $R_{xy}(m)$ by the factor [24];

$$\frac{1}{N}\sqrt{\sum_{n=0}^{N-1} x(n)^2 \sum_{n=0}^{N-1} y(n)^2}$$

Equation 6.6 gives the Pearson's cross correlation coefficient from $R_{xy}(m)$ which results in a value of ± 1 as an indication of the strength of the correlation between $x(n)$ and $y(n)$. A value of 1 for $\rho_{xy}(m)$ signifies 100% in-phase correlation, whilst a value of -1 for $\rho_{xy}(m)$ signifies 100% anti-phase correlation, and a value of $\rho_{xy}(m) = 0$ signifies no correlation.

$$\rho_{xy}(m) = \frac{R_{xy}(m)}{\frac{1}{N}\sqrt{\sum_{n=0}^{N-1} x(n)^2 \sum_{n=0}^{N-1} y(n)^2}} \qquad \textbf{Equation 6.6}$$

6.3 Measurement Accuracy

6.3.1 Statistical Errors in Time Delay Measurement

The statistical accuracy of time delay measurement is influenced by three major factors; [54];

i. The total correlation delay range time T. As stated previously, due to the fact that cross correlation calculations are made over a definite time period the measured cross correlation function is only an approximation of the true cross correlation function. This approximation introduces an indeterminate statistical scattering of the measured transit time. Longer delay time ranges produce more accurate results.

ii. The signal's bandwidth B (see Chapter 3, Section 3.3). Figure 6.5 depicts how the effective bandwidth can be estimated from Pearson's normalised cross correlation function $\rho_{xy}(\tau)$.

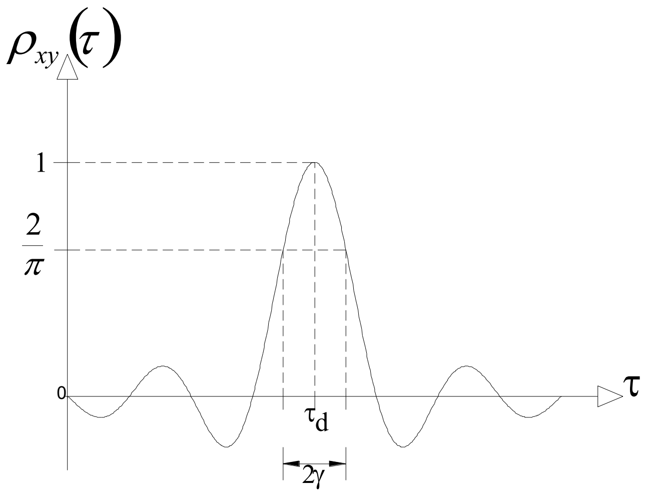

Figure 6.5 Determination of System Bandwidth from $\rho_{xy}(\tau)$

Where γ is determined from the $\rho_{xy}(\tau) = \frac{2}{\pi}$ points relative to the peak of the correlation function corresponding to the transit delay time τ_d between the $x(t)$ and $y(t)$ signals, the bandwidth is given by Equation 6.7. Wider bandwidths produce more accurate results.

$$B = \frac{1}{4\gamma} Hz$$ **Equation 6.7**

iii. The normalised cross correlation coefficient $\rho_{xy}(\tau)$. The greater the similarity between the reference and tracer signals produces more accurate results. Similarity between signals can be influenced by such things as the spacing between the upstream and downstream flow sensors, where the flow regime between the two sensors could start to break up causing an increase in the signal to noise ratio of the tracer signal.

$$\text{Normalised Mean Square Error} = \varepsilon(\tau) = \frac{1}{\sqrt{2BT}} \sqrt{1 + \frac{1}{\rho_{xy}(\tau)^2}}$$ **Equation 6.8**

As it can be seen from Equation 6.8 [55], the normalised mean square error is dependant on the observation time (T), system bandwidth (B) and the magnitude of the correlation coefficient ($\rho_{xy}(\tau)$). Equation 6.8 also implies that, longer observation times, wide system bandwidths and a strong similarity between the reference and tracer signals will reduce the normalised mean square error.

6.3.2 Velocity Discrimination Factor

The Velocity Discrimination Factor (VDF) is used as an indication of the cross correlation flowmeter's ability to accurately resolve small changes in flow velocity. The VDF is defined as the ratio of the change in measured velocity (Δv) to the maximum required velocity to be measured ($v_{\max}$). The VDF of the flowmeter can be determined from Equation 6.9 [24].

$$VDF = \frac{\Delta v}{v_{\max}} = \pm \frac{\delta t\, v}{2l} = \pm \frac{\delta t}{2\tau_d} = \pm \frac{1}{2m_d}$$ **Equation 6.9**

Where:

δt is the sample interval.

l is the distance between the signal and tracer sensors (see Figure 6.1).

v is the measured flow velocity.

m_d is the number of samples corresponding to the maximum peak position (see Figure 6.3) where; $m_d = \frac{\tau_d}{\delta t}$.

Equation 6.9 implies that as measured flow velocity increases (corresponding to a decrease in τ_d), the accuracy of the measured velocity declines drastically to as much as $\pm 50\%$ as the actual measured velocity approaches the possible maximum measureable velocity ($\tau_d = \delta t$). The choice of sensor spacing (l) and a suitable sample interval (δt) when designing a cross correlation flowmeter is entirely dependant on the measurable flow range ($v_{\min}$ and $v_{\max}$) and the required accuracy of the velocity measurement at $v_{\max}$.

6.4 Computational Methods of Calculating the Cross Correlation Function

6.4.1 Direct Methods

Direct methods of cross correlation are based on the computational expansion of Equation 6.3 to produce a set of data points ($R_{xy}(0), R_{xy}(1), R_{xy}(2), \cdots, R_{xy}(M-1)$) corresponding to the correlation function $R_{xy}(m)$. This is achieved by either the point-by-point method or the evolutionary method as described below.

6.4.1.1 Point-by-Point Method

The point-by-point method involves the calculation of individual points of the cross correlation function curve (Figure 6.6) by repeated dot product multiplication of the $x(n)$ signal vector by the sample shifted $y(n+m)$ signal vector to produce a resultant vector containing a set of data points corresponding to $R_{xy}(m)$.The total number of sample shifts performed is determined by the size of the correlation delay range (see Figure 6.2).

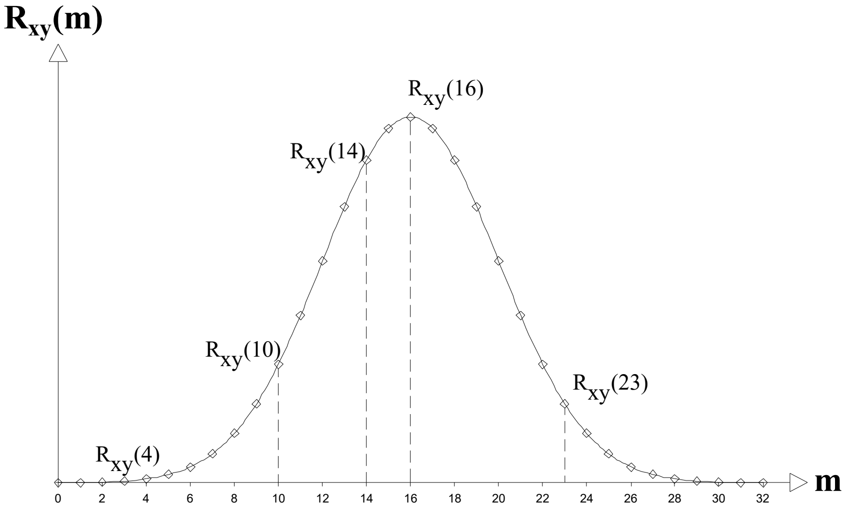

Figure 6.6 Point-by-Point Cross Correlation

This process also referred to as the “sliding dot product” of the $x(n)$ and $y(n)$ signal vectors, is shown conceptually in Figure 6.7.

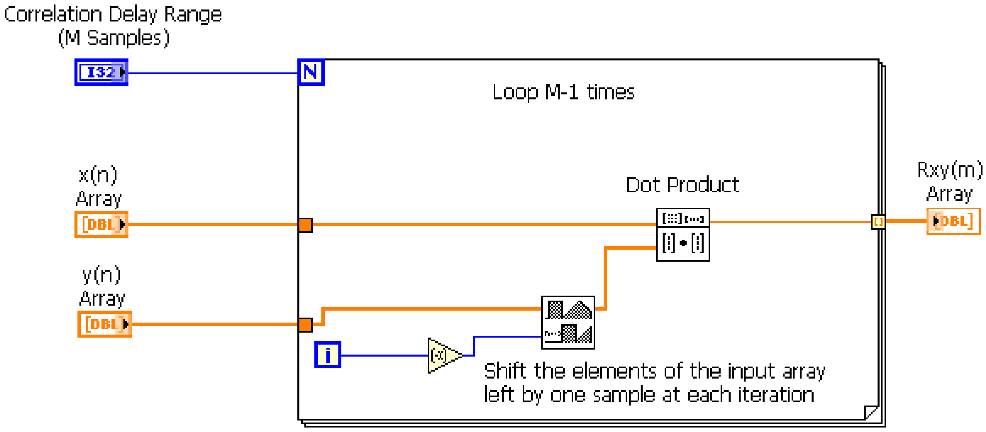

Figure 6.7 Conceptual LabVIEW Diagram of Point-by-Point Cross Correlation

6.4.1.2 Evolutionary Method

Unlike the point-by-point method which produces a single $R_{xy}(m)$ value per iteration from the dot product of the $x(n)$ and $y(n)$ vectors. The evolutionary method produces a full set of $R_{xy}(m)$ values in the form of a growing cross correlation curve.

$$R_{xy}(m) = \underbrace{\underbrace{\underbrace{x(0)\begin{bmatrix} y(0) \\ y(1) \\ y(2) \\ \vdots \\ y(M-1) \end{bmatrix}}_{1^{st}\ evolution} + x(1)\begin{bmatrix} y(1) \\ y(2) \\ y(3) \\ \vdots \\ y(M) \end{bmatrix}}_{2^{nd}\ evolution} + \ldots + x(N-1)\begin{bmatrix} y(M-1) \\ y(M) \\ y(M+1) \\ \vdots \\ y(N+M-2) \end{bmatrix}}_{m^{th}\ evolution} \tag{Equation 6.10}$$

Equation 6.10 shows how the evolutionary method for calculating the cross correlation function from $x(n)$ and $y(n)$ vectors is achieved. On the first evolution, all elements of the $y(n)$ vector are multiplied by the first element of the $x(n)$ vector to produce the initial $R_{xy}(m)$ curve vector. On the second evolution, the $y(n)$ vector is shifted by one sample then all elements of the shifted $y(n)$ vector are multiplied by the second element of the $x(n)$ vector to produce a second $R_{xy}(m)$ curve vector which is then added to the previous curve vector. This process of shifting, multiplying, and then adding, is repeated over the required correlation delay range to produce a final curve vector value for $R_{xy}(m)$ which is identical to the curve produced by the point-by-point method.

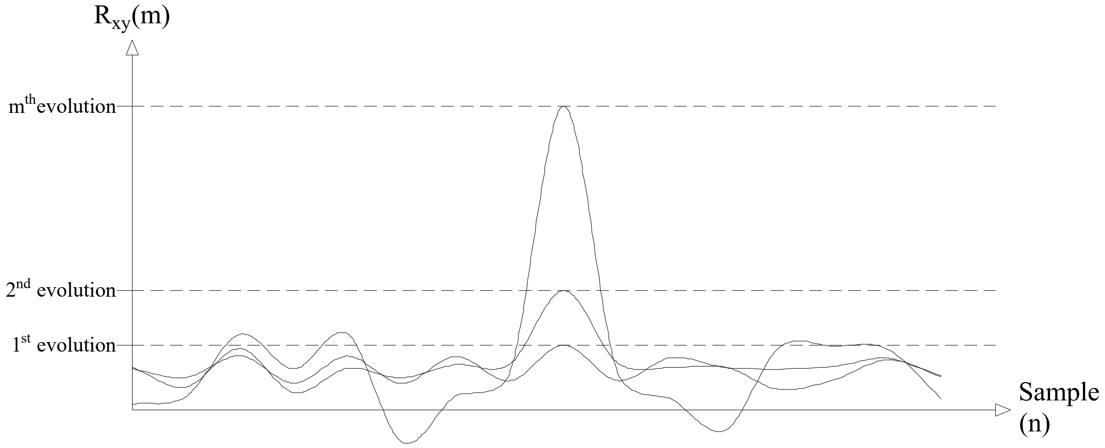

Figure 6.8 Evolutionary Cross Correlation Curves

Despite the similarity the evolutionary method has with the point-by-point method, the evolutionary method produces a continually growing curve (Figure 6.8) which allows for a more rapid but less accurate determination of the transit delay τ_d from the peak generated by one of its earlier iterations [24].

6.4.2 Frequency Domain Method

6.4.2.1 Fast Fourier Transform (FFT)

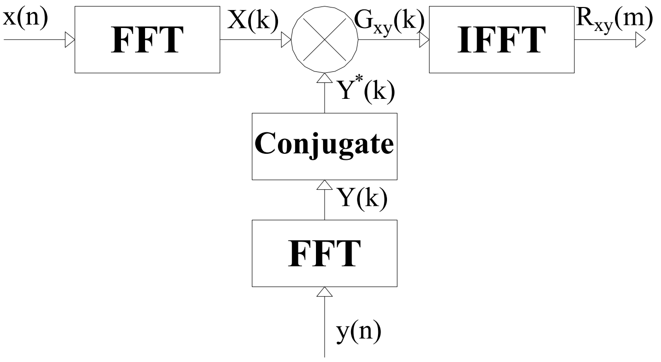

Figure 6.9 The FFT Method for Calculating the CCF

The Fast Fourier Transform (FFT) method for calculating the cross correlation function is depicted in Figure 6.9. Here, the cross correlation function $R_{xy}(m)$ is found from the Inverse Fast Fourier Transform (IFFT) of the FFT of the $x(n)$ series multiplied by the conjugate of the FFT of the $y(n)$ series which is given by [55]:

$$R_{xy}(m) = IFFT(G_{xy}(k))$$ **Equation 6.11**

Where:

$G_{xy}(k) = X(k)Y^*(k)$

$X(k) = FFT(x(n))$

$Y^*(k) = CONJUGATE(Y(k))$

$Y(k) = FFT(y(n))$

This method for computing the cross correlation series is particularly useful for larger $x(n)$ and $y(n)$ vectors where the computational efficiency of the FFT can significantly reduce the time required to compute the cross correlation series [56].

6.5 The Measurement of Solids Mass Flow using LabVIEW

6.5.1 VI Overview

The VI routines which collect the cross correlation data from the upstream and downstream ECT sensors is an extended version of the dual-plane 8-electrode imaging VI system as described in Chapter 5, Section 5.2.2.3.

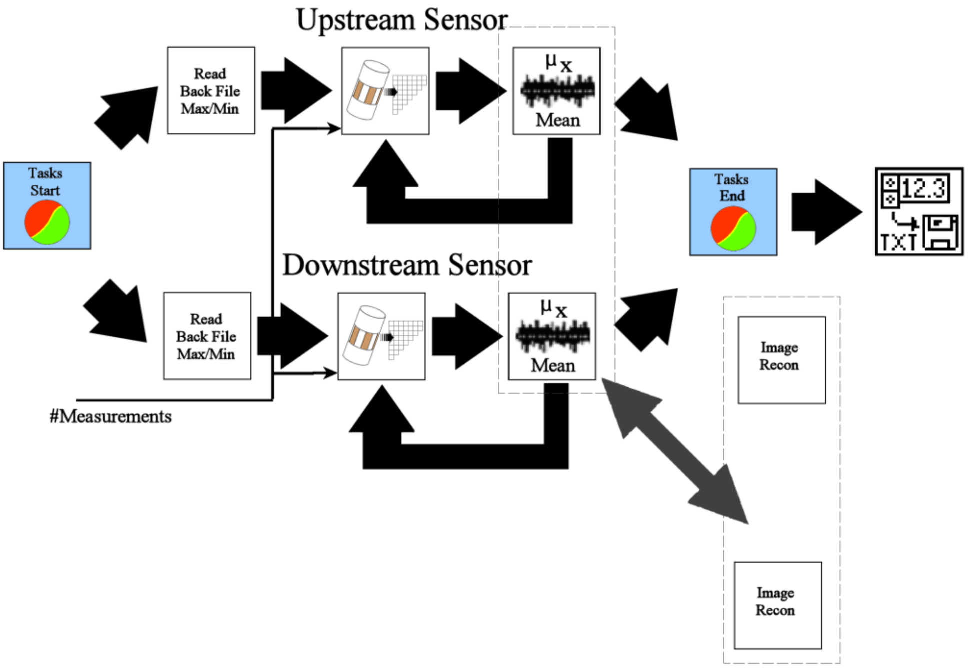

Figure 6.10 The Dual-Plane 8-Electrode Imaging VI Parallel Sequence Structure with Modifications for Collecting Cross Correlation Data

The modified imaging system is depicted in Figure 6.10. The image reconstruction and image display VIs adds a significant time overhead to the operation of the whole system. This depreciates the data capture rate of image frames and hence the cross correlation sample interval δt . A dual mode system was implemented to reduce this, where the system would operate in either one of two modes; real time tomographic imaging or, cross correlation data capture.

In cross correlation data capture mode the average of the normalised capacitance data taken from ECT sensors for each image frame, is stored on exit from the imaging software run. The average of the normalised capacitance data for each image frame is given by Equation 6.12.

$$\overline{V_{NC}} = \frac{1}{N_{CM}} \sum_{n=0}^{N_{CM}-1} V_{NC}(n) \qquad \textbf{Equation 6.12}$$

Where:

$V_{NC}(n)$ is the n^{th} normalised capacitance measurement taken from the ECT sensors (see Chapter 4, Section 4.2.2.1).

N_{CM} is the total number of independent normalised capacitance measurements taken from the ECT sensor. Variations in the capture rate of each frame (corresponding to the cross correlation sample interval δt) can be achieved by specifying the total number of independent measurements taken from the ECT sensors (Figure 6.11).

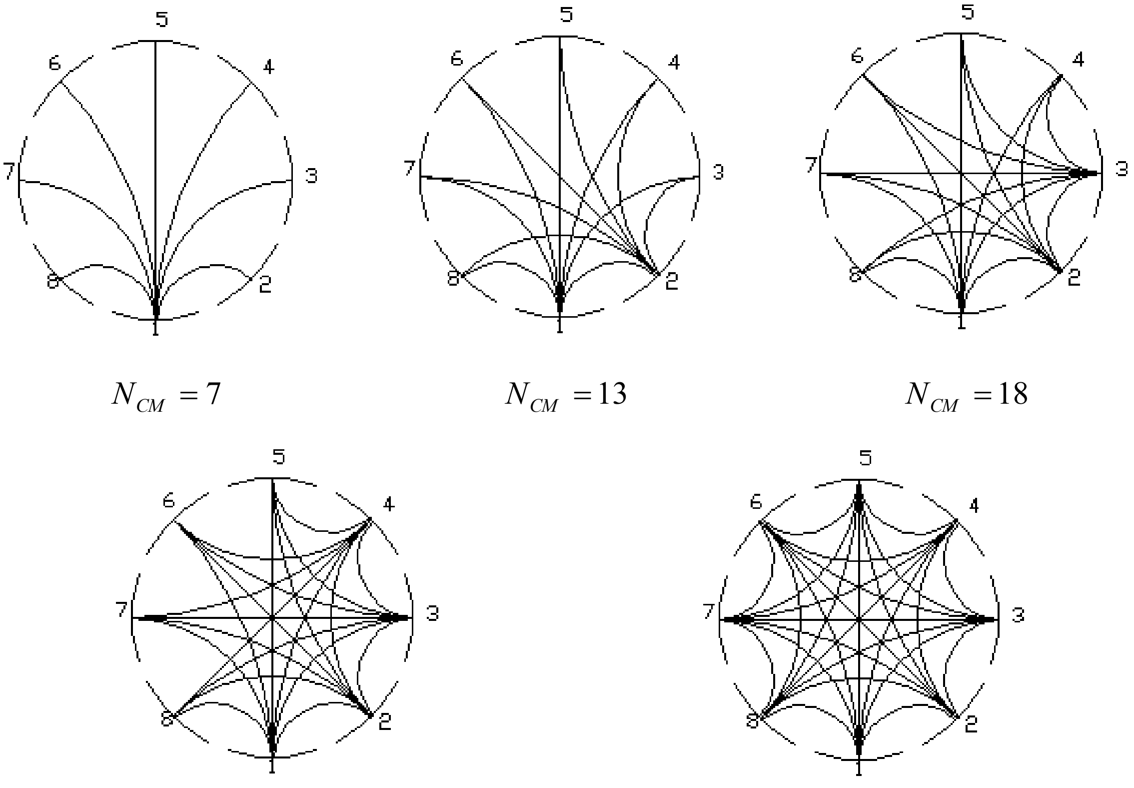

$N_{CM} = 7$ $N_{CM} = 13$ $N_{CM} = 18$

$N_{CM} = 22$ $N_{CM} = 28$

Figure 6.11 Measurement Number Options Available in Cross Correlation Data Capture Mode

Figure 6.12 shows a typical flow profile of averaged normalised capacitance values ($\overline{V_{NC}}$) taken from one of the ECT sensors.

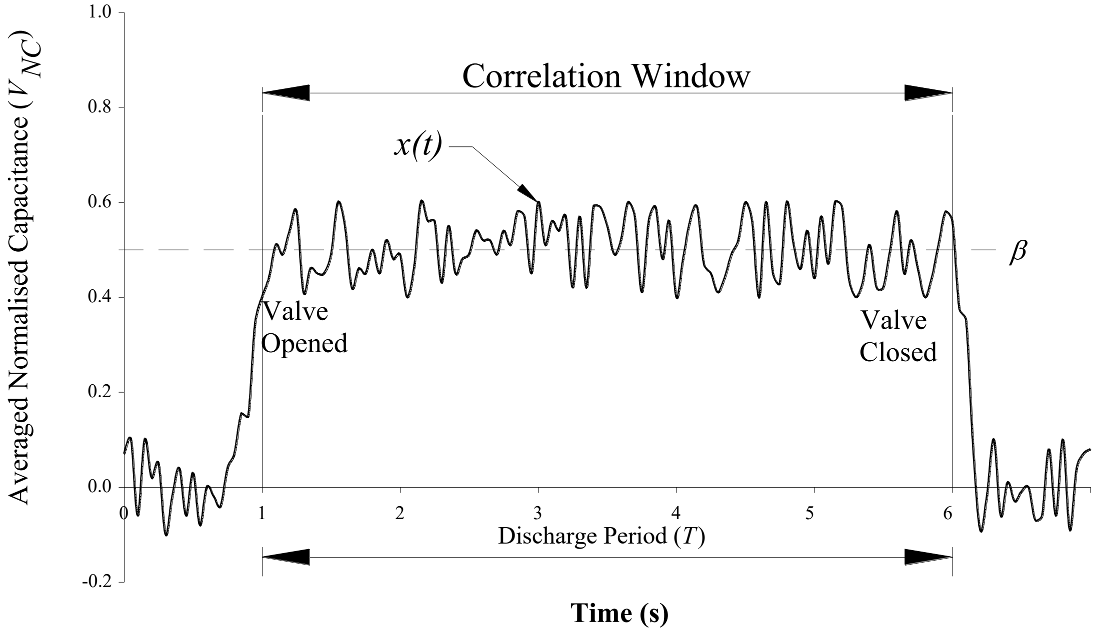

Figure 6.12 Typical Flow Profile of $\overline{V_{NC}}$ Values Taken from One of the ECT Sensors

As it can be seen from Figure 6.12, the measured averaged normalised capacitance signal taken from the sensor over the discharge period (T) contains two components (Equation 6.13).

$$\overline{V_{NC}(t)} = x(t) + \beta$$ **Equation 6.13**

Where:

$x(t)$ is a random noise pattern, caused by the naturally occurring random flow as the solids material passes through the sensor.

β is the mean volumetric concentration of the solids material over the discharge period (T) and is given by Equation 6.14 [57]:

$$\beta = \frac{1}{M}\sum_{m=0}^{M-1}\overline{V_{NC}}(m)$$ **Equation 6.14**

Where:

$\overline{V_{NC}}(m)$ is the m^{th} averaged normalised capacitance value, taken from the ECT sensor.

M is the total number of samples taken during the discharge period (T).

The instantaneous solids mass flow rate can be inferred from the captured data by Equation 6.15.

$$\dot{m}_i(t) = \rho \, v \, A \, (x(t) + \beta) \qquad \textbf{Equation 6.15}$$

Where:

$\dot{m}_i(t)$ is the instantaneous mass flow rate $\left(\frac{kg}{s}\right)$.

ρ is the true density of the solids material $\left(\frac{kg}{m^3}\right)$.

A is the cross sectional area of the pipe $\left(m^2\right)$.

v is the solids velocity $\left(\frac{m}{s}\right)$. This is given from the cross correlation of the random noise patterns taken from the upstream ($x(t)$ in Figure 6.13) and downstream ($y(t)$ in Figure 6.13) ECT sensors.

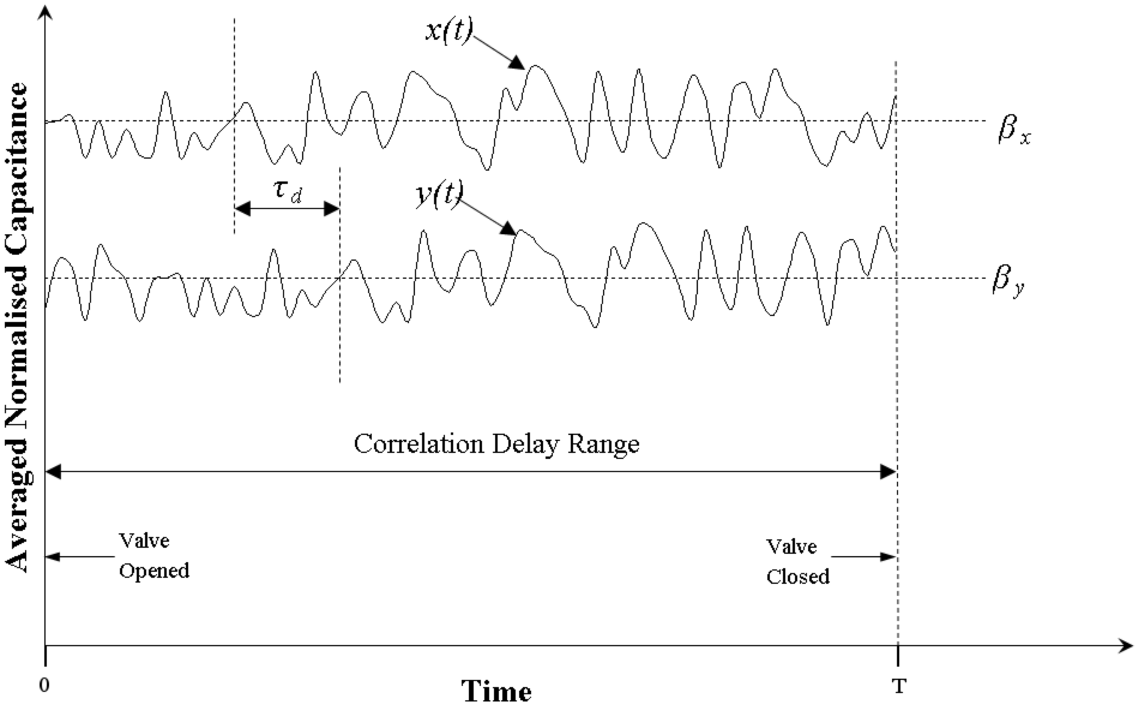

Figure 6.13 Typical Averaged Normalised Capacitance Measurements ($\overline{V_{NC}}$) Taken from the Upstream and Downstream ECT Sensors

Assuming that the solids velocity (v) remains constant over the total discharge period (T), the mean solids mass flow rate over the total discharge period can be directly calculated from the captured data by Equation 6.16.

$$\dot{m} = \rho \; v \, A \; \beta \qquad \textbf{Equation 6.16}$$

Where:

$\dot{m}$ is the mean solids mass flow rate $\left(\dfrac{kg}{s}\right)$.

Figure 6.13 shows a segment, between the "valve opened" and "valve closed" positions of the flow profile see Figure 6.12, of typical averaged normalised capacitance measurements ($\overline{V_{NC}}$) taken from the upstream and downstream ECT sensors.

The averaged normalised capacitance measurements taken from the upstream and downstream ECT sensors contain the time delayed random noise patterns necessary for time delay measurement by cross correlation. Accurate time delay measurement can only obtained be firstly, separating from the averaged normalised capacitance measurements the two random signal patterns $x(t)$ and $y(t)$, followed by the cross correlation of these two random signal patterns as explained below.

The cross correlation function of upstream and downstream signals shown in Figure 6.13, is given by Equation 6.17 (see Appendix A).

$$R_{xy}(\tau) = \lim_{T\to\infty} \frac{1}{T} \int_0^T x(t)\, y(t+\tau)\, dt + \lim_{T\to\infty} \frac{1}{T} \int_0^T \beta_x \;\beta_y \; dt \qquad \textbf{Equation 6.17}$$

Where:

$x(t)$ is the random noise pattern of the averaged normalised capacitance as the solids material passes through the upstream sensor.

$y(t)$ is the random noise pattern of the averaged normalised capacitance as the solids material passes through the downstream sensor.

β_x is the mean volumetric concentration of the solids material in the upstream sensor.

β_y is the mean volumetric concentration of the solids material in the downstream sensor.

As it can be seen from the above equation, the total cross correlation function is the sum of the cross correlation function of two random noise pattern signals, ($x(t)$ and $y(t)$) and, the cross correlation function of two mean volumetric concentration values (β_x and β_y). Equation 6.18 is a simplified version of Equation 6.17.

$$CCF = CCF_{xy} + CCF_{\beta}$$ **Equation 6.18**

Where:

CCF is the total cross correlation function.

CCF_{xy} is the cross correlation function of two random noise pattern signals, $x(t)$ and $y(t)$.

CCF_{β} is the cross correlation function of two mean volumetric concentration values β_x and β_y.

Figure 6.14 shows why care has to taken when cross correlating the two averaged normalised capacitance signals as shown in Figure 6.13. If the two mean solids volumetric concentration values are large compared to the maximum peak to peak amplitude of the two random noise pattern signals, CCF_{β} will be much greater than CCF_{xy}. This will result in a total cross correlation function that is dominated by the CCF_{β} portion of the cross total correlation function. This is because the discrete cross correlation of two constant values results in a triangular shaped correlation function with its peak at $\tau = 0$. This triangular shaped correlation function obscures the CCF_{xy} portion of the cross correlation function which contains the required correlation peak from which the correct transit delay time (τ_d) can be determined.

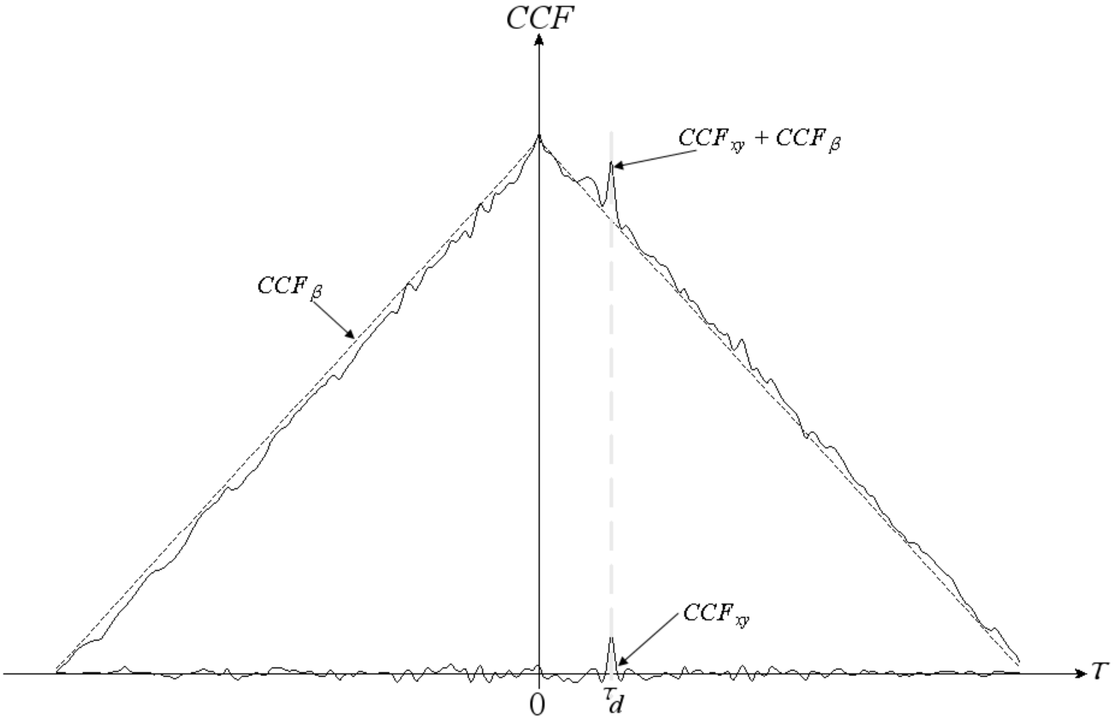

Figure 6.14 The Domination of CCF_{β} Obscures the Actual Required Peak Value

6.5.2 The Virtual Instrument Measuring System's Cross Correlation Function Virtual Instrument (CCF.VI)

6.5.2.1 LabVIEW's Cross Correlation VI

The fundamental VI on which all subsequent cross correlation measurements for the MMU Virtual Instrument Measuring System are based is the "CrossCorrelation" VI as supplied by National Instruments which is part of the VI library supplied with the LabVIEW software package.

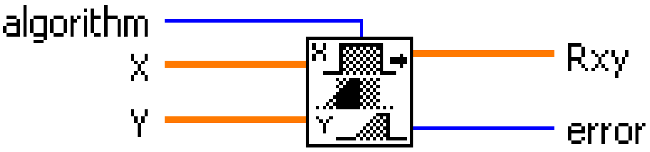

Figure 6.15 LabVIEW's Cross Correlation VI

This VI as shown in Figure 6.15, performs a dual sided cross correlation (Rxy) of the supplied X and Y input vectors according to Equation 6.19.

$$R_{xy}(\tau) = \frac{1}{2T}\int_{-T}^{T} x(t)y(t+\tau)$$ **Equation 6.19**

Unlike the single sided correlation described in Section 6.4, which can only produce a correlation peak for time-lagging $y(n)$ vectors with respect to the $x(n)$ vector. Double sided cross correlation is capable of producing correlation peaks for both time-leading and for time-lagging $y(n)$ vectors with respect to the $x(n)$ vector. The discrete form LabVIEW's double sided cross correlation VI is given by Equation 6.20 and, is depicted by Figure 6.16.

$$R_{xy}(m) = \sum_{n=0}^{N-1} x(n)y(n+m)$$

Equation 6.20

$$m = 0,1,2,\cdots,N+M-2$$

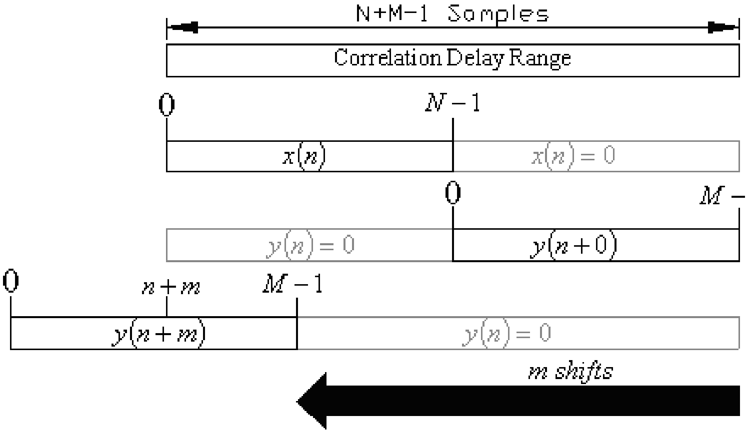

Figure 6.16 Discrete Double Sided Cross Correlation

LabVIEW's cross correlation VI uses the X vector of size N and, the Y vector of size M to produce, either by direct or by frequency domain computation (set by the "Algorithm" input in Figure 6.15), the cross correlation function Rxy, of size N+M-1 [56].

6.5.2.2 The CCF.VI

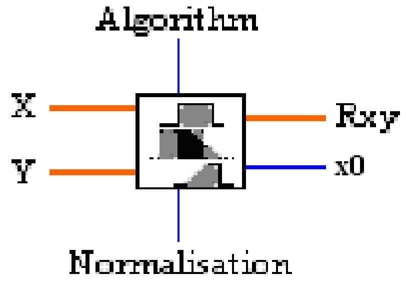

(a)

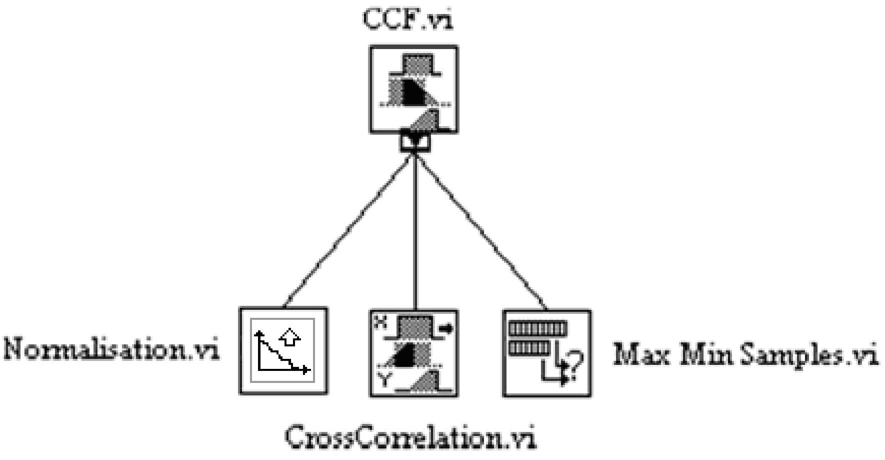

(b)

Figure 6.17 (a) The MMU Virtual Instrument Measuring System CCF.VI and, (b) the Hierarchal Diagram of the CCF.VI

The MMU Virtual Instrument Measuring System Cross Correlation Function VI (CCF.VI) is shown in Figure 6.17. As it can be seen from the hierarchal diagram of the CCF.VI (Figure 6.17b), LabVIEW's cross correlation VI is central to this VI. In addition, the Rxy output of the CCF.VI can optionally be changed. These options are;

a) No change (None), the output is the same as the one produced by LabVIEW's cross correlation VI.
b) Biased, the Rxy vector produced by LabVIEW's cross correlation VI is divided by the larger of N or M (MAX(N,M)). Where N and M are the corresponding sizes of the X and Y input vectors.
c) Unbiased, the Rxy vector produced by LabVIEW's cross correlation VI is adjusted to reduce edge effect (see Section 6.2.2).

d) ρ Coefficient, the Rxy vector produced by LabVIEW's cross correlation VI is adjusted to a peak correlation value between 0 and 1 (see Section 6.2.3).

Figure 6.18a shows an example of two, 16 element, X and Y signal input sequences applied to LabVIEW's cross correlation VI as described in Section 6.5.2. Here the Y signal lags the X signal by four samples. Figure 6.18b shows the resulting cross correlation sequence as taken from the VI's Rxy output.

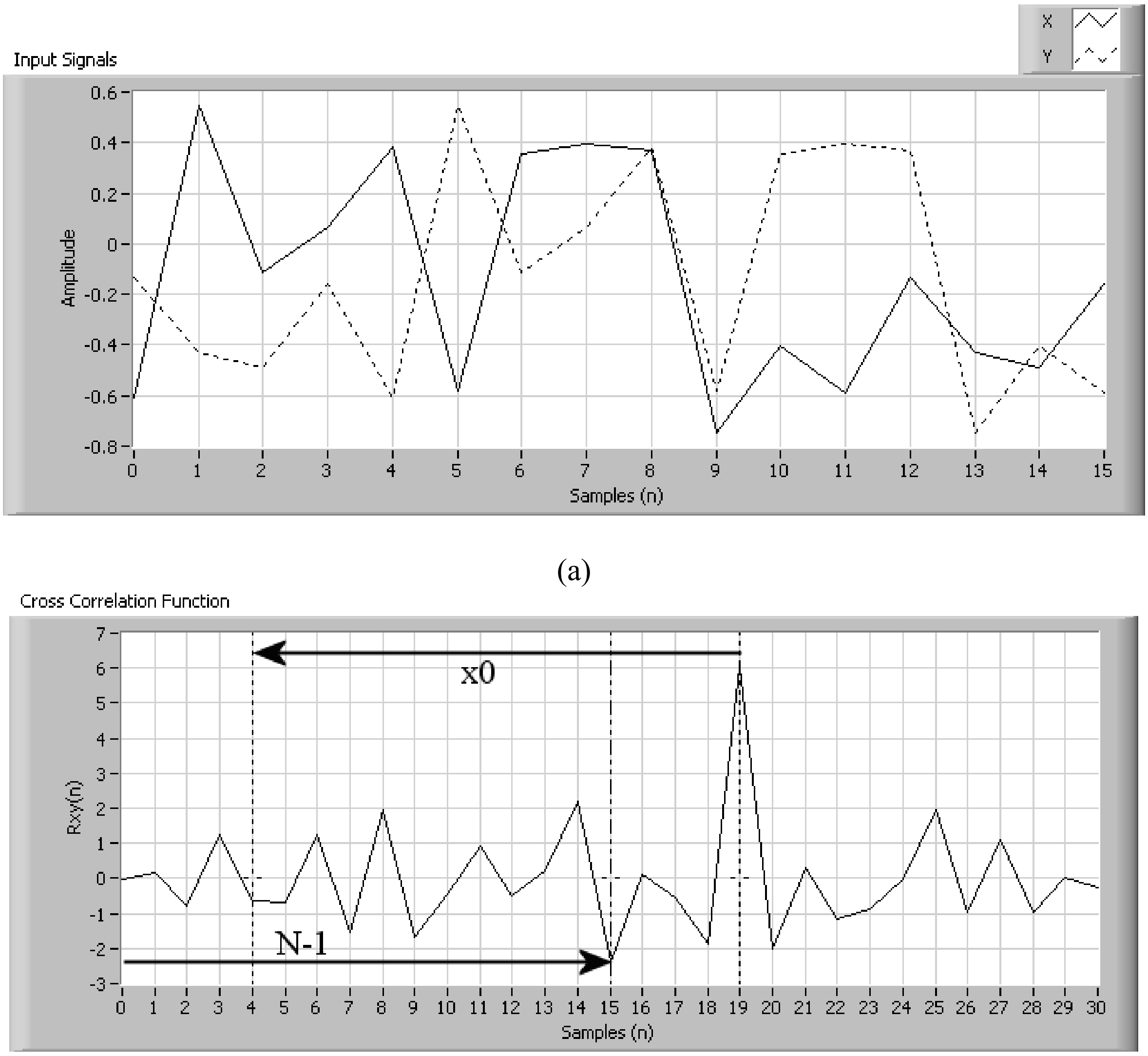

(a)

(b)

Figure 6.18 An Example of the X and Y Signal Input Sequences and the Resulting Rxy Output Sequence as Applied to and Taken from, LabVIEW's CrossCorrelation VI

Because LabVIEW cannot index arrays with negative numbers, the nth sample corresponding to a zero time shift will be shifted by (N-1) samples (see Figure 6.18b).

Where N is whichever of the two input sequences (X or Y) contains the largest number of individual elements. Consequently, in this particular case, the n^th^ sample which corresponds to the correlation's peak occurs at the 19th sample and not at the 4th as expected. The CCF.VI (as shown in Figure 6.17a) provides a suitable offset correction value (x0) which when added to the correlation peak's sample index, gives the correct nth sample shift. The correction value (x0) is given by Equation 6.21.

$$x0 = 1 - MAX(SIZE(X), SIZE(Y))$$ **Equation 6.21**

Figure 6.19 shows how the CCF.VI determines the transit delay time τ_0 from the Rxy sample sequence. Firstly, LabVIEW uses the "Array Max & Min" VI to find the sample index of the correlation's peak which is corrected by adding x0 to this value. The result of this is then multiplied by the sample interval time δt, to give the transit delay time τ_d.

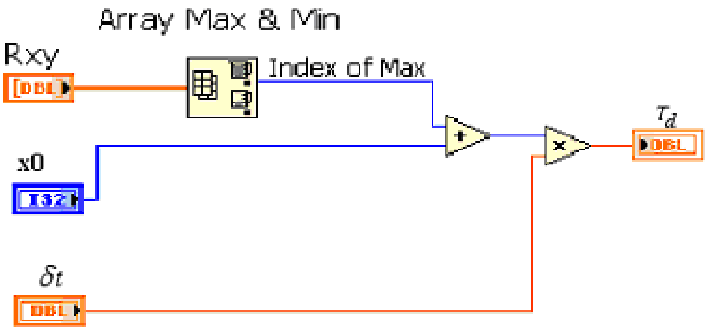

Figure 6.19 Obtaining the Delay Time from Rxy

Part of the function of the CCF.VI is to separate the $x(n), y(m), \beta_x$ and, β_y information from the X and Y signal input sequences before correlation (Figure 6.20). This is achieved by utilising LabVIEW's "Mean.vi" which firstly, computes the average value of the X and Y input sequences to supply values for β_x and, β_y. The β_x and, β_y values are then subtracted from the X and Y input sequences to leave only the $x(n)$ and, $y(m)$ sequences, which are then passed on to LabVIEW's "CrossCorrelation" VI.

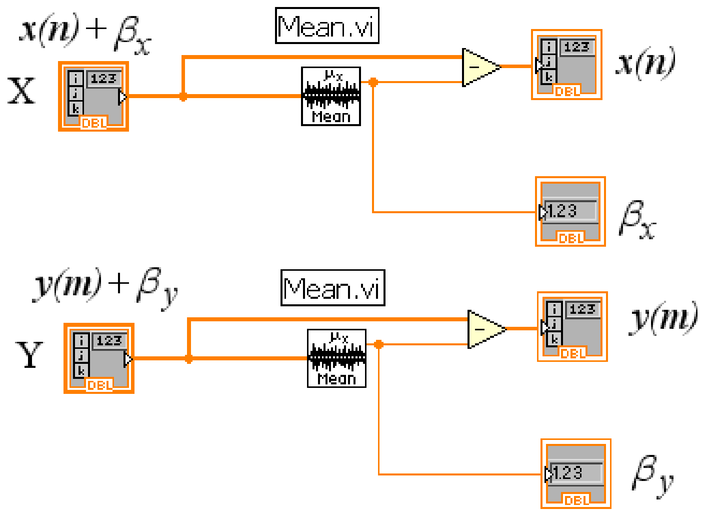

Figure 6.20 Separation of the $x(n), y(m), \beta_x$ and, β_y Information from the X and Y Signal Input Sequences by the Use of LabVIEW's "Mean.vi"

6.6 Conclusion

The two major factors which have the greatest affect on the accuracy of flow velocity measurement by the cross correlation method is the sample interval time δt, the correlation delay range over which the cross correlation process was calculated T (correlation window). Generally lower sampling intervals (δt) lead to a more precise measurement of the transit delay time (τ_d) hence greater accuracy of flow velocity measurement. Shorter sampling intervals could lead to cross correlation peak positions which occur too close to end of the correlation delay range where the peak is at risk of becoming lost due to edge affect and associated increase in statistical variance. Longer correlation delay ranges (T) will ensure suitable cross correlation peak positions but at the expense of overall correlation times. The design of a cross correlation flow meter is usually a case of finding the correct balance between the sample interval time and the delay range, and to a lesser extent the axial spacing between the sensors l, over a specified measurement range ($v_{\min}$ and $v_{\max}$) for a required velocity discrimination.

If the solids flow is of primary interest, a homogeneous two-phase solids/gas mixture can be regarded as a single-phase solids flow. If the solids/gas mixture is viewed as a single-phase solids flow and the solids material is known to be moving at a constant velocity for the duration of the measurement period. Then only a single cross correlation measurement is required in order to calculate either the instantaneous or mean solids mass flow, from the instantaneous or mean volumetric concentration value obtained from just a single ECT sensor placed in a suitable position in the flow's path.

Chapter Seven

7 Results

7.1 Introduction

This chapter describes the sequence of tests performed on the MMU Virtual Instrument Measuring System in conjunction the MMU Flow Rig in order to evaluate how the measuring system performs as a velocity/solids mass flowmeter.

The chapter examines the relationship between the actual measured mass flow and the mean volumetric concentration compared to the number of independent normalised capacitance measurements taken from the upstream ECT sensor.

The collected data is presented and compared to a series of LabVIEW simulations of mean volumetric concentration measurements corresponding to a solid object, of increasing size, placed in various crosswise positions inside a virtual ECT sensor.

Results are presented for the pellet velocity measurements which were evaluated by the cross correlation of the collected data. The accuracy of the pellet velocity measurements are then compared to the number of independent normalised capacitance measurements taken from the upstream and downstream ECT sensor.

The calculated value for the true density of the solids material is presented and compared to the standard true density of the solids material.

The chapter finishes by summarising the issues arising from the assessment of the presented data.

7.2 Results

7.2.1 Vertical Mass Flow Measurement

The purpose of the experiment is to examine the relationship between the cross-sectional mean volumetric concentration of the moving polypropylene pellets (β) and the measured mass flow ($\dot{m}$) over a range of averaged normalised capacitance measurements taken from the ECT sensor.

Figure 7.1 shows in diagrammatical form the vertical gravity-conveyed section of the MMU flow rig as introduced in Chapter 1, Section 1.2.1. As stated in this section, the gravitational mass flow rate of the polypropylene pellets delivered by the pellet header tank is controlled by a pellet control feeder valve. The mass flow is measured by the "bucket-and-stopwatch" technique where the total mass discharge of the gravity-conveyed polypropylene pellets over a five second fixed time period is weighed by a digital weighing scale and the mass flow is calculated by dividing the measured mass by the fixed time period.

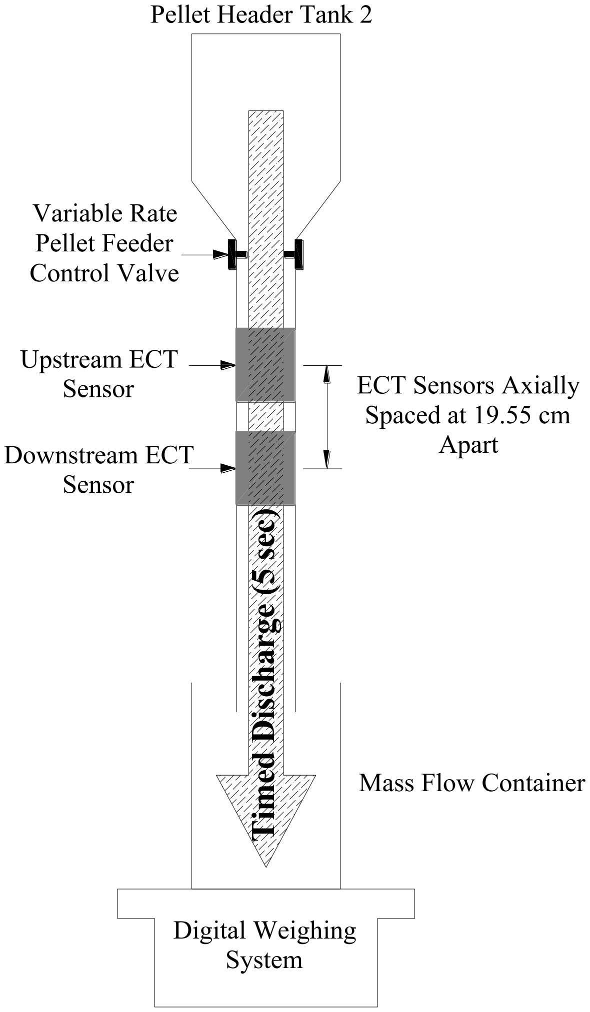

Figure 7.1 Vertical Gravity-Conveyed Flow Section of the MMU Flow Rig

The pellet control feeder valve is fitted with a calibrated scale of 0 to 10; where 0 corresponds to zero flow (valve fully shut) and 10 corresponds to the maximum obtainable flow (valve fully opened). Preliminary investigations demonstrated that for valve aperture settings lower than 4 resulted in mass flow rates too small to be practically detected by the tomographic imaging hardware and valve aperture settings higher than 6 resulted in a total mass discharge (over the five second fixed time test period) beyond the operational limit of the digital weighing scales. Because of these limitations, it was decided that valve aperture settings of 4, 5, and 6 gave suitable distinctive changes of measured mass flow rate for the trials.

During the discharge period, the LabVIEW virtual instrumentation software collects the averaged normalised capacitance values ($\overline{V_{NC}}$) from the upstream and downstream ECT sensors which is stored as a data file at the end of each trial. The sample interval time (δt) between averaged normalised capacitance values ($\overline{V_{NC}}$) is dependant upon the actual number of independent averaged normalised capacitance measurements (N_{CM}) taken from the upstream and downstream ECT sensors (see Chapter 6, Section 6.5).

Total Number of Normalised Capacitance Measurements N_{CM}	**Sample Interval Time** δt **(ms)**
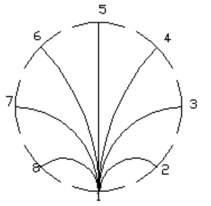 7	2.5
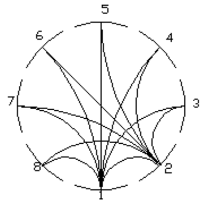 13	4.9
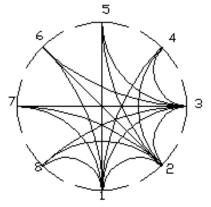 18	7.3
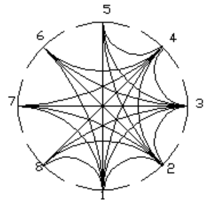 22	9.4
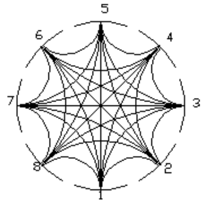 28	16.6

Table 7.1 The Total Number of Independent Averaged Normalised Capacitance Measurements (N_{CM}) Taken from the ECT Sensors and its Associated Sample Interval Time (δt)

The total number of independent averaged normalised capacitance measurements (N_{CM}) taken from the upstream and downstream sensors and its associated sample interval time (δt) is shown in Table 7.1

Each trial followed the subsequent procedure:

1. For each valve aperture setting (4, 5 and 6) the mass flow data was measured and recorded along with the resulting averaged normalised capacitance data set ($\overline{V_{NC}}$), which is stored as a data file.

2. The above process is repeated for N_{CM} values of 7, 13, 18, 22 and 28 measurements respectively.
3. The post processing and analysing the collected averaged normalised capacitance data enabled values for the cross-sectional mean volumetric concentration (β) to be evaluated. By cross correlation, the transit time of polypropylene pellets between upstream ECT sensor and the downstream ECT sensor (τ_d) was evaluated.
4. the above steps 1 to 3 were repeated four times to obtain overall an average value for the measured mass flow ($\dot{m}$) and the cross-sectional mean volumetric concentration (β).

A total of three such trials was performed, the results of which are show in Figures 7.2, 7.3 and, 7.4.

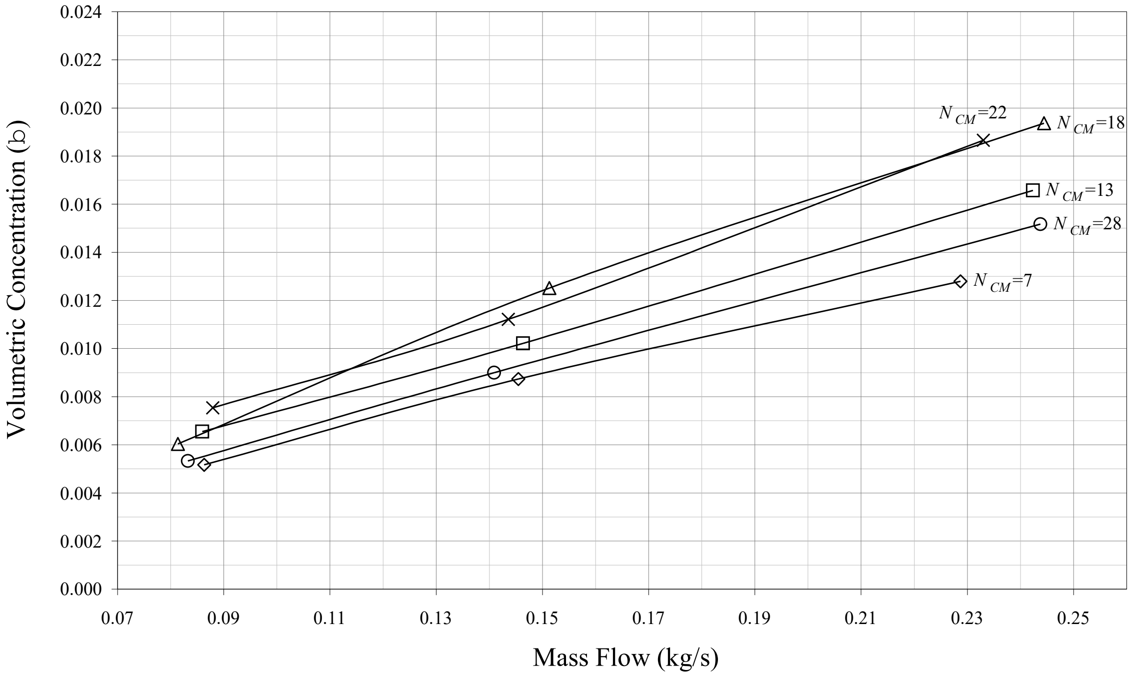

Figure 7.2 Mass Flow vs. Volumetric Concentration for Trial 1

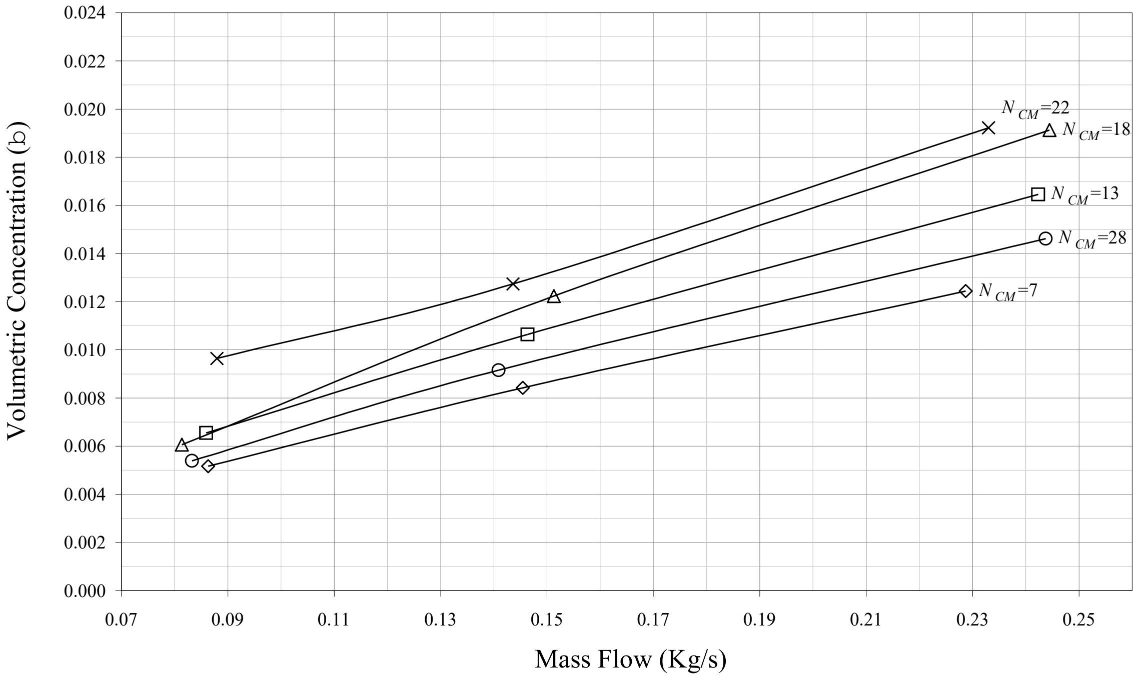

Figure 7.3 Mass Flow vs. Volumetric Concentration for Trial 2

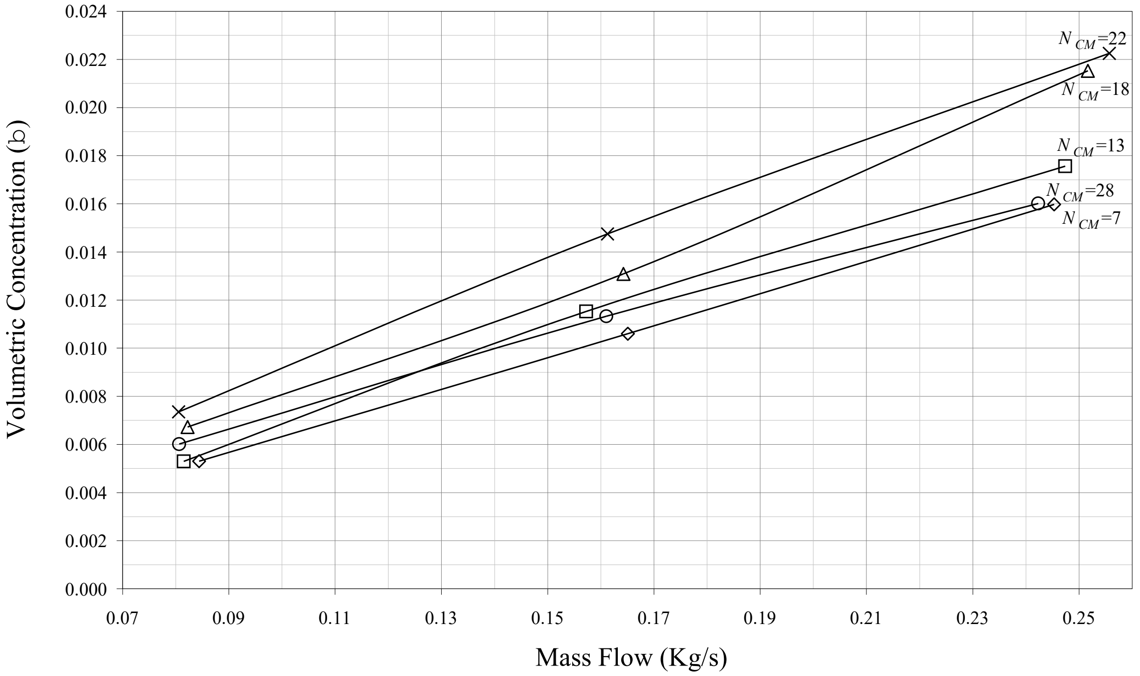

Figure 7.4 Mass Flow vs. Volumetric Concentration for Trial 3

From initial examination of the graphs shown in the above Figures 7.2 - 7.4, the following observations were made;

1. A linear relationship exists between the measured mass flow and the cross-sectional mean volumetric concentration which concurs with the work done by Young [4].
2. There is a widespread dispersal in the position of the graph contours corresponding to the number of measurements taken.
3. The position of the contours obtained for N_{CM} values of 7, 13 and, 28 measurements remain consistent between trials but the position of the contours obtained for N_{CM} values of 18 and 22 measurements regularly shifts position between each trial.

With the purpose of finding suitable explanation for the wide spread dispersal and the positional shift in the contours obtained, a second experiment performed. In this experiment, a cardboard divider was used to separate the sensor's pipe section into four separate areas (Figure 7.5).

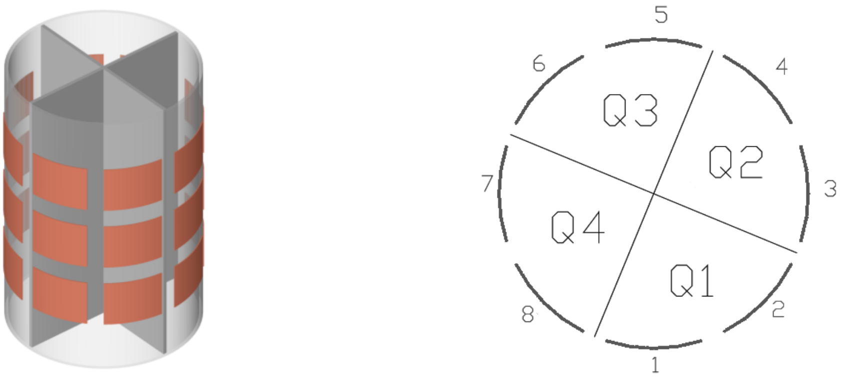

Figure 7.5 The ECT Sensor Divided Into Quadrants

The cardboard divider was arranged so quadrant one would span plates 1 & 2, quadrant two would span plates 3 & 4, quadrant three would span plates 5 & 6 and, quadrant four would span plates 7 & 8. Each quadrant of the calibrated sensor was filled with polypropylene pellets in turn whilst data was collected for N_{CM} values of 7, 13, 18, 22 and 28 measurements respectively. The results of which are shown in Figure 7.6.

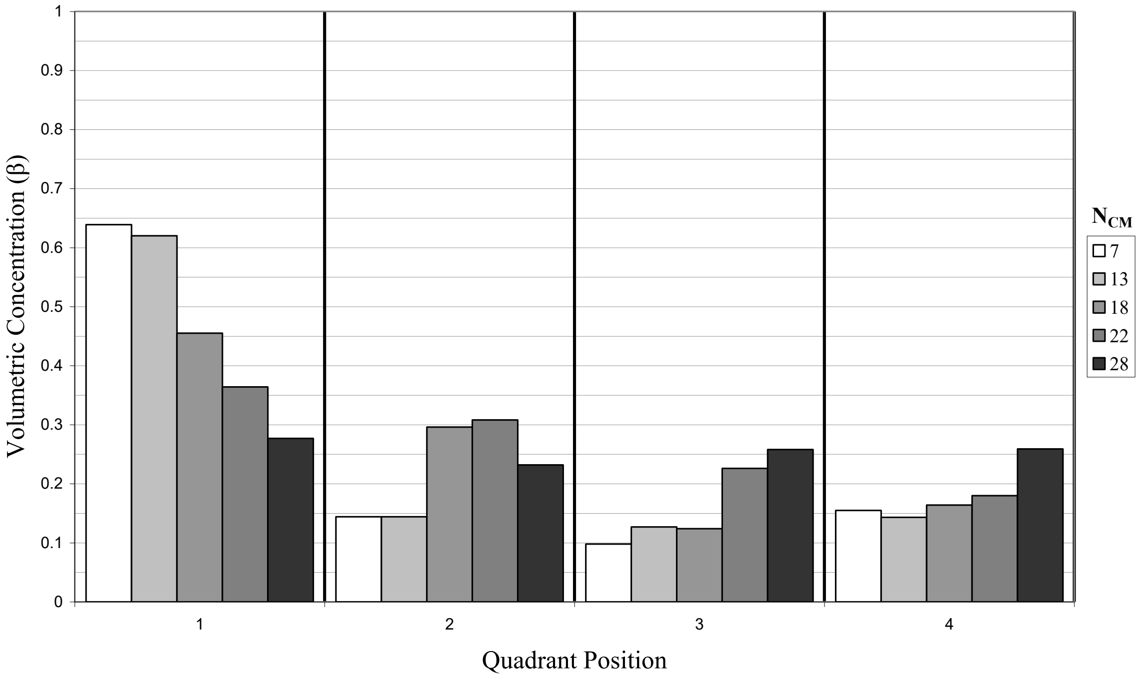

Figure 7.6 Measured Volumetric Concentration for all Four Quadrants

From Figure 7.6, the following observations were made;

1. The sum total of each individual volumetric concentration magnitude in each quadrant for a particular number of N_{CM} measurements is always equal to 1 (i.e. the equivalent of an undivided and filled sensor).
2. As the number of N_{CM} measurements taken is reduced, the magnitude of volumetric concentration is biased towards quadrant 1.
3. At $N_{CM} = 28$, the magnitude of volumetric concentration tends to even out across all quadrants.

Based on the above observations, the following assumptions can be made;

1. As the number of N_{CM} measurement taken from the ECT sensor is reduced, the resulting electrostatic field produced inside the sensor becomes more unevenly distributed. Hence the magnitude obtained relating to volumetric concentration becomes more solid object position dependant.
2. When the maximum number possible of measurements taken from the ECT sensor is taken (in this case $N_{CM} = 28$), the resulting electrostatic field produced inside the sensor is evenly distributed. Hence the magnitude obtained relating to volumetric concentration is independent of solid object position.

The validity of the above assumptions was tested further through the use of a LabVIEW based simulation program which was used to perform linear forward projection on predefined permittivity images mapped to the 812 normalised pixel permittivity grid (see Chapter 4, Section 4.2.2.2). From these predefined permittivity images, the program creates a series of cross-sectional mean volumetric concentration values (β) for each N_{CM} value of 7, 13, 18, 22 and 28 measurements respectively.

Two permittivity image sets were used; the first image set as shown in Figure 7.7, represents the four quadrant positions within the ECT sensor.

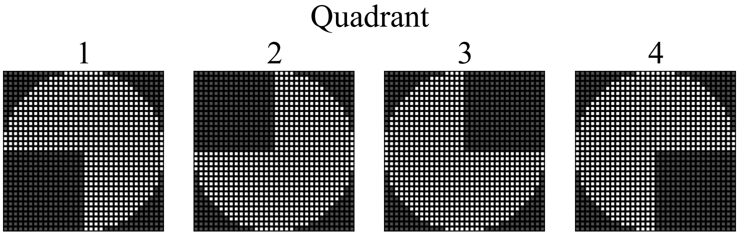

Figure 7.7 The Predefined Permittivity Images Corresponding to the Four Quadrant Positions within the ECT Sensor

The second set permittivity images used (Figure 7.8); represent increasing object densities located in the centre then in all four quadrants within the ECT sensor.

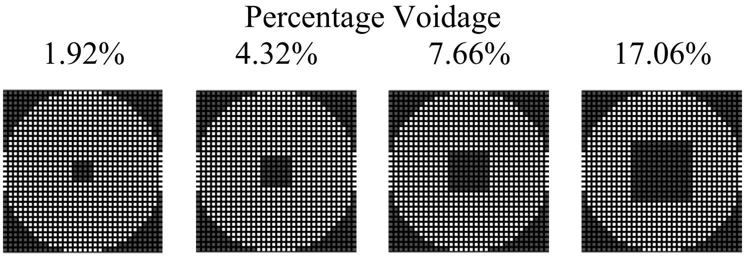

Centre

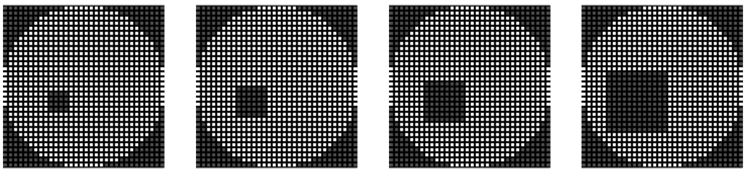

Quadrant 1

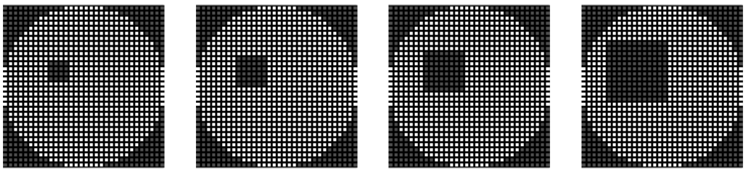

Quadrant 2

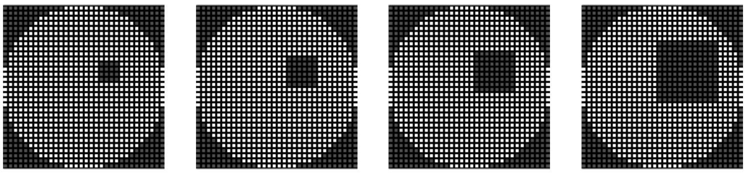

Quadrant 3

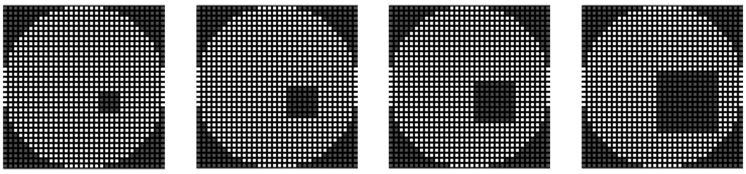

Quadrant 4

Figure 7.8 The Second Set of Predefined Permittivity Images Used for the Simulation

The first set of images as shown in Figure 7.7 is used to recreate the quadrant test as described above. The results obtained from this simulation are used to plot a bar graph similar to one shown in Figure 7.6 and is shown in Figure 7.9.

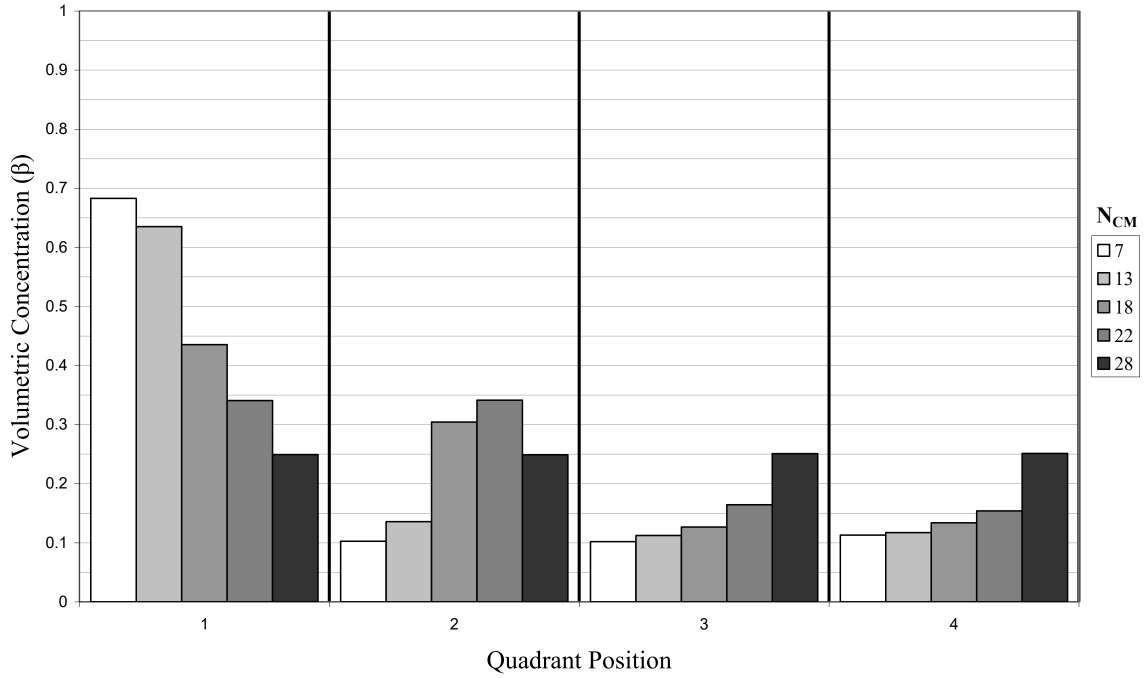

Figure 7.9 Simulated Volumetric Concentration for all Four Quadrants

Figure 7.10 shows the similarity between the the actual and the simulated results obtained for the cross-sectional mean volumetric concentration in each quadrant.

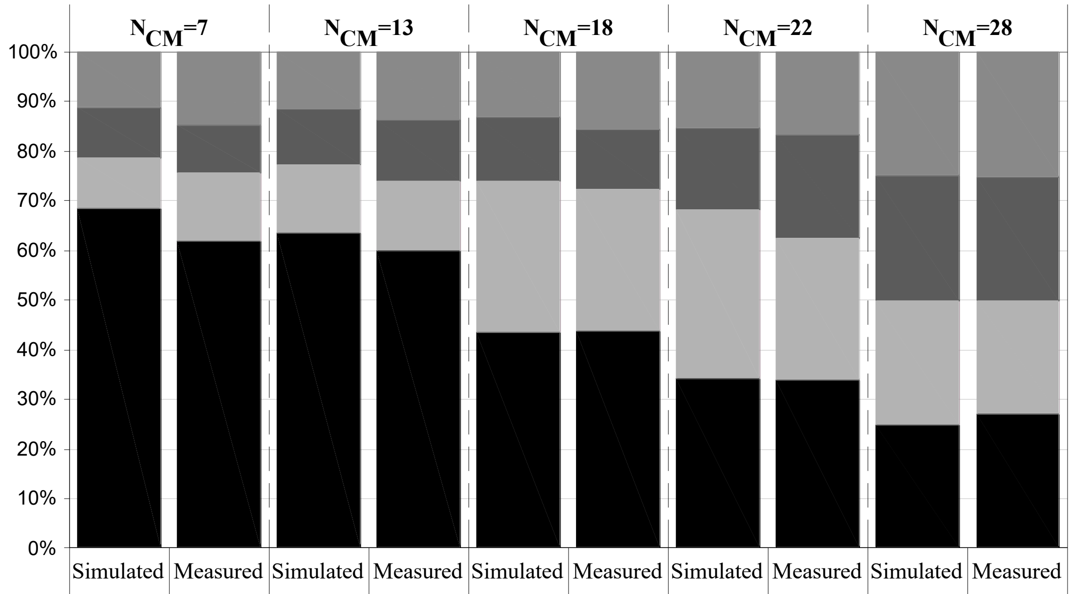

	Simulated	Measured	Simulated	Measured	Simulated	Measured	Simulated	Measured	Simulated	Measured
Quadrant 4	11.29%	14.96%	11.71%	13.83%	13.37%	15.78%	15.39%	16.70%	25.12%	25.24%
Quadrant 3	10.19%	9.46%	11.23%	12.28%	12.67%	11.93%	16.44%	20.96%	25.07%	25.15%
Quadrant 2	10.24%	13.90%	13.55%	13.93%	30.43%	28.49%	34.12%	28.57%	24.90%	22.61%
Quadrant 1	68.28%	61.68%	63.51%	59.96%	43.53%	43.79%	34.06%	33.77%	24.92%	27.00%

Figure 7.10 The Relative Contributions of Cross-Sectional Mean Volumetric Concentration Values of Each Quadrant as a Percentage of the Sum Total

Here, the simulated and measured data obtained from each quadrant for each value of independent averaged normalised capacitance measurements (N_{CM}) taken from the sensor is depicted as a stacked column chart, which compares the relative contribution of the cross-sectional mean volumetric concentration magnitudes of each quadrant as a percentage of the sum total of each individual volumetric concentration magnitudes.

The second set of images as shown in Figure 7.8, are used to generate a set data from which a series of contours showing percentage voidage (increasing mass) vs. the cross-sectional mean volumetric concentration for N_{CM} values of 7, 13, 18, 22 and 28 measurements respectively could be plotted. Also plotted, is the contour for an ideal position independent ECT sensor. For an ideal position independent ECT sensor the relationship between the percentage voidage and the mean volumetric concentration is given by Equation 7.1 where;

$$\beta_{Ideal} = 0.1 \times \%Voidage \qquad \textbf{Equation 7.1}$$

Figures 7.11, 7.12, 7.13, 7.14 and, 7.15 shows, graphs of the results obtained from the simulation based on the second image set compared to the ideal position independent contour (β_{Ideal}).

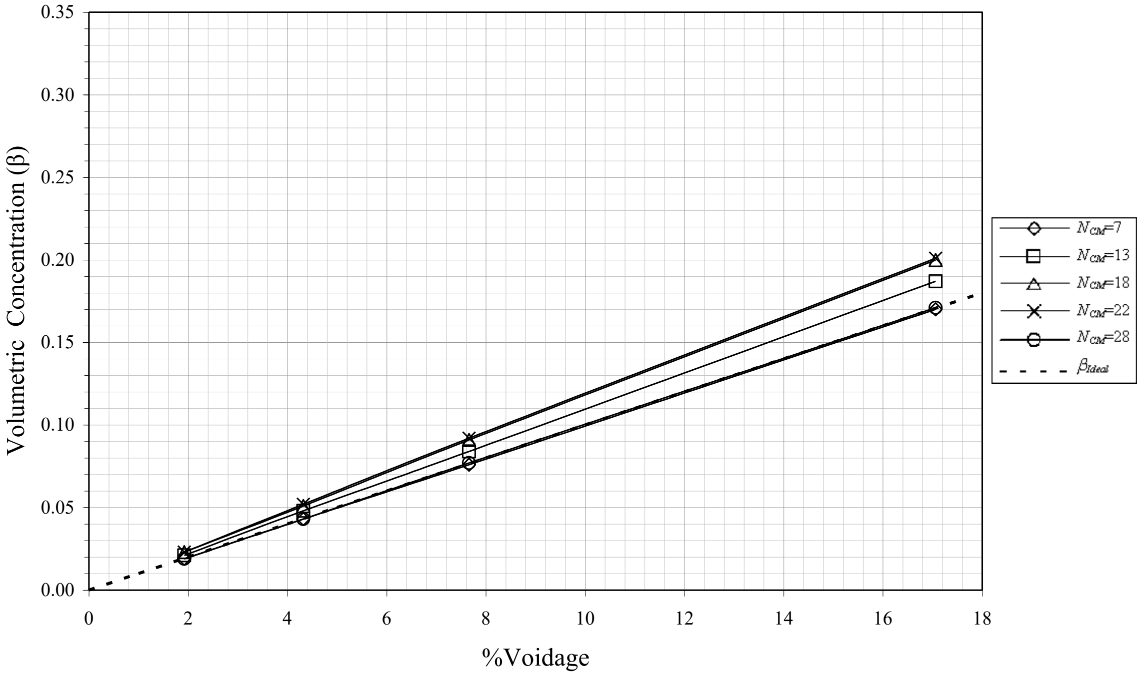

Figure 7.11 Simulation Result of Voidage vs. Volumetric Concentration for the Centre Position

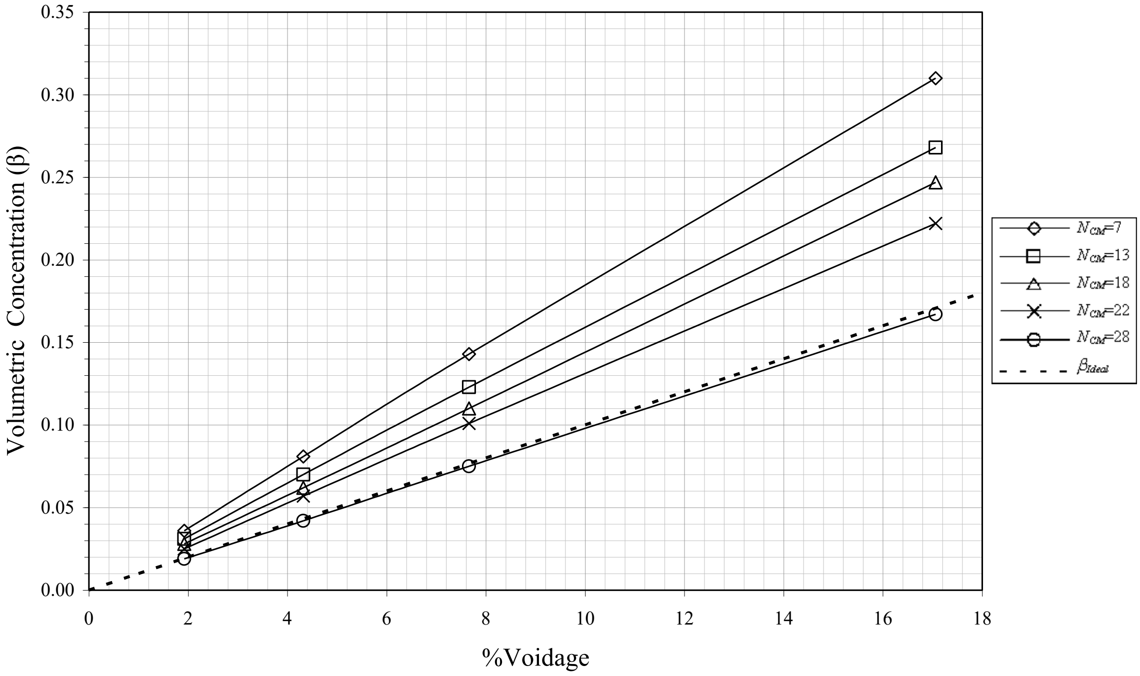

Figure 7.12 Simulation Result of Voidage vs. Volumetric Concentration for Quadrant 1

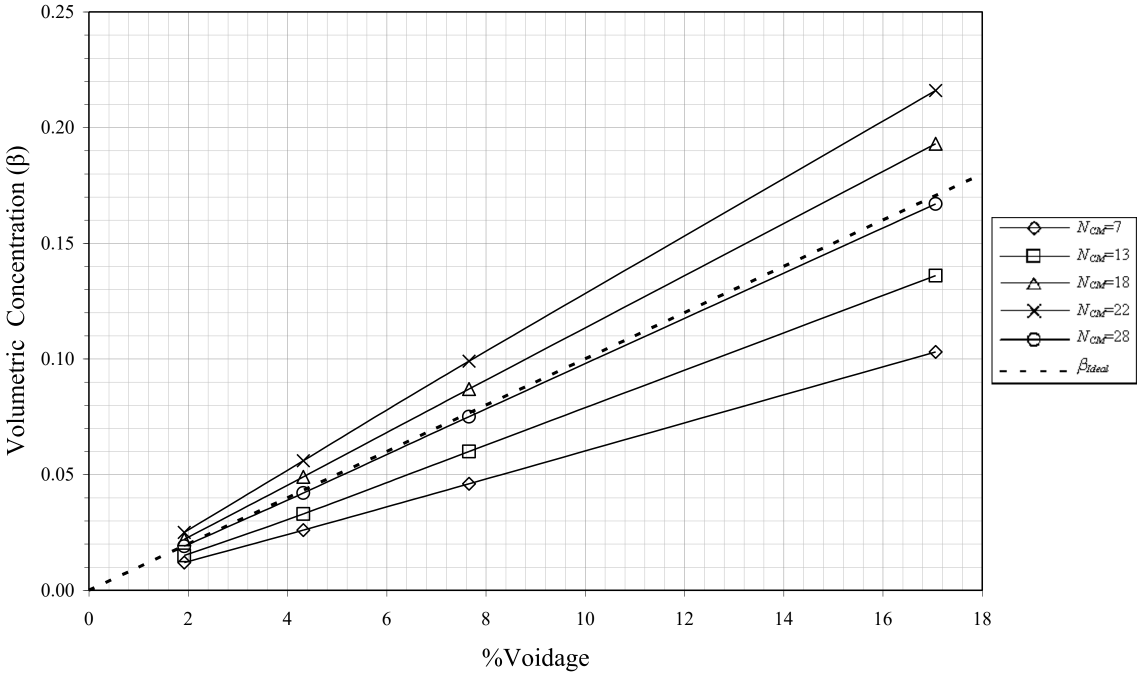

Figure 7.13 Simulation Result of Voidage vs. Volumetric Concentration for Quadrant 2

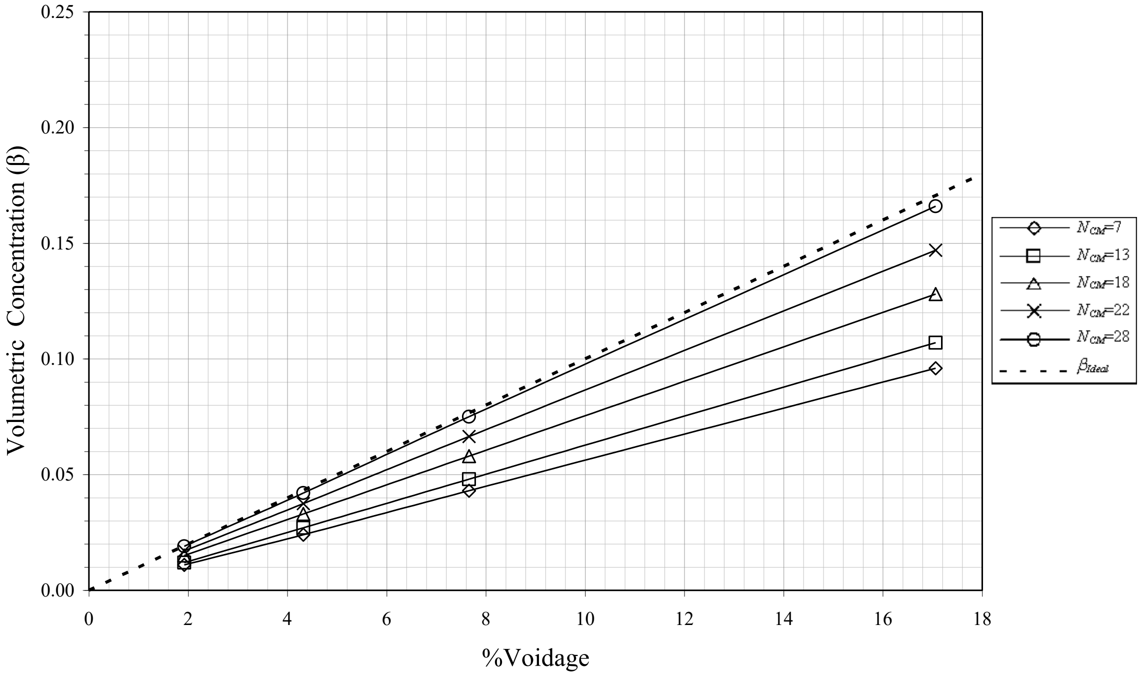

Figure 7.14 Simulation Result of Voidage vs. Volumetric Concentration for Quadrant 3

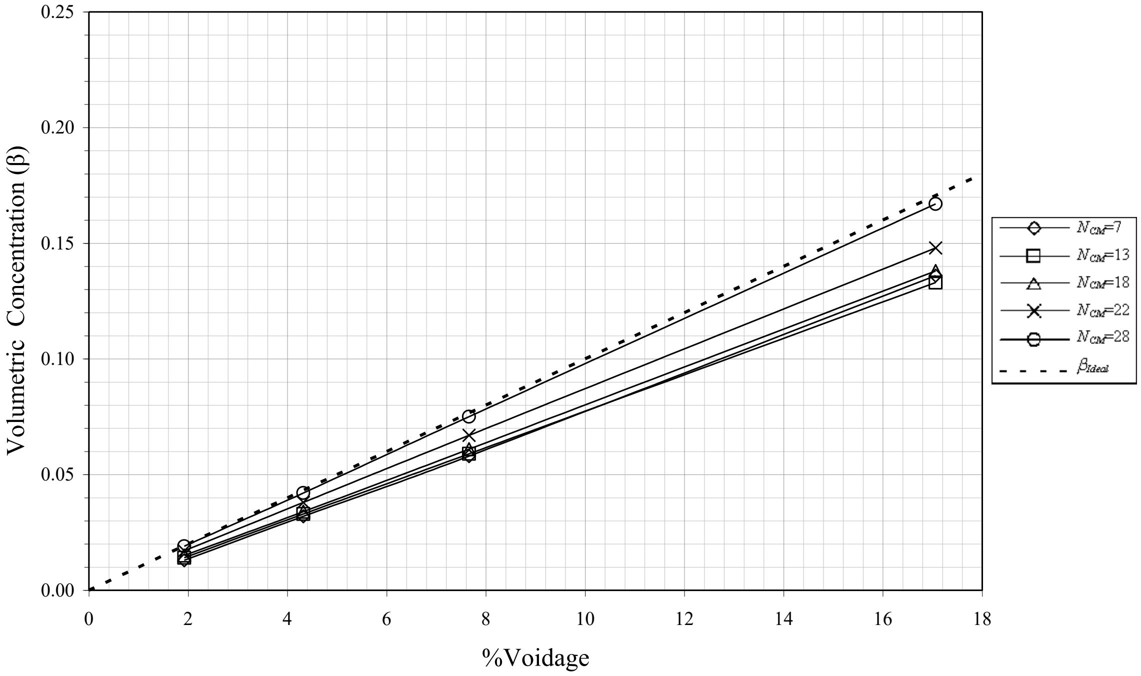

Figure 7.15 Simulation Result of Voidage vs. Volumetric Concentration for Quadrant 4

By examination of the graphs shown in the above Figures, the following observations can be made;

1. The relative positions of the contours corresponding to the number of measurements made can be successfully predicted by the use of the bar graph shown in Figure 7.9.
2. The contours obtained for N_{CM} values of 7, 13, 18 and, 22 measurements move significantly away from the ideal volumetric concentration contour as the simulated mass inside the sensor changes its position. It's only when $N_{CM} = 28$, that the measured contour converges towards the ideal volumetric concentration contour irrespective of the position of the simulated mass. This observation strongly indicates that only by taking all of the 28 average normalised capacitance measurements from the sensor, an accurate value for the mass flow rate can be obtained.

7.2.2 Pellet Velocity Measurement

The polypropylene pellet flow velocity (v) is calculated from the transit time (τ_d) of the pellets as they pass from the upstream ECT sensor to the downstream ECT sensor (See Chapter 3, Section 3.3). The transit time is obtained from the cross correlation of the averaged normalised capacitance values ($\overline{V_{NC}}$), taken from the upstream/downstream ECT sensors.

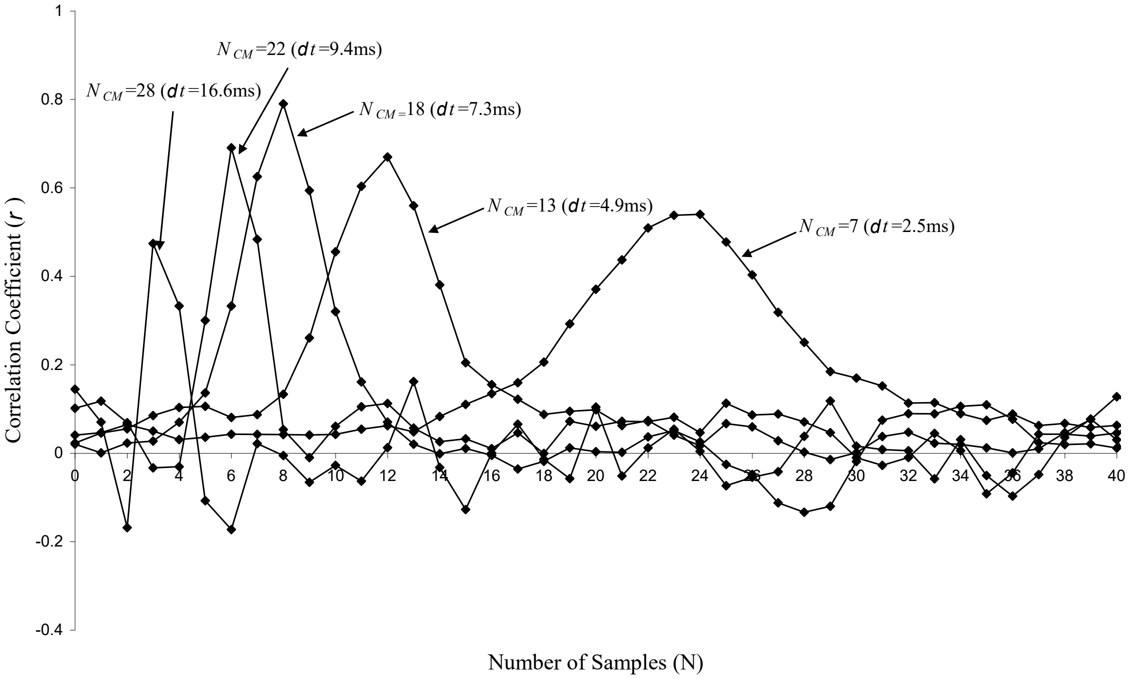

Figure 7.16 Comparison of Typical Correlograms Obtained for Independent Averaged Normalised Capacitance Measurements (N_{CM}) of 7, 13, 18, 22 and, 28

Figure 7.16 shows the resulting correlograms obtained for independent averaged normalised capacitance measurements (N_{CM}) of 7, 13, 18, 22 and, 28 measurements respectively. As it can be seen from Table 7.2, the sample interval (δt) is shortest when $N_{CM} = 7$ and longest when $N_{CM} = 28$. Figure 7.16 shows more N sample shifts when $N_{CM} = 7$ which decreases correspondingly as more measurements are taken from the sensor.

Number of Independent averaged normalised capacitance measurements (N_{CM})	**Sample Interval δt (ms)**	**Number of Sample Delays Corresponding to the Maximum Peak Position (m_d)**	**Transit Time τ_d (ms)**	**Pellet Velocity v (m/s)**	**%VDF $\left(\frac{100}{2m_d}\right)$**
7	2.5	23	58.5	3.3417	±2.17%
13	4.9	12	58.9	3.3183	±4.17%
18	7.3	8	58.6	3.3390	±6.25%
22	9.4	6	56.7	3.4494	±8.33%
28	16.6	3	49.9	3.9178	±16.67%

Table 7.2 Comparison of Transit Time Measurements (τ_d), Pellet Velocity (v) and, Velocity Discrimination Factor (VDF) Obtained for Independent averaged normalised capacitance measurements (N_{CM}) of 7, 13, 18, 22 and, 28

As Table 7.2 shows, the velocity discrimination factor (VDF) of the measured pellet velocity is smallest when only 7 measurements are taken from the sensor.

7.2.3 True Density of the Solids Material

As stated previously, $N_{CM} = 28$ measurements provide the most accurate measured quantity for the mean cross-sectional volumetric concentration. Based on this hypothesis, linear regression of the values taken for $N_{CM} = 28$ measurements, averaged over the three trials, should enable the actual relationship between mass flow and volumetric concentration to be determined empirically.

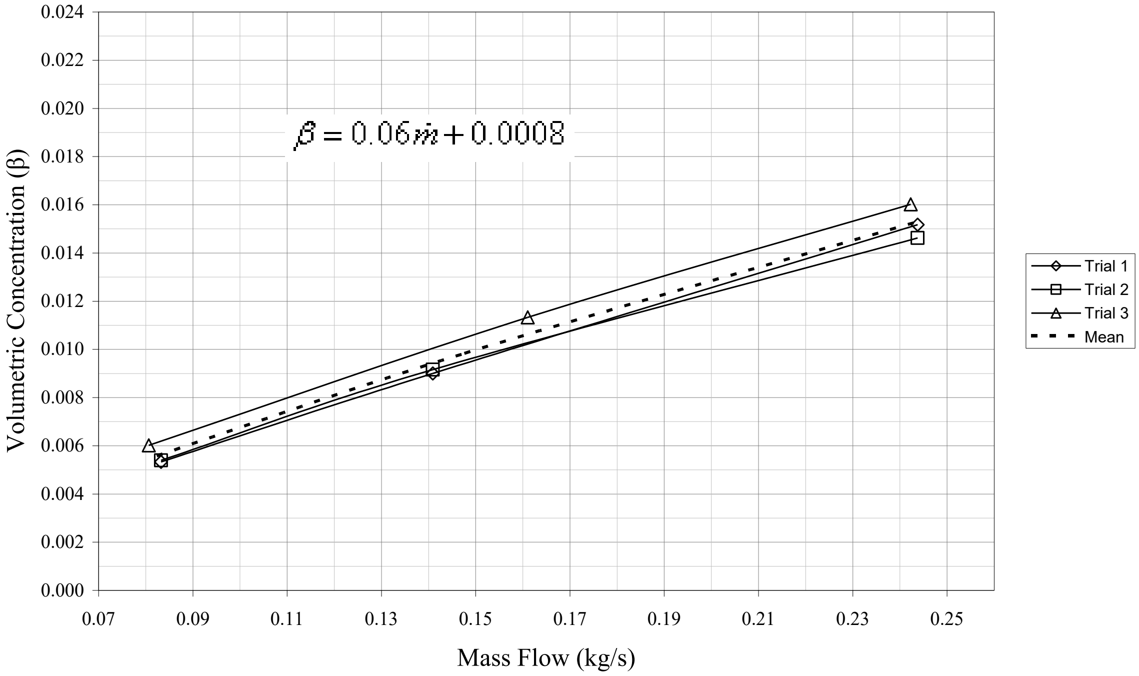

Figure 7.17 Mass Flow vs. Volumetric Concentration for $N_{CM} = 28$ Measurements (Averaged Over the Three Trials)

The result of this is depicted in Figure 7.17; analysis of this straight line graph gives Equation 7.2;

$$\beta = \dot{m}K_1 + K_2 \qquad \textbf{Equation 7.2}$$

Where:

$\dot{m}$ is the mass flow rate $\left(\frac{kg}{s}\right)$.

β is the cross-sectional mean volumetric concentration.

K_1 is a constant corresponding to the slope of the straight line graph as shown in Figure 7.17, and is equal to 0.06 $\frac{s}{kg}$.

K_2 is a dimensionless constant corresponding to the intercept of the straight line graph as shown in Figure 7.17, and is equal to 0.0008.

Rearranging Equation 7.2 to give mass flow in terms of volumetric concentration gives;

$$\dot{m} = \frac{\beta}{K_1} + \frac{K_2}{K_1}$$ **Equation 7.3**

Comparing Equation 7.3 with Equation 6.15 as given in Chapter 6, gives the mass flow in terms of the true density of the solids material (ρ),the solids velocity (v), the internal cross sectional area of the pipe that forms the ECT sensor (A), and the cross-sectional mean volumetric concentration (β). Here;

$$K_1 = \frac{1}{\rho v A}$$ **Equation 7.4**

Using Equation 7.4 to substitute for K_1 in Equation 7.3 gives;

$$\dot{m} = \rho v A(\beta + K_2)$$ **Equation 7.5**

The term K_2 in Equation 7.5, is probably due to a small DC voltage offset error introduced by the ECT measurement hardware system. For this reason, the K_2 term in the above equation can be effectively discarded providing it is sufficiently small (in this case 0.0008).

Equation 7.4 can be rearranged in order to find the true density of polypropylene pellets (ρ_{poly}) to give Equation 7.6.

$$\rho_{poly} = \frac{1}{K_1 v A}$$ **Equation 7.6**

As stated previously 7 measurements gives the most accurate measured quantity for transitional velocity, hence from Table 7.2;

$$v = 3.3417 \frac{m}{s}$$

and the internal cross sectional area of the ECT sensor vessel;

$$A = 69.398 cm^2$$

By using the above values in conjunction with Equation 7.6 gives a true density for the polypropylene pellets of;

$$\rho_{poly} = 0.626 \frac{gm}{cm^3}$$

The Shell measurement standard for polypropylene pellets is quoted as [23];

$$\rho_{poly} = 0.7 \frac{gm}{cm^3}$$

7.3 Conclusions

The results obtained show that as the number of average actual normalised capacitance measurements taken from the ECT sensor is reduced, the value obtained for cross-sectional mean volumetric concentration of the moving polypropylene pellets (β), is dependant on the position of the bulk of the flow within the plastic pipe. This is due to the fact that, for any number of average normalised capacitance measurements less than 28 will cause the electrostatic field generated within the ECT sensor to be concentrated in one area only (see Figure 7.18). Whereas, when 28 average normalised capacitance measurements are taken, the electrostatic field is distributed evenly throughout the sensor. As a result the value obtained for cross-sectional mean volumetric concentration, of the moving polypropylene pellets, consistent irrespective of the position of the bulk of the flow within the plastic pipe.

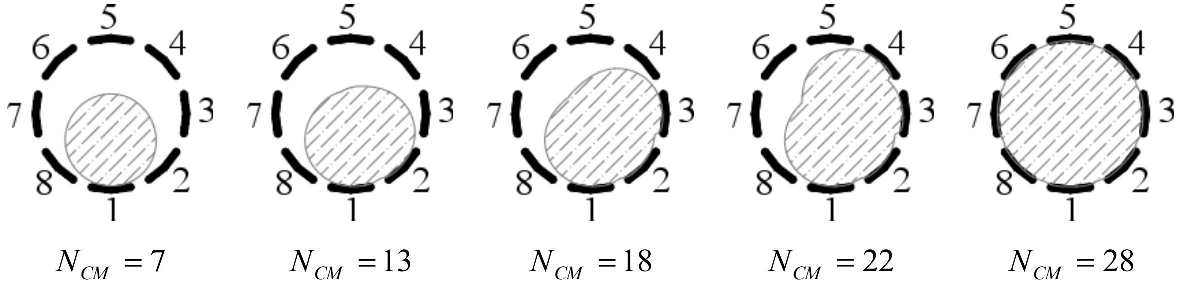

Figure 7.18 Qualitative Depiction of the Changes in the Electrostatic Field Generated Inside the ECT Sensor as the Number of Average Normalised Capacitance Measurements Taken Increases

Figure 7.19, shows one of the tomographic images taken from the upstream and downstream ECT sensors. As it can be seen, the bulk of the flow in the upstream sensor is noncircular and slightly off centre. The change in contour position for $N_{CM} = 18$ and $N_{CM} = 22$ average normalised capacitance measurements in Figures 7.2, 7.3 and, 7.4 could be attributed to outer perimeter perturbations of the flow profile.

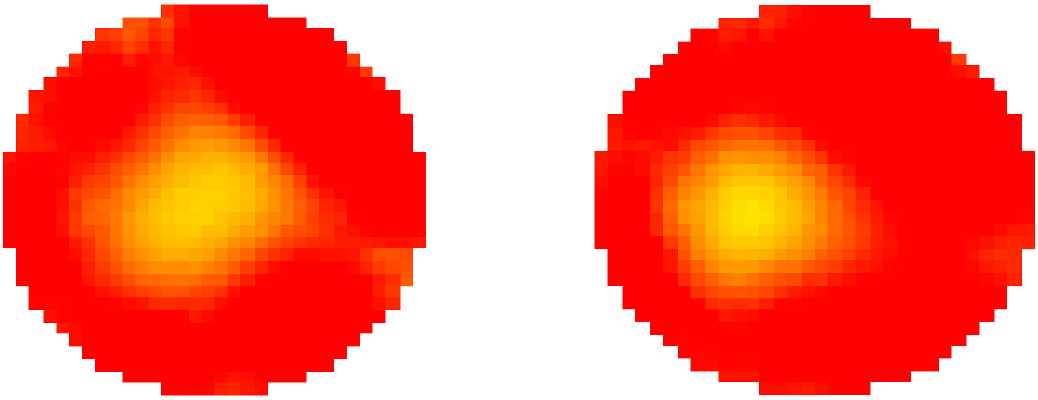

Upstream Downstream

Figure 7.19 Tomographic Images Taken from the Upstream and Downstream ECT Sensors

It is only when 28 average normalised capacitance measurements are taken from the ECT sensor that any practical relationship between volumetric concentration and mass flow can be assumed. In this case, this relationship is shown by Equation 7.7.

$$\dot{m} = 16.667\beta \frac{kg}{s} \qquad \textbf{Equation 7.7}$$

The measured pellet velocity's VDF is smallest, that is to say more accurate, when only 7 average normalised capacitance measurements are taken from the ECT sensor, which corresponds to the shortest sample interval of 2.5ms.

Chapter Eight

8 Conclusions and Future Work

8.1 Conclusions

The results obtained from the series of tests carried out on the MMU Virtual Instrument Measuring System confirmed that the solids volume concentration and consequently mass flow and flow velocity, can be derived from the data obtained for ECT imaging. Due to data acquisition time limitations introduced by the PXI system's hardware simultaneous accurate measurement of both mass flow and flow velocity cannot be successfully achieved with the existing system configuration.

Only when 28 average normalised capacitance measurements, corresponding to a data acquisition rate of 60 samples-per-second, were taken from the ECT sensor could an accurate determination for mass flow be achieved. Attempting to measure volumetric concentration with a measurement number of less than 28 will generate an inhomogeneous distribution of the electrostatic field within the sensor thus causing the sensor to become more flow position dependant. This consecutively produces an erroneous result in terms of mass flow measurement. Taking 28 average normalised capacitance measurements from the ECT sensor is analogous to the field rotation method which compensates for inhomogeneous field distributions.

The cross correlation measurement for flow velocity at 28 average normalised capacitance measurements, taken from the ECT sensor, produces a result with a high velocity discrimination factor ($\pm 16.67\%$). The most accurate measurement was achieved with 7 average normalised capacitance measurements taken from the ECT sensor, corresponding to a data acquisition rate of 400 samples-per-second, which gave a velocity discrimination factor of $\pm 2.17\%$.However when 7 average normalised capacitance measurements taken from the ECT sensor, it results in an inconclusive measurement in terms of the mass flow.

8.2 Future Work and Recommendations

8.2.1 Mass Flow Measurement

8.2.1.1 Modification to the MMU Flow Rig

Limitations in the MMU Flow rig mass flow measurement system meant that only a maximum value of 2.2% volumetric concentration was attained. Providing only three usable data points for the mass flow vs. volumetric concentration plots as given in Figures 7.2, 7.3 and, 7.4. A digital weighing scale with superior operational range (see Chapter 7, Section 7.2.1) would enable maximum mass flows corresponding to 25% - 50% volumetric concentration to be successfully achieved thus, giving a wider range of measured values.

8.2.1.2 Modifications to the Imaging Hardware and LabVIEW Software

One of the limitations of the current MMU Virtual Instrument Measuring System can be found with the hardware's parallel switching electronics (see Figure 5.6). At present, the system can only effectively drive and detect from single electrodes in a fixed sequence. Suitable modifications to the imaging hardware's parallel switching electronics and associated LabVIEW controlling software could enable the system to perform independent switching of the drive/detect electrodes of the ECT sensor. This would allow a wider range of electrode-pair configuration, measurements to be taken from the ECT sensor.

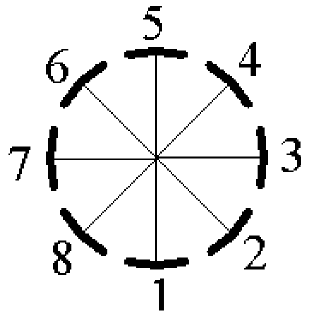

Measurement Step	Driven Electrode(s)	Detected Electrodes(s)
1	1,2,3,4	5,6,7,8

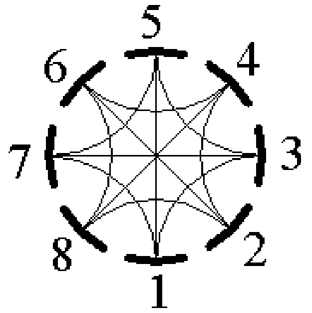

Measurement Step	Driven Electrode(s)	Detected Electrodes(s)
1	1	3,5,7
2	2	4,6,8
3	3	1,5,7
4	4	2,6,8
5	5	1,3,7
6	6	2,4,8
7	7	1,3,5
8	8	2,4,6

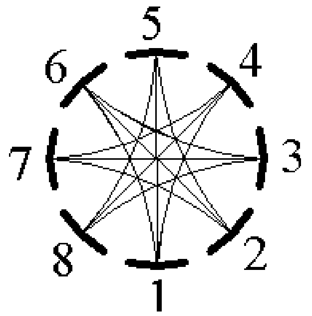

Measurement Step	Driven Electrode(s)	Detected Electrodes(s)
1	1	4,5,6
2	2	5,6,7
3	3	6,7,8
4	4	1,7,8
5	5	1,2,8
6	6	1,2,3
7	7	2,3,4
8	8	3,4,5

Figure 8.1 Examples of Possible Alternative Field Rotation Measurement Configurations

With this additional capability, complete rotation of the electric field could be achieved with fewer measurements as depicted in Figure 8.1. This would effectively increase the data acquisition rate whilst reducing flow regime dependency. This would improve the accuracy for simultaneous mass flow and flow velocity measurements.

This modification would also improve the system's tomographic imagining capabilities. The present system is capable of only implementing the protocol 1 (drive from a single electrode and detect from a single electrode). Improved image resolution can be achieved by increasing the number of joined electrodes used for drive and detect. Accordingly the protocol 2 measurement strategy would mean that four electrodes, joined as pairs, would be used as the drive and detect electrodes. The protocol number in fact, corresponds to the actual number of electrode pair groupings used and the total number of measurements M, for a given total number of electrodes N, in groups of P, is given by Equation 8.1 [30].

$$M = \frac{N(N-(2P-1))}{2} \qquad \textbf{Equation 8.1}$$

As it can be seen from the above equation, the total number of independent measurements generated will increase in proportion to the number electrode pair groupings employed. Image resolution therefore, can be improved but at the expense of total frame rate (data acquisition time).

8.2.2 Flow Velocity Measurement

8.2.2.1 Development of an Improved Flowmeter Virtual Instrument

Based on LabVIEW's cross correlation VI, an improved self contained flowmeter virtual instrument can be developed.

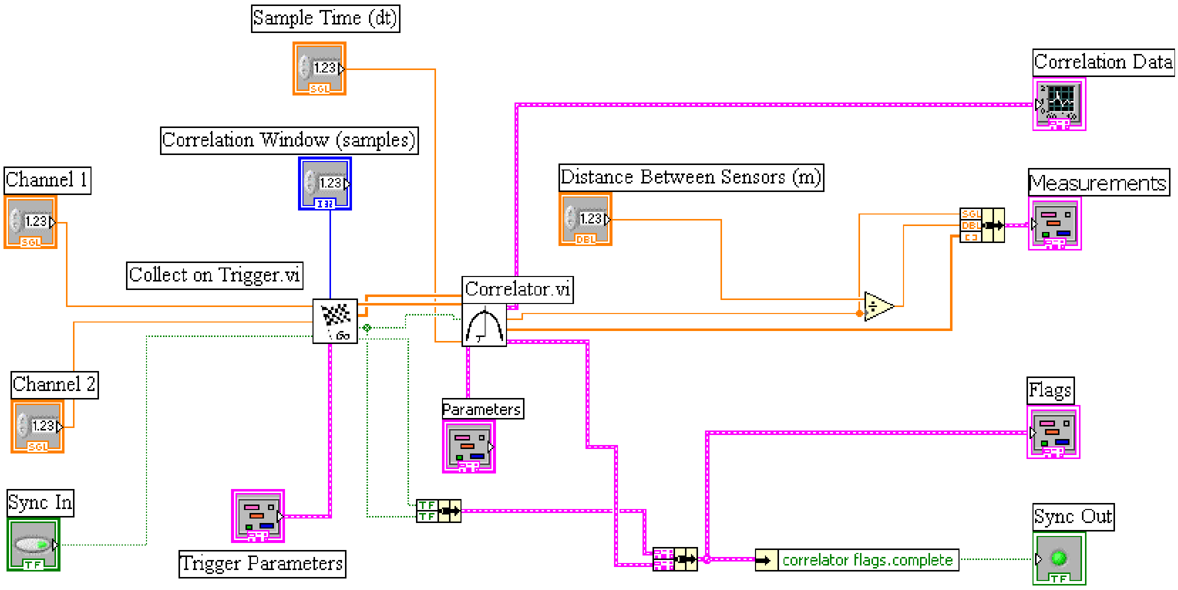

Figure 8.2 Proposed LabVIEW Flowmeter Virtual Instrument

An example of a proposed LabVIEW flowmeter is shown in Figure 8.2, which contains two main subVIs, the "Collect on Trigger" VI and the "Correlator" VI. The "Collect on Trigger" VI controls start and end of the cross correlation based on user defined trigger conditions of the input signals. Once triggered this VI starts to buffer the input data ready for cross correlation. The "Correlator" VI, besides performing a cross correlation of the two input signals, should also feature an ensemble averaging of the correlation data, a pre-delay to improve the time resolution for a limited correlation delay range and discrimination error reduction by the use of second order polynomial peak detection [58].

8.2.2.2 Single Plane Velocity Measurement

As stated in Chapter 3, Section 3.3, the measurement of pellet velocity by cross correlation requires the need for two suitable sensors spaced a fixed distance axially apart. A alternative technique proposed by Reinecke and Mewes [59] outlines a scheme which requires only one sensor in order to determine the average velocity of the total mass of an object passing the sensor over a fixed period of time. This method employs the axial extension in the x direction of the measurement volume of the ECT sensor to generate two signals from which the entry and exit time of an object as it passes through the sensor can be determined. Further research as to the practicability of this method would be required before a comparison to the cross correlation method could be made.

8.3 Contributions to Knowledge and Learning

The work in this thesis has contributed to knowledge in the following areas:

- That a proprietary based PXI industrial system running a modular virtual instrument measuring system based on the LabVIEW software platform can be successfully implemented as the core component used in the design and development of a highly flexible electrical capacitance tomographic imaging system.
- By exploiting the intrinsic modularity of the virtual instrument measuring system and by use of separate software modules a single function combined solids mass flow and solids velocity measuring systems has been developed from an ECT Tomographic imaging system.
- Measurement and simulation into the investigation of the reduction of the number measurements required in a mass flow/ velocity measuring system have shown it to be a function of mass flow position in the sensing area and of the maximum number of measurements taken.
- Shown that due to the limitations encountered with the current available hardware simultaneous and accurate measurement of solids mass flow and solids velocity could not be achieved.

8.4 Fulfilment of Objectives

The objectives of this work, as stated in section *xxxxx*, of this thesis have been met as follows:

1. The preceding MMU flow rig was modified to facilitate the study of material flow either as a pneumatically conveyed system in the horizontal plane or, a gravity conveyed system in the vertical plane.
2. Theoretical techniques for direct and inferential mass flow measurement using non-intrusive steady state capacitive sensors have been examined. Also, a practical capacitance based mass flow measurement system was presented.
3. Computational methods for finding the transit time delay and hence, the flow velocity, from the peak of the discrete cross correlation function has been presented. Measurement errors introduced by edge effect, correlation delay range time, signal bandwidth sensor spacing and velocity discrimination have also been examined.
4. A LabVIEW subVI was developed which post processes the collected averaged normalised capacitance data from the ECT system. The post processing procudure firstly, measures the flow velocity of the polypropylene pellets by cross correlation of the upstream and downstream, time delayed, random noise patterns taken from the two ECT sensors. Then secondly, determines the normalised mean volumetric concentration measured in the upstream ECT sensor. These two quantities are then used to infer the overall mass flow rate of the polypropylenes pellets.

Appendix A

PSPICE Simulation Results for the MMU ECT System’s Low Pass Filter

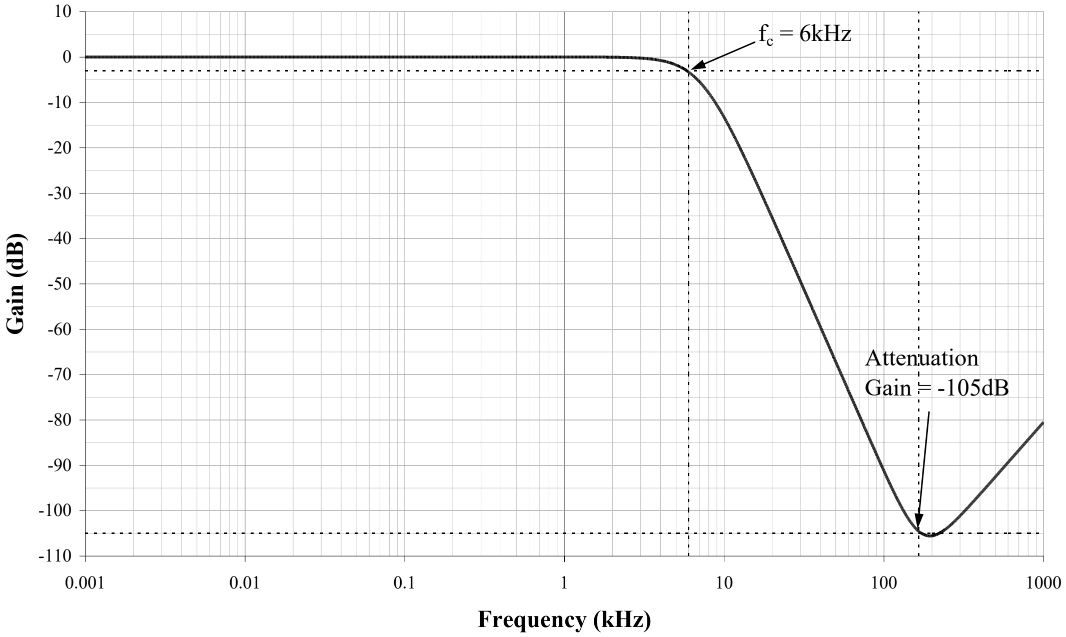

Figure A.1 PSPICE Simulated AC Magnitude Response of the 4th Order LPF

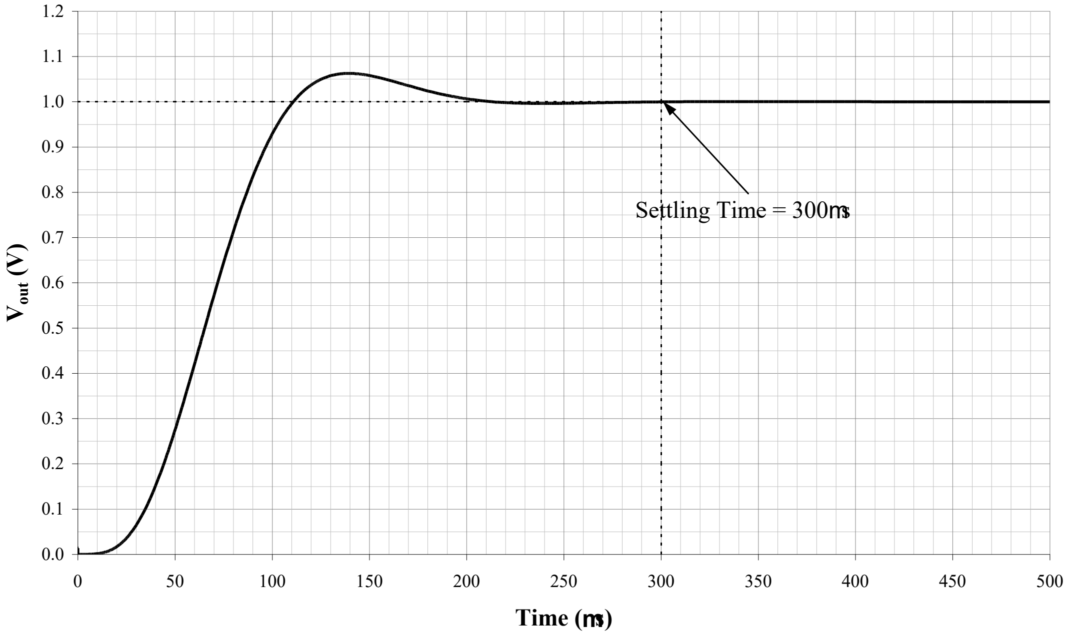

Figure A.2 PSPICE Simulated Transient Response of the 4th Order LPF

Appendix B

Derivation of Equation 6.17 in Chapter 6, Section 6.5.2.2

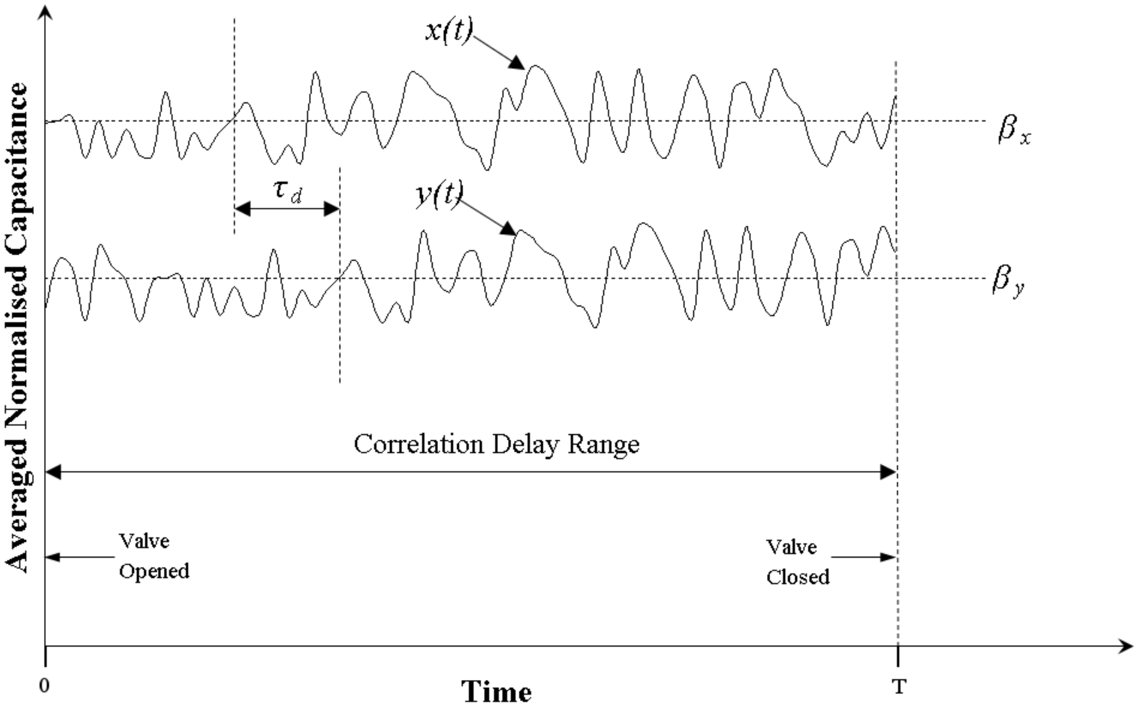

Figure B.1 Typical Averaged Normalised Capacitance Measurements ($\overline{V_N}$) Taken from the Upstream and Downstream ECT Sensors

The averaged normalised capacitances ($\overline{V}_{NCx}(t)$ and $\overline{V}_{NCy}(t)$) taken from the upstream and downstream ECT sensors (Figure B.1) can be represented by Equations B.1 and B.2.

$$\overline{V}_{NCx}(t) = x(t) + \beta_x$$ **Equation B.1**

$$\overline{V}_{NCy}(t) = y(t) + \beta_y$$ **Equation B.2**

Where:

$x(t)$ and $y(t)$ is the random noise patterns generated by the solids material as it passes through the upstream and downstream sensor respectively.

β_x and β_y is the mean volumetric concentration of the solids material in the upstream and downstream sensor respectively.

The cross correlation function of the upstream ($\overline{V}_{NCx}(t)$) and downstream ($\overline{V}_{NCy}$) signals is given by Equation B.3.

$$R_{xy}(\tau) = \lim_{T\to\infty} \frac{1}{T} \int_0^T \overline{V}_{N_x}(t)\, \overline{V}_{NCy}(t+\tau)\, dt$$ **Equation B.3**

By using Equations B.1 and B.2 to substitute for $\overline{V}_{NCx}(t)$ and $\overline{V}_{NCy}$ into Equation B.3 gives;

$$R_{xy}(\tau) = \lim_{T\to\infty} \frac{1}{T} \int_0^T [x(t) + \beta_x]\,[y(t+\tau) + \beta_y]\, dt$$ **Equation B.4**

Expansion of Equation B.4 produces;

$$R_{xy}(\tau) = \lim_{T\to\infty}\left[\frac{1}{T}\int_0^T x(t)\, y(t+\tau)\, dt + \frac{1}{T}\int_0^T x(t)\, \beta_y\ dt + \frac{1}{T}\int_0^T y(t+\tau)\, \beta_x\ dt + \frac{1}{T}\int_0^T \beta_x\ \beta_y\ dt\right]$$ **Equation B.5**

Since no correlation exists between ($x(t), \beta_y$) and ($y(t), \beta_x$);

$$\frac{1}{T}\int_0^T x(t)\beta_y\ dt = 0$$

and

$$\frac{1}{T}\int_0^T y(t+\tau)\beta_x\ dt = 0$$

Hence, Equation B.5 becomes;

$$R_{xy}(\tau) = \lim_{T\to\infty} \frac{1}{T}\left[\int_0^T x(t)\, y(t+\tau)\, dt + \int_0^T \beta_x\ \beta_y\ dt\right]$$ **Equation B.6**

Appendix C

Related Published Papers

Application of an Industrial Embedded Virtual Instrument System to Electrical Capacitance Tomographic Imaging

I. Ibrahim[1], R. Deloughry[1],

P.V.S Ponnapalli[1], P. Lingard[1] ,

D. Benchebra[1].

[1]*Department of Engineering and Technology, Manchester Metropolitan University. Manchester M15GD, UK. Email: i.ibrahim@mmu.ac.uk*

PROCTOM 2006

4th International Symposium on Process Tomography in Poland, Warsaw 14-15 September 2006

Application of an Industrial Embedded Virtual Instrument System to Electrical Capacitance Tomographic Imaging

I. Ibrahim[1], R. Deloughry[1],
P.V.S Ponnapalli[1], P. Lingard[1] ,
D. Benchebra[1].

[1]Department of Engineering and Technology, Manchester Metropolitan University.
Manchester M15GD, UK. Email: i.ibrahim@mmu.ac.uk

Summary: *The research program at MMU into a modular generic VI system is based on a National Instruments (NI) PXI 8186 Embedded Pentium Controller system and NI LabView Graphical programming software.The structure and design philosophy of the ECT Embedded VI, imaging system will be presented and the limitations/advantages of the system discussed. An evaluation of the system to the closed loop control of a pneumatic flow rig, using Neural Networks will be presented.*

Keywords: Virtual Instrument, LabVIEW, PXI, Process Tomography.

Introduction

For most tomographic imaging systems the required hardware and software is engineered for a specific process, and portability is limited, applying this to an industrial environment results in an expensive and lengthy development process for each application. Although the sensing hardware connected to the process may be application specific, the signal conditioning, timing control hardware, image reconstruction software and image display/user interface software can be designed using proprietary equipment and developed as a modular structure. As increases in processing capabilities of modern computers continue, migration of application specific hardware systems over to more generic platforms are becoming more popular. Major factors such as cost; reductions in production time and ease of modification are the reasons for this. Current tomographic imaging systems are based on application specific hardware used in conjunction with high level programming languages such as C++ and Matlab. A Virtual Instrument (VI) used for Process Tomography that is low cost and robust yet flexible incorporating proprietary hardware plug-in boards would be attractive in industrial applications. This study aims to analyse the application of Virtual Instrumentation, based on proprietary hardware, to Electrical Capacitance Tomography for use with process flow control.

Virtual Instrument System

The concept of a Virtual Instrument, comprising of a combination of hardware and/or software elements typically used with a PC, has seen rapid growth as computers become cheaper and more powerful. Advances in software capabilities have also contributed to this growth by allowing complex software systems to be built using relatively simple Graphical User Interfaces (GUI). Fast production and prototyping with ease of modification has made the VI favourable over traditional standalone instruments. Decreasing production costs of proprietary data acquisition (DAQ) hardware modules have also been a major contributor to the widespread use of VI’s in industrial applications

(National Instruments, 2005; Nair, 2006). The MMU Virtual Instrument Measuring System (VIMS) replaces the general purpose PC with a National Instruments PXI system, consisting of a Pentium 4 embedded controller and add-on propriety data acquisition hardware. It combines standard PCI and Compact-PCI technology with integrated timing and triggering to deliver a rugged platform with projected performance improvement over older architectures. The PXI instrumentation platform is a recognised industry standard for test measurement and automation (PXI Systems, Alliance 2004).

Virtual Instrument Software Architecture

VI systems share a common goal of acquiring, analyzing and presenting information (data) from a signal or sensors. The MMU Virtual Instrument Software Architecture (VISA) is implemented in LabVIEW, a graphical programming environment allowing a modular structure design to maximize interoperability between VI components adhering to the design concepts outlined previously (Deloughry, 2003, Davenport 2004). An overview of the Virtual Instrument Measuring System (VIMS) is shown in *Figure-1* highlighting key hardware and software components. The modular nature of Virtual Instrumentation allows 'plug-in' modules to be added for image processing and image analysis, such as Linear Back Projection (LBP), iterative LPB (P.T Ltd, 1999), Tikhonov and Landweber transforms (Byars 2001; Lionheart 2001; Liu, Fu et al. 2001; P.T Ltd 2005).

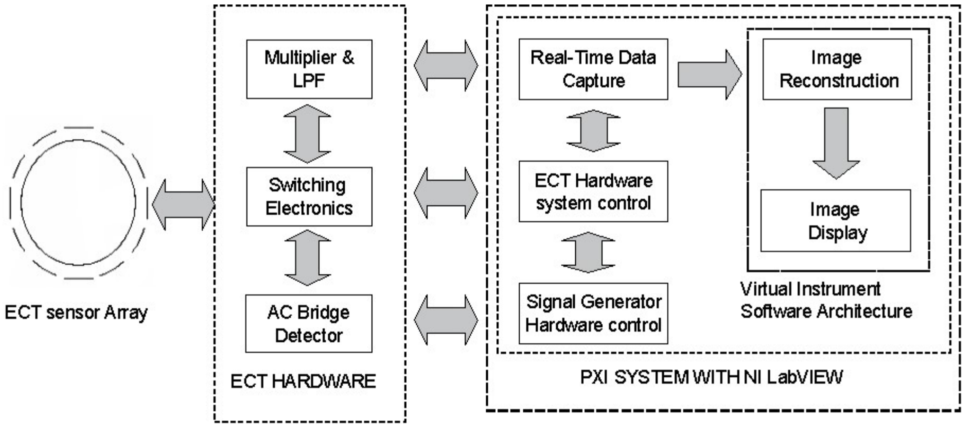

Figure-1. VIMS overview

The VI software consists of three main sections, a real-time data capture system, acquiring capacitance data via a PXI analogue input card, a hardware control system managing plate coupling and signal generation and an image reconstruction / display sub-system. . The generic nature of virtual instrumentation allows implementation of different sensing modalities (Deloughry, 2003) or ECT sensing systems, such as interchanging between an 8 and 12 electrode system or changing from AC-bridge to other capacitance detection techniques. The ECT hardware consists of an AC-bridge detector circuit operating at 100k Hz with signal routing, demodulation and low pass filtering hardware.

Application of the VIMS to Process Control

The MMU Virtual Instrument Measuring System (VIMS) was incorporated as part of a system to monitor and control the 'slugging' of polypropylene nibs in a pneumatic flow rig, *Figure-2*. The flow rig was operated in dilute phase flow conditions and the saltation/dune formation (Deloughry, 2001) of the Polypropylene nibs was controlled via the air flow rate. The nibs were allowed to build up in the flow rig and real time cross sectional images of the flow regime formed. *Figure-3* shows a series of tomograms of the dune formation of the nibs at the sensor position. The top row of the tomograms show the permittivity cross sections and the bottom row show occupied pixel area.

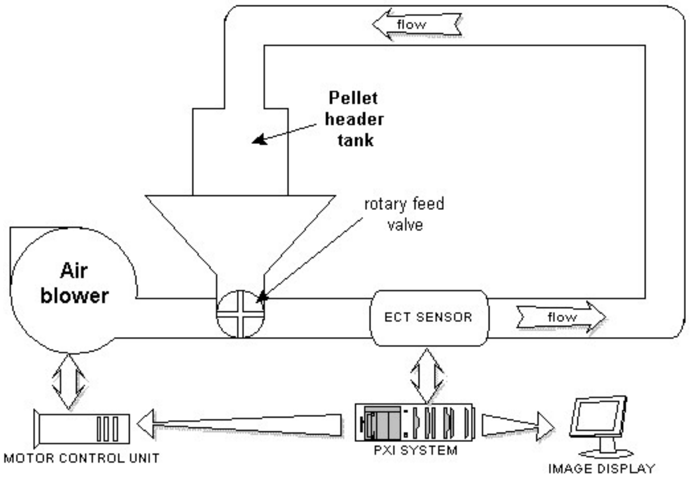

Figure-2. The MMU flow rig

The pixel area tomogram of the dune formation was used as part of the feedback control mechanism and incorporated in a Neural Network (NN) controller to control the flow rate of the air blower. The NN controller was compared to a conventional proportional integral controller which used the pixel area tomogram in its feedback path.

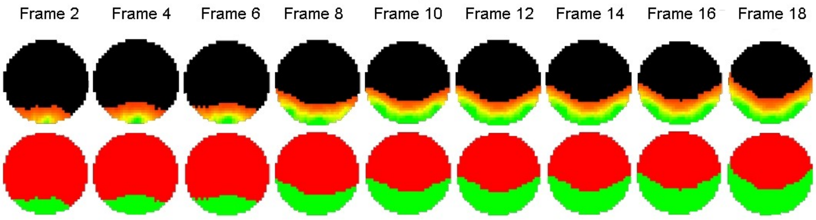

Figure-3. Tomograms showing pellet build-up

A plot of the number of non-zero pixels with each consecutive frame, Figure-4 confirms a steady build up pellets in the sensor region as the air speed in the rig decreases.

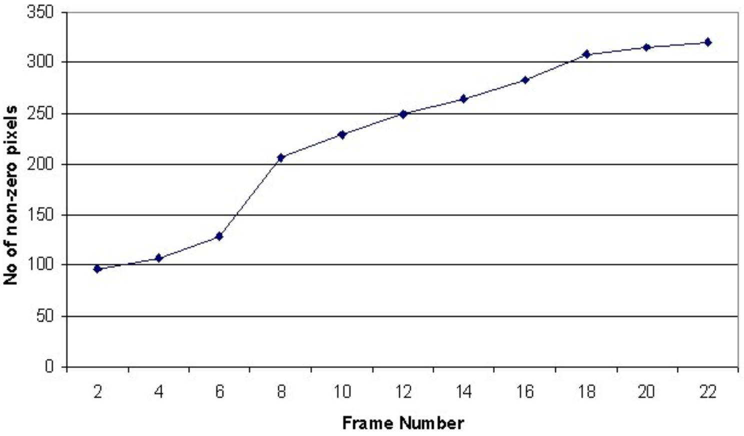

Figure-4. Plot of pixel count Vs frame number

The Neural Network Based Controller

The controller based on a Multi-Layer Perceptron (MLP) is implemented as shown in *Figure-5*. It consists of a set of sensors units which constitute the input layer, one or more hidden layers of variable numbers of neurons and an output layer. The input *d(t-n)* is the dune level measurement at the image *t-n*, *v(t-n)* represents the air flow speed at the time *t-n*, *c(t)* is the desired dune level and *k* the number of hidden nodes. Dune level measures from 9 previous permittivity images and 10 previous values of air control speeds are given as inputs to the perceptron in order to obtain the control value of air speed, *v(t),* to apply.

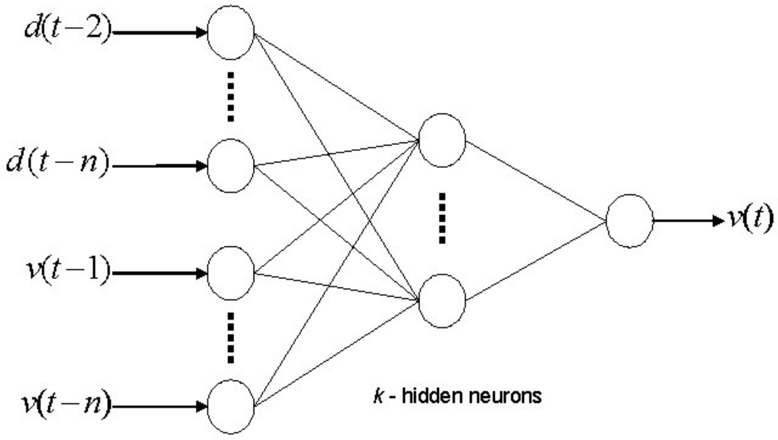

Figure-5. The MLP based NN controller

Benefits / Limitations of the VI Imaging System.

Virtual Instrumentation offers fast development compared to the design and production times of traditional standalone instruments. The graphical nature of LabVIEW with the use of proprietary ‘off the shelf’ hardware, enables the generation of complex measurement instruments. The hierarchical and modular nature of LabVIEW enables existing Virtual Instruments to be easily modified. The PXI system presents a rugged proprietary instrumentation platform designed for the industrial environment and by minimizing the external application specific hardware a system can be developed which is inherently more reliable. As Virtual instruments are generally PC based they have the ability to communicate to other systems via USB, Ethernet or the internet. Newer technologies such as WiFi and Bluetooth allow wireless communications which are suitable for industrial applications, a group of instruments would have the ability to share data or collectively be used as a single system, creating new possibilities for tomographic analysis. A major limitation in the use of VI for tomographic imaging is the maximum frame rate achievable due to the high number software threads the processor has to execute within a Windows based operating system. This restriction was as indicated by Davenport (Davenport 2004) and encountered by the current VI ECT system. The maximum achievable frame rate for any tomographic imaging system is limited by its hardware settling time and/or the execution time of the imaging algorithm. In the case of the VI the software/hardware setup time for excitation signal generation for each capacitance measurement is an additional limiting factor determining the maximum image frame rate. The frame rate is further decreased when other software applications, such as Matlab, are used with LabVIEW increasing the overhead on the embedded controller.

Future Work

Investigations in to the use of Field Programmable Gate Array (FPGA) systems in conjunction with ECT systems to produce faster more reliable imaging systems is to be conducted. The FPGA system would work with the current the PXI based virtual instrument and be used to analyse faster flow regimes allowing further flow rig behaviour model investigations. Current data acquisition hardware limitations rule out the possibility of a tomography system built entirely using proprietary hardware. Reductions in production costs could in the future give way to a tomographic image system with excitation signal routing, phase sensitive demodulation and low pass filtering implemented in software. An example of LabVIEW code which would perform such a function is given in *Figure-6.*

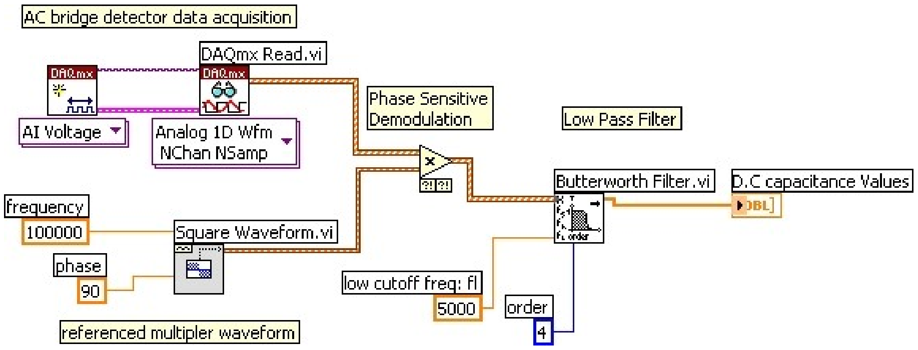

Figure-6. Signal conditioning in software

Implementation of the current VI on a non Windows based real time system, such as a National Instruments based RT controller, would provide deterministic performance and improve frame rate capability.

Conclusions

A Virtual Instrument incorporating a Tomographic system capable of imaging pneumatically conveyed pellets flowing in the MMU flow rig has been designed and built using LabVIEW software running on an embedded Pentium 4 PXI controller. This has resulted in a system which is independent of the standard PC platform and provides a robust system capable of use in an industrial environment. Advantages of using the PXI system include having an imaging system that uses proprietary interchangeable hardware enabling easy modification and provides a platform for executing powerful software applications using LabVIEW. The VI system was incorporated into a Neural Network controller and showed that the dune level in a pneumatic flow rig could be controlled. Due to the Windows operating environment and the Graphical programming structure it was not possible to obtain high frame rates for tomographic imaging. For applications where fast frame rates are not critcal but design flexibilty and low develpoment costs are required the VIMS system has shown distinct advantages.

References

Byars, M., (2001), Developments in Electrical Capacitance Tomography, 2nd World Congress on Industrial Process Tomography, 542-549

Deloughry, R., (2003), Development of a Virtual Instrument System for Industrial Process Tomography, 3rd World Congress on Industrial Process Tomography, 756-760

Deloughry, R, Pickup, E., (2001), Investigation of the closed loop control of a pneumatic conveying system using tomographic imaging, SPIE Vol 4188, 103-113

Davenport, I., (2004), A Virtual Instrument System for Tomographic Imaging, M.Sc., MMU

Lionheart, B., (2001), Reconstruction Algorithms for Permittivity and Conductivity Imaging, 2nd World Congress on Industrial Process Tomography, 4-11

Nair, C., (2006), Virtual Instrumentation for user-defined measurement, National Instrument Corp (Electronic Engineering Times: Asia)

National Instruments (2005), NI Developer Zone: Virtual Instrument, National instruments

P.T Ltd (1999), An iterative method for improving ECT images, Application Note: AN4(2)

P.T Ltd (2005), Matlab programs for ECT, (2.0)

PXI Systems Alliance, (2004), PXI Hardware Specification Rev. 2.2, PXISA

Liu, S., Fu, L., et al, (2001), Comparison of Three Image Reconstruction Algorithms for Electrical Capacitance Tomography, 2nd World Congress on Industrial Process Tomography, 29-34

PXI-Based Electrical Capacitance Tomographic Imaging System Applied to Flow Control and Mass Flow Measurement

R. Deloughry, I. Ibrahim, P.V.S Ponnapalli, P. Lingard,
D. Benchebra

Department of Engineering and Technology, Manchester Metropolitan University,

Manchester M15GD, UK, Email: r.deloughry@mmu.ac.uk

5th World Congress on Industrial Process Tomography, Bergen, Norway

2007

PXI-Based Electrical Capacitance Tomographic Imaging System Applied to Flow Control and Mass Flow Measurement

R. Deloughry, I. Ibrahim, P.V.S Ponnapalli, P. Lingard, D. Benchebra

Department of Engineering and Technology, Manchester Metropolitan University,
Manchester M15GD, UK, Email: r.deloughry@mmu.ac.uk

Typical ECT systems for use in industrial applications were based on dedicated hardware, such as the Texas Instrument C40 parallel processing system developed at MMU for measurement of large scale loading of road tankers. The industrial application indicated that a robust proprietary ECT system would be advantageous. The research program at MMU into a modular generic Virtual Instrument Tomographic imaging systems is based on a National Instruments (NI) PXI 8186 Embedded Pentium Controller system and NI LabView Graphical programming software. This has enabled a move towards using robust industry based proprietary equipment. Dual 8 and 12 electrode serial and parallel imaging systems have been developed and applied to control the flow of plastic pellets in a pneumatic flow rig using Neural Networks techniques. Axially spaced sensing arrays have been developed to enable the system to be used to measure the mass flow of pellets. The structure, design philosophy and limitations of the systems will be discussed and the results of the flow control application presented.

Keywords Process Tomography, ECT, LabView, PXI, Neural Network, Mass Flow

1 INTRODUCTION

The application of a tomographic imaging system to a specific industrial environment can result in an expensive and lengthy development process. Although the sensing hardware connected to the process may be application specific, the signal conditioning, timing control hardware, image reconstruction software and image display/user interface software can be designed using proprietary equipment and developed as a modular structure. Factors such as cost, reductions in production time and ease of modification are the reasons for this transfer from application specific hardware systems over to more generic platforms. Current tomographic imaging systems are based on application specific hardware used in conjunction with high level programming languages such as C++ and Matlab. A Virtual Instrument (VI) used for Process Tomography that is low cost and robust yet flexible incorporating proprietary hardware plug-in boards would be attractive in industrial applications.

The flow of pneumatically conveyed solids is a complex phenomenon which depends on many different flow conditions. Flow regimes that occur within a pneumatically conveyed system can be summarised by the phase diagram shown in Figure 1. If the solids mass flow rate is constant and the air velocity is reduced a point will be reached where there is an abrupt change from dilute to dense phase flow. In a horizontal pipe the transition from dilute to dense phase flow, for a constant mass flow, is the saltation velocity resulting in particles forming a layer on the base of the conveying pipe (Butterworth 1981, Deloughry 2000). The sudden transition between dense and dilute phase flow denotes a non-linear relationship between the air velocity input to the conveying system and the flow regime to be imaged, which presents a problem when attempting to control the flow in the pneumatic conveying system.

The paper aims to analyse the application of a proprietary based PXI National Instruments Virtual Instrumentation equipment configuration applied to an Electrical Capacitance Tomography (ECT) system. The system measures the mass flow of the pellets and provides data to a Neural Network controller for real-time control. Results obtained from the various imaging system configurations will be presented.

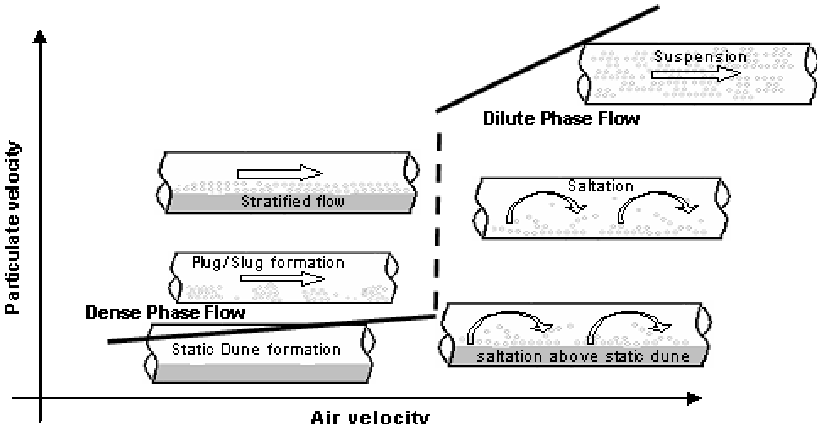

Figure 1. Schematic of phase diagram for pneumatic conveying

2 VIRTUAL INSTRUMENT SYSTEM

Santori (Santori, 1990) defines a virtual instrument as "an instrument whose general function and capabilities are determined in software". The concept of a Virtual Instrument (VI), comprising of a combination of hardware and/or software elements typically used with a PC, has seen rapid growth as computers become cheaper and more powerful. Advances in software capabilities and decreasing production costs of proprietary data acquisition (DAQ) hardware modules have contributed to the growth of Virtual Instrumentation allowing complex hardware/software systems to be built using relatively simple Graphical User Interface (GUI) based programming languages such as LabView and DAQBench (National Instruments, 2005, Nair, 2006).

The MMU VI ECT system replaces the general purpose PC with a National Instruments PXI instrumentation platform consisting of a Pentium 4 embedded controller and add-on propriety data acquisition hardware. The MMU Virtual Instrument Software Architecture (VISA) is implemented in LabView, a graphical programming environment allowing a modular structure design to maximize interoperability between VI components adhering to the design concepts outlined previously (Deloughry, 2003, Davenport 2004). An overview of the Virtual Instrument Measuring System (VIMS) is shown in Figure 2 highlighting key hardware and software components.

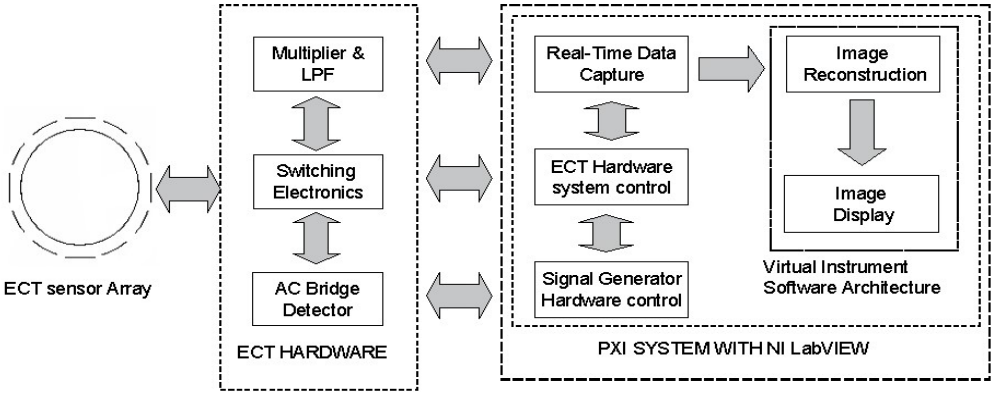

Figure 2. VIMS overview

Initial development of a VI based ECT system led to a serial capacitance data acquisition system generating 5 frames of permittivity images/sec. Although for some applications fast frame rates are not required further investigations indicated the need for a faster imaging system that would allow more accurate investigations into flow regime behaviour. The VI software consists of three main sections, a real-time data capture system, acquiring capacitance data via a PXI analogue input card, a hardware control system managing plate coupling and signal generation, and an image reconstruction/display sub-system. The generic nature of virtual instrumentation allows implementation of different sensing modalities (Deloughry, 2003) or ECT detection techniques. The current capacitance detection hardware consists of an AC-bridge detector circuit operating at 100k Hz with signal routing, demodulation and low pass filtering hardware.

The imaging frame rates achieved for the various configurations for the parallel sensing configuration are shown in table 1. For the serial configured system the measured frame rate was 5 frames/sec and this was found to be acceptable for the NN control application.

Sensing plate configuration	**Frame rate**
Single 8 plate sensing array	100 frames/sec
Dual 8 plate sensing array	66 frames/sec
Single 12 plate sensing array	40 frames/sec

Table 1 Parallel Sensing configurations and frame rates

3 THE NEURAL NETWORK BASED CONTROLLER

The Virtual Instrument Measuring System (VIMS) was used in conjunction with another research project working on NN-based controllers for real-time control using ECT. This also served as a validation tool for the VIMS. The architecture of the NN controller implemented was based on a Multi-Layer Perceptron (MLP) as shown in Figure *3*. It consists of a set of dune levels (inferred using the VIMS) that constitute the input layer, one hidden layer and an output layer having applied voltage to the air blower as output. The model used is an inverse model of the flow rig. The input $d(t-n)$ is the dune level measurement at the image $t-n$, $v(t-n)$ represents the air flow speed at the time $t-n$, $c(t)$ is the desired dune level and k is the number of hidden nodes. Dune level measurements from 9 previous permittivity images and 10 previous values of air control speeds are given as inputs to the NN in order to obtain the control value of air speed, *v(t),* which is applied to the motor.

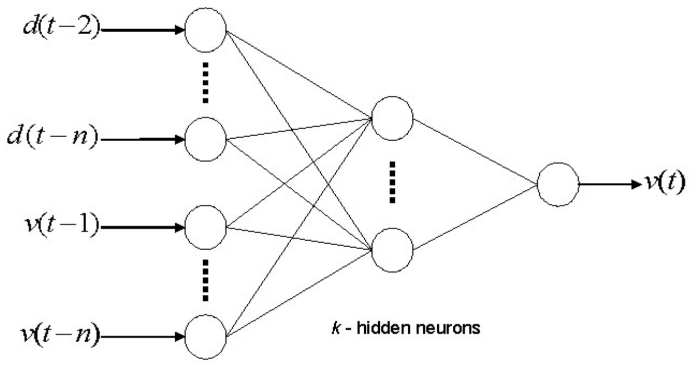

Figure 3. The MLP based NN controller

4 APPLICATION OF THE VIMS TO PROCESS CONTROL

The MMU Virtual Instrument Measuring System (VIMS) was incorporated as part of a system to monitor and control the 'slugging' of polypropylene pellets in a pneumatic flow rig, Figure 4. The flow rig was operated in dilute phase flow conditions and the saltation/dune formation (Deloughry, 2000) of the Polypropylene pellets was controlled via the air flow rate. The flow rig also incorporated a pellet diverter valve allowing a second pellet header tank to be used for mass flow measurement. Power measurements for the 1.5KW three phase induction motor driven air blower were taken using a Voltech™ PM3000 power analyser. The pixel area tomogram of the dune formation was used as part of the feedback control mechanism and incorporated in a Neural Network (NN) controller to control the flow rate of the air blower. The NN controller was compared to a conventional proportional integral controller which performed the same function as the NN controller.

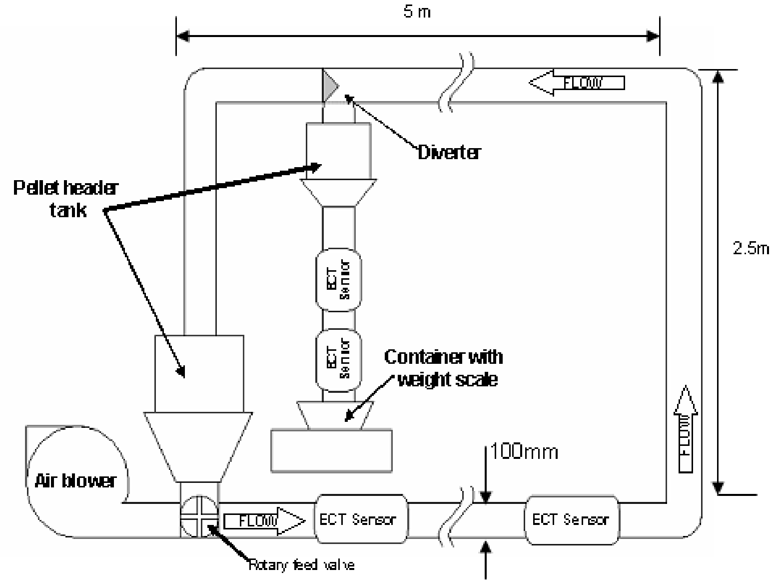

Figure4. The MMU pneumatic conveying flow rig

Initial application of the serial imaging system with NN controller indicated that for controlling dune build up a fast imaging frame rate is not essential, as the formations were either static or slow moving. However when disturbances in the form of an increase in mass flow rate were introduced there was an increase in the likelihood of a flow blockage. This may be due to the slow imaging frame rate given by the serial acquisition system meaning the NN controller was not able to react in time. The faster parallel VI ECT system enables imaging of higher speed plug/slug formation which when used with the NN controller diminished the chances of any blockages occurring. Figure 5 and 6 show the results from application of the NN controller for a fixed mass flow rate of 0.13kgs^{-1}

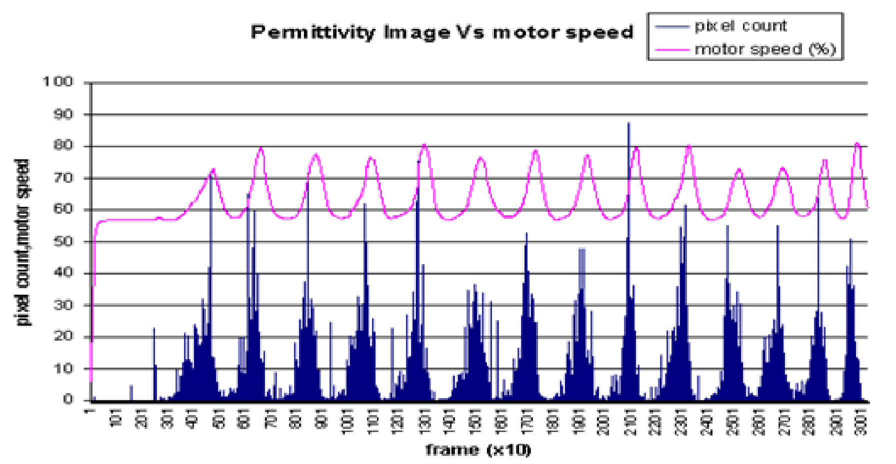

Figure 5. Sustained clearance of dune formation at saltation velocity, NN controller results

In Figure 5 the dune formation due to the saltation velocity being reached is represented in terms of the tomographic image pixel count. The NN controller motor speed is also shown providing successful clearance of dune formation indicated by a decrease in pixel count this cycle continued is over a sustained period validating successful dune level control.

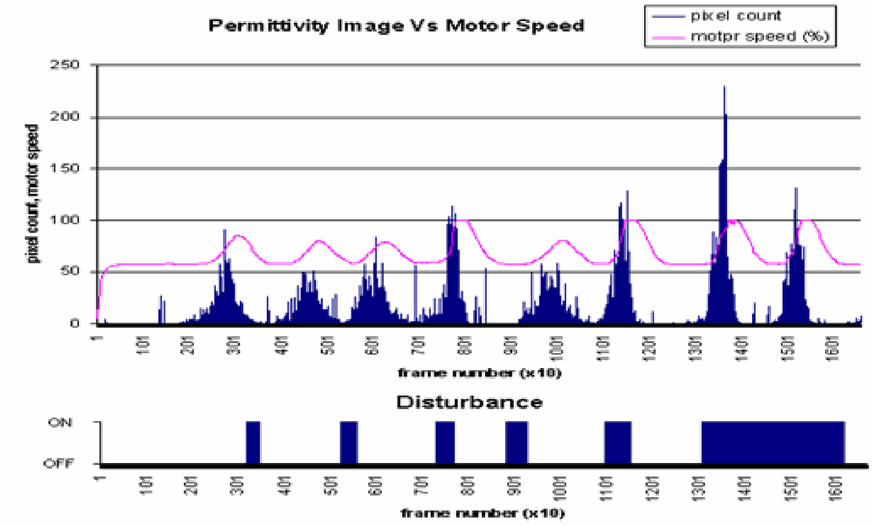

Figure 6. Neural Network controller results with 5% disturbance introduced to the mass flow rate

The introduction of controlled 5% mass flow disturbances (Figure 6) at random time intervals and periods showed that the NN controller was able to control the dune formation, though higher motor speeds were required to prevent dune formation compared to the sustained dune formation during saltation. The non linearity of the flow rig and complex system dynamics does not enable direct correlation with the disturbance and the peak of dune formation.

Two axially spaced capacitance sensing arrays, 20cm apart, were used to determine the mass flow of the plastic pellets by cross correlating (Beck, 1987) the normalised average capacitance values from the sensing arrays Figure 7 and 8. The pellets discharged from the pellet header tank reached terminal velocity (Edgar, 1989) and initial results show a linear relationship between the normalised average capacitance and the measured mass flow as shown in Figure 9.

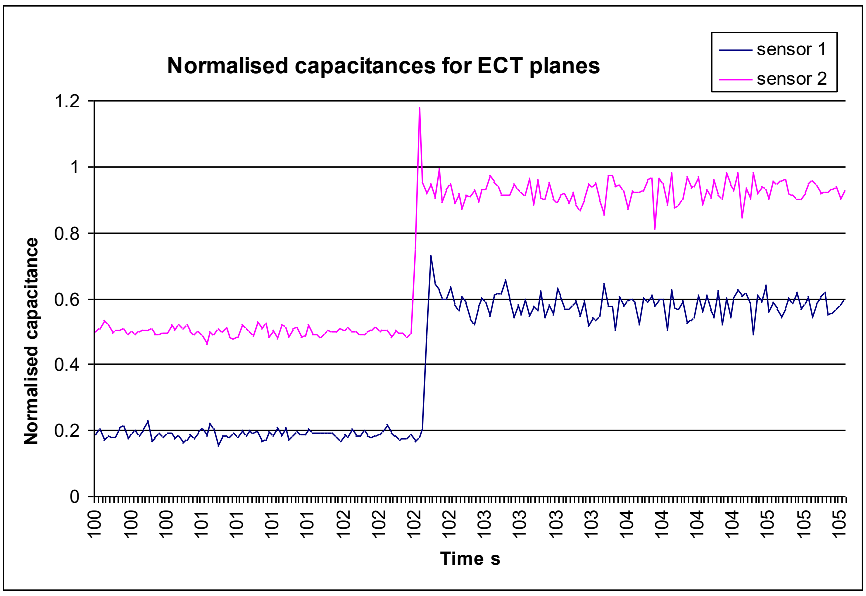

Figure 7 Normalised capacitance against time (s)

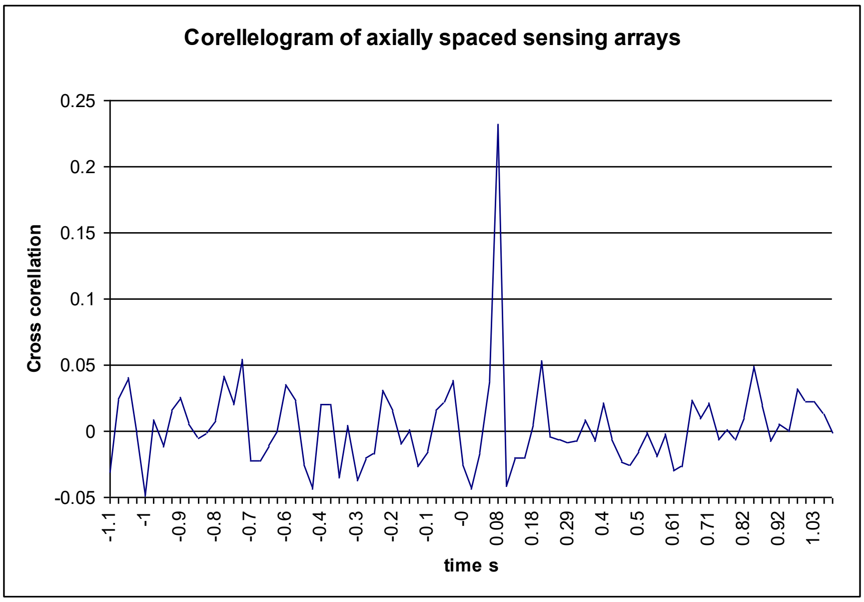

Figure 8 Corellelogram of axially spaced sensing arrays

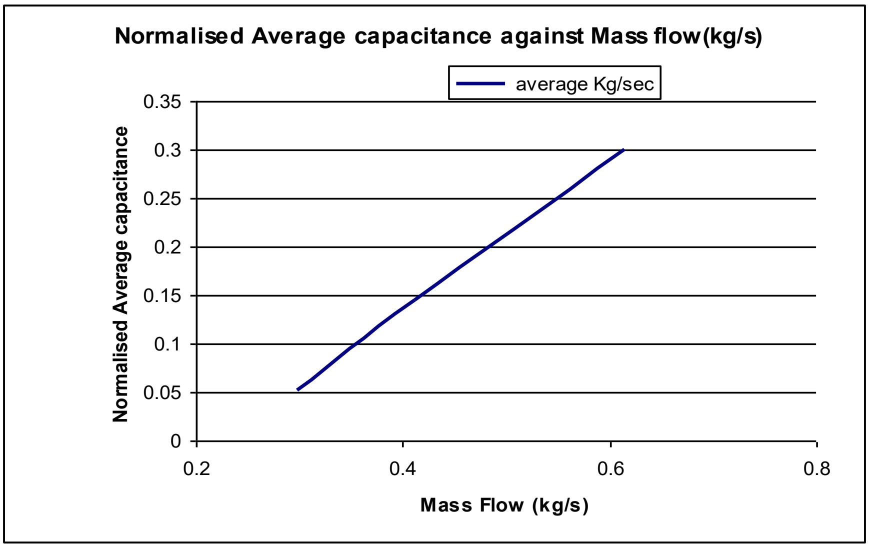

Figure 9. Normalised Average capacitance against Mass flow (kg/s)

6 BENEFITS / LIMITATIONS OF THE VI IMAGING SYSTEM.

The ECT PXI system presents a rugged proprietary instrumentation platform designed for the industrial environment and by minimizing the external application specific hardware a system can be developed which is inherently reliable. The National Instruments LabView based configured Virtual Instrumentation systems offer fast development compared to the design and production times of traditional standalone bench top instruments. The hierarchical and modular nature of LabView enables existing Virtual Instruments to be easily modified or added to, an example of such a case is the use of the VI ECT for flow control using NN or enabling mass flow analysis by cross correlation. The frames rates of the initial serial ECT imaging systems (Ibrahim, 2006) showed a limitation due to the high number software threads the processor has to execute within a

Windows based operating system. These problems have been overcome to some extent with the parallel system which has shown an improved performance than previously developed systems at MMU (Young, 1998). Although the parallel VI ECT system facilitates faster frame rates it is still dominated by the number of operations/threads executed by the embedded processor, any changes in the operating system such as execution of another program results in a reduction of the frame rate. This is a draw back in using Virtual instrumentation over traditional standalone equipment.

7 FUTURE WORK

Initial power usage investigations show that for a fixed mass flow rate of 0.13kgs^{-1} the average power usage of the air blower can be reduced to 30% of its maximum with the use of the NN controller before saltation/dune formation occurs. Further studies for other mass flow rates and NN controller configurations are to be carried out as current results indicate that lower power consumption control before saltation velocities occur could be achieved enabling greater power efficiency. With a dual plane ECT imaging, the VIMS would allow improved accuracy in modelling of the MMU flow rig and pellet behaviour by enabling better prediction of the time-delays involved. On line cross correlation of slug/dune formation using two axially spaced sensing arrays would provide real time mass flow measurements. This could be used for flow control and may provide enhanced dune formation control and enable dilute and dense phase flow to be monitored and controlled. The non deterministic frame rate performances achieved in a Windows environment indicate the need for ECT systems to be developed either as standalone instruments or implemented on a non Windows based real time operating system, such as a National Instruments based RT controller platform. This would not only provide increased deterministic performance but also improve frame rate capability.

8 CONCLUSIONS

A Virtual Instrument, incorporating a Tomographic system capable of imaging pneumatically conveyed pellets in the MMU flow rig, has been designed and built using LabView software running on an embedded Pentium 4 PXI controller. This has resulted in a system which is independent of the standard PC platform and a robust system capable of use in an industrial environment. Advantages of using the PXI system include having an imaging system that uses proprietary interchangeable hardware, and can be easily modified. In addition it lends to a platform that can be used for developing powerful tools using LabView and Matlab. The VIMS system has shown distinct advantages for applications where fast frame rates are not critical but design flexibility and low development costs are required. The VI imaging system was successfully used with an implementation of a Neural Network controller for maintaining a set dune level in a pneumatic flow rig in the presence of disturbances. The mass flow measurements of the pellets using cross correlation has been achieved and show a linear relationship between the mass flow and the normalised average capacitance values.

9 REFERENCES

BUTTERWORTH, G, (1981), Plastics pneumatic conveying and bulk storage, Applied Science Publishers Ltd.

BECK, M.S., PLASKOWSKI, A., (1987), Cross Correlation flowmeters: their design and application, Hilger.

DELOUGHRY, R, PICKUP, E., (2000), Investigation of the closed loop control of a pneumatic conveying system using tomographic imaging, SPIE Vol 4188, 103-113.

DELOUGHRY, R., (2003), Development of a Virtual Instrument System for Industrial Process Tomography, 3rd World Congress on Industrial Process Tomography, 756-760.

DAVENPORT, I., (2004), A Virtual Instrument System for Tomographic Imaging, M.Sc., MMU.

EDGAR, E. (1989), Flow measurement using cross correlation, MMU BEng(Hons) report.

NAIR, C., (2006), Virtual Instrumentation for user-defined measurement, National Instrument Corp (Electronic Engineering Times: Asia).

NATIONAL INSTRUMENTS (2005), NI Developer Zone: Virtual Instrument, National instruments.

SANTORI, M. (1990), An instrument that isn't really, IEEE Spectrum 27(8), 36 -39.

IBRAHIM, I. (2006), Application of an Industrial Embedded Virtual Instrument System to Electrical Capacitance Tomographic Imaging. 4th International Symposium on Process Tomography, Warsaw. Poland, 2006.

YOUNG, M. J. (1998). Tomographic Imaging of Polypropylene nib Granulates for an Industrial Environment. PhD thesis Eng & Tech. Manchester, MMU.

References

1 R. Deloughry, M. Young, E. Pickup, and L. Barratt, "Variable Density Flowmeter for Loading Road Tankers Using Process Tomography", *Process Imaging for Automatic Control*, vol. 4188, pp. 273-283, 2001.

2 T. York, "Status of Electrical Tomography in Industrial Applications", *Journal of Electronic Imaging*, vol. 10, pp. 608-619, 2001.

3 E. Pickup, "Imaging of Pneumatically Conveyed Polyethylene Particles", PhD Thesis, Manchester Metropolitan University, Manchester, 1997.

4 M. Young, "Tomographic Imaging of Polypropylene Nib Granulates for an Industrial Application", PhD Thesis, Manchester Metropolitan University, Manchester, 1999.

5 S. M. Huang, "Capacitance Transducers for Concentration Measurements", PhD Thesis, UMIST, Manchester, 1986.

6 P. W. R. Southern, "A Multi-Component Fluid Capacitance Measurement System", M Phil Thesis, Manchester Metropolitan University, Manchester, 1995.

7 National Instruments Corporation, "About Virtual Instrumentation", [Online], Available from: http://zone.ni.com/devzone/cda/tut/p/id/2964, 2005.

8 I. Davenport, "A Virtual Instrument System for Tomographic Imaging", MSc Thesis, Manchester Metropolitan University, Manchester, 2004.

9 I. Ibrahim, "A Virtual Instrument Tomographic Measurement System", PhD Thesis, Manchester Metropolitan University, Manchester, 2007.

10 D. Romanchik, "Choose the Right Bus for Electronic Test Systems ", [Online], Available from: http://www.hit.bme.hu/~papay/edu/GPIB/bus.htm, 1997.

11 National Instruments Corporation, "Hardware's Role in Virtual Instrumentation", [Online], Available from: http://zone.ni.com/devzone/cda/tut/p/id/3397, 2007.

12 National Instruments Corporation, "Virtual Instrumentation and Traditional Instruments", [Online], Available from: http://zone.ni.com/devzone/cda/tut/p/id/4757, 2007.

13 T. Jeffrey and K. Jim, "LabVIEW for Everyone: Graphical Programming Made Easy and Fun (3rd Edition) (National Instruments Virtual Instrumentation Series)": Prentice Hall PTR, 2006.

14 National Instruments Corporation, "Achieving Productivity Gains with National Instruments LabVIEW", [Online], Available from: ftp://ftp.ni.com/evaluation/labview/ekit/productivity_ekit.pdf, 2007.

15 National Instruments Corporation, "NI PXI-1042 Series User Manual and Specifications", [Online], Available from: http://www.ni.com/pdf/manuals/371088a.pdf, 2007.

16 National Instruments Corporation, "NI PXI-8186/8187 User Manual and Specifications", [Online], Available from: http://www.ni.com/pdf/manuals/370747c.pdf, 2005.

17 National Instruments Corporation, "Analog Output Series User Manual", [Online], Available from: http://www.ni.com/pdf/manuals/370735e.pdf, 2007.

18 National Instruments Corporation, "S Series User Manual", [Online], Available from: http://www.ni.com/pdf/manuals/370781h.pdf, 2007.

19 National Instruments Corporation, "NI PXI-6534 Series Data Sheet", [Online], Available from: http://www.ni.com/pdf/products/us/4mi432-434.pdf, 2007.

20 Y. Yan, "Mass Flow Measurement of Bulk Solids in Pneumatic Pipelines", *Measurement Science and Technology*, vol. 7, pp. 1687-1706, 1996.

21 F. Shao, Z. Lu, E. Wu, and S. Wang, "Study and Industrial Evaluation of mass Flow Measurement of Pulverized Coal for Iron-Making Production", *Flow Measurement and Instrumentation*, vol. 11, pp. 159-163, 2000.

22 E. A. Hammer and R. G. Green, "The Spatial Filtering Effect of Capacitance Transducer Electrodes", *Journal of Physics E: Scientific Instruments*, vol. 16, pp. 438-443, 1983.

23 E. S. Edgar, "Flow Measurement Using Cross Correlation", B(Eng) Project Report, Manchester Polytechnic, Manchester, 1989.

24 M. S. Beck and A. Plaskowski, "Cross Correlation Flowmeters: Their Design and Application": Hilger, 1987.

25 M. S. Beck, R. G. Green, and R. Thorn, "Non-intrusive Measurement of Solids Mass Flow in Pneumatic Conveying", *Journal of Physics E: Scientific Instruments*, vol. 20, pp. 835-840, 1987.

26 R. G. Green, H. K. Kwan, R. John, and M. S. Beck, "A Low Cost Solids Flowmeter for Industrial Use", *Journal of Physics E: Scientific Instruments*, vol. 11, pp. 1005-1010, 1978.

27 C. G. Xie, A. L. Stott, S. M. Huang, A. Plaskowski, and M. S. Beck, "Mass-Flow Measurement of Solids Using Electrodynamic and Capacitance Transducers", *Journal of Physics E: Scientific Instruments*, vol. 22, pp. 712-719, 1989.

28 Thermo Electron Corporation, "Ramsey Granucor Solids Flow Measurement System", [User Manual], 2007.

29 Y. Yan and A. R. Reed, "Experimental Evaluation of Capacitance Transducers for Volumetric Concentration Measurement of Particulate Solids", *Flow Measurement and Instrumentation*, vol. 10, pp. 45-49, 1999.

30 M. Byars, "Developments in Electrical Capacitance Tomography", 2nd World Congress on Industrial Process Tomography, Hannover, Germany, 2001.

31 Process Tomography Limited, "Engineering Design Rules for ECT Sensors", PTL: Application Note: AN3, 2001.

32 C. G. Xie, A. L. Stott, A. Plaskowski, and M. S. Beck, "Design of Capacitance Electrodes for Concentration Measurement of Two-Phase Flow", *Measurement Science and Technology*, vol. 1, pp. 65-78, 1990.

33 N. Reinecke and D. Mewes, "Recent Developments and Industrial/Research Applications of Capacitance Tomography", *Measurement Science and Technology*, vol. 7, pp. 233-246, 1996.

34 K. Zhu, S. Madhusudana Rao, C. Wang, and S. Sundaresan, "Electrical Capacitance Tomography Measurements on Vertical and Inclined Pneumatic Conveying of Granular Solids", *Chemical Engineering Science*, vol. 58, pp. 4225-4245, 2003.

35 Process Tomography Limited, "Calculation of Volume Ratio for ECT Sensors", PTL: Application Note: AN2, 1999.

36 S. S. Donthi, "Capacitance based tomography for industrial applications. " M.Tech. Report, Indian Institute of Technology, Bombay, 2004.

37 Process Tomography Limited, "Generation of ECT images from Capacitance Measurements", PTL: Application Note: AN1, 2001.

38 Y. Li and W. Q. Yang, "Virtual Electrical Capacitance Tomography Sensor", *Journal of Physics: Conference Series*, vol. 15, pp. 183–188, 2005.

39 W. Q. Yang, D. M. Spink, J. C. Gamio, and M. S. Beck, "Sensitivity Distributions of Capacitance Tomography Sensors with Parallel Field Excitation", *Measurement Science and Technology*, vol. 8, pp. 562-569, 1997.

40 Process Tomography Limited, "An Iterative Method for Improving ECT images", PTL: Application Note: AN4, 1999.

41 S. Liu, L. Fu, and W. Q. Yang, "Comparison of Three Image Reconstruction Algorithms for Electrical Capacitance Tomography", 2nd World Congress on Industrial Process Tomography, Hannover Germany, 2001.

42 S. M. Huang, A. L. Stott, R. G. Green, and M. S. Beck, "Electronic Transducers for Industrial Measurement of Low Value Capacitances", *Journal of Physics E: Scientific Instruments*, vol. 21, pp. 242-250, 1988.

43 W. Q. Yang, "Hardware Design of Electrical Capacitance Tomography Systems", *Measurement Science and Technology*, vol. 7, pp. 225-232, 1996.

44 M. K. Xiaohui Hu, Wuqiang Yang, Songming Huang, "Further Analysis of Charge/Discharge Capacitance Measuring Circuit Used with Tomography Sensors", *Sensors & Tranducers*, vol. 80, pp. 1246-1256, 2007.

45 D. Georgakopoulos and W. Q. Yang, "Key Issues in the Design of a Capacitance Transducer for Tomography", 2nd World Congress on Industrial Process Tomography, Hannover, Germany, 2001.

46 D. P. Blair and P. H. Sydenham, "Phase Sensitive Detection as a Means to Recover Signals Buried in Noise", *Journal of Physics E: Scientific Instruments*, vol. 8, pp. 621-627, 1975.

47 R. W. M. Smith, I. L. Freeston, B. H. Brown, and A. M. Sinton, "Design of a Phase-Sensitive Detector to Maximize Signal-to-Noise Ratio in the Presence of Gaussian Wideband Noise", *Measurement Science and Technology*, vol. 3, pp. 1054-1062, 1992.

48 W. Q. Yang and T. A. York, "New AC-Based Capacitance Tomography System", *IEE Proceedings - Science, Measurement and Technology*, vol. 146, pp. 47-53, 1999.

49 R. Deloughry, I. Davenport, X. Ma, and P. V. S. Ponnapalli, "Development of a Virtual Instrument System for Industrial Process Tomography", 3rd World Congress on Industrial Process Tomography, Banff, Canada, 2003.

50 R. Deloughry, M. Young, E. Pickup, and L. Barratt, "Development of a Variable Density Flowmeter for an Industrial Application", 1st World Congress on Industrial Process Tomography, Buxton, Greater Manchester, UK, 1999.

51 S. Natarajan, "Theory and Design of Linear Active Networks": Collier MacMillan, 1987.

52 A. Gonzalez-Nakazawa, J. C. Gamio, and W. Q. Yang, "Transient Analysis of the AC based Capacitance Measuring Circuit for Tomography", 3rd World Congress on Industrial Process Tomography, Banff Canada, 2003.

53 E. C. Ifeachor and B. W. Jervis, "Digital Signal Processing:A Practical Approach 2nd Edition": Prentice Hall, 2001.

54 M. S. Beck, "Correlation in instruments: Cross Correlation Flowmeters", *Journal of Physics E: Scientific Instruments*, vol. 14, pp. 7-19, 1981.

55 R. Deloughry, "Electronic Instrumentation", Undergraduate Course Material, Manchester Metropolitan University, 2006.

56 National Instruments Corporation, "Function and VI Reference Manual", [User Manual], 1998.

57 W. Q. Yang and S. Liu, "Role of Tomography in Gas/Solids Flow Measurement", *Flow Measurement and Instrumentation*, vol. 11, pp. 237–244, 2000.

58 W. Q. Yang and M. S. Beck, "An Intelligent Cross Correlator for Pipeline Flow Velocity Measurement", *Flow Measurement and Instrumentation*, vol. 8, pp. 77-84, 1998.

59 N. Reinecke and D. Mewes, "Investigation of the Two-Phase Flow in Trickle-Bed Reactors Using Capacitance Tomography", *Chemical Engineering Science*, vol. 52, pp. 2111-2127, 1997.